UNIVERSITY OF CALIFORNIA
RIVERSIDE

Electrical and Mechanical Properties of Graphene

A Dissertation submitted in partial satisfaction
of the requirements for the degree of

Doctor of Philosophy

in

Physics

by

Wenzhong Bao

March 2012

Dissertation Committee:

Dr. Chun Ning (Jeanie) Lau, Chairperson
Dr. Jing Shi
Dr. Roland Kawakami

The Dissertation of Wenzhong Bao is approved by:

_____

_____

_____

Committee Chairperson

University of California, Riverside

Acknowledgements

First and foremost I would like to thank Professor Chun Ning (Jeanie) Lau for being a prime example of good advisor and scientist. She has been always supportive, attentive, kind, and patient to me and I am greatly indebted to her for giving me the opportunity to work with her and her lab. After graduation she will remain a role model for me during my lifetime. Here I would also thank the members of my defense and candidacy exam committees for their interest and precious time.

Dr. Lau has had great professional infuence on my development as a scientist. One of the many remarkable powers within Jeanie is that she always has a great number of genius ideas that soon turn out to work – unfortunately most of them materialize as Science or Nature papers published by other groups. She also effectively motivates and encourages us when we encounter difficulties or failures – as we all know, nanofabrication can be really frustrating. Another important thing she taught me is how to deal with people in academia; I believe not every advisor shares this with his or her students. Even more supportive she once helped me deal with a car accident that first happened in my life, that is why sometimes Jeanie told us she is busier than our babysitter and I couldn't disagree. Another annoying ability Jeanie possesses is that her intuitive insights often turns out to be correct after I displayed endless efforts to contradict. Anyway, thanks for teaching me, listening to me and letting me argure with you. I couldn't ask for better guidance.

During these five years one of the greatest things happened in my life was the marriage to my wife Honghui Cheng, a girl I met as early as in the summer of 2005. Between Paris and Riverside, we kept in long distance contact via phone and internet, at last we got together under Eiffel tower in 2009's Christmas. I thank her for her full support, encouragement and her love. I love her deeply and will always be a good husband.

When I first arrived at UCR and joined Jeanie's lab, graphene was only fabricated by a few groups. I sat in the basement of Pierce Hall, spent hours rubbing a piece of microns long graphene sheet, and really doubted what Feng Miao, who is Jeanie's first student, had told me every week: "One day our group's name will become famous in graphene reserach." Five yeasr later, we can say that we survive the fierce competition, especially thanks to the original batch of the group memebers includes Feng Miao, Gang Liu and former postdocs Yong Zhang and Ulas Coskun for building this lab together with Jeanie. The lab couldn't work so smoothly without their original work on graphene and carbon nanotube. I would also like to thanks all current group memebers: Jairo Velasco, Hang Zhang, Lei Jing, Yongjin Lee, Kevin Myhro, Fenglin Wang, Jhao-Wun Huang, Zeng Zhao and David Tran. Your passion and creativity will make this group stronger and one of the leading groups in the future graphene research.

I was very fortunate to get help which was more than I ever hoped for from my labmates and close friends Gang Liu and Feng Miao. Gang Liu helped me a lot when

I first came to southern California; I still remember that he reserved an apartment for me when I was still in China, drove me to supermarket before I bought my first car, and patiently taught me driving. He is also smart and diligent, e.g. all the works on "suspended top gate" in our lab are based on his genius invention of suspended structure. Feng Miao, who led the first graphene project and published the first big paper in our group, also helped me a lot at UCR, he trained me everything from fabrication to measurement and never complained repeating so many times to me. And every discussion I had with him contributed to my understanding of research and life. I will cherish a lifetime the friendships I made with them in Lau's group.

Jairo Velasco and I joined Lau's group in the same year, then we became very good friends. We have resemblance in physical shape, clothing, taste of japanese animes, and even daily schedule (before I got married). We both like Physics and strive together towards our goal of becoming faculty members. I will alwasy cherish the time we spent together fabricating devices and analyzing data.

I also have many collaborators who deserve acknowledgement: Prof. Dmitry Smirnov helped us operate high field magnet at NHMFL in Tallahassee, Brian Standley from Prof. Marc Bockrath's group taught us graphene switching technique and helped me with the low temperature measurement in his group, Prof. Hsin-Ying Chiu who also graduated from Prof. Marc Bockrath's group helped us on BOE etching of suspended graphene, Peng Wei from Prof. Jing Shi' group helped us setup electric measurement and programming. Zhen Chen and Wanyoung Jang from Prof.

Chris Dames' group helped me build the hot stage for *in-situ* SEM imaging. I also need to acknowledge help and advice from: Wei Han (also my roommate for three years), Wei-Hua Wang and Kathleen McCreary from Prof. Roland Kawakami's group, Guanxiong Liu, Irene Calizo and Suchi Ghosh from Prof. Alexander Balandin' group. Two technicians in our cleanroom: Dong Yan and Dexter Humphrey also helped me a lot to develop my fabrication recipes.

I especially thank my close friends, Peng Wei and Hsiang-Ku Lin, Yang Meng, Hsin-Ying Chiu, Deqi Wang, Wei Han, Tao Lin and Vivian Ouyang, Yachong Wang, Dezheng Sun, Ling Yang, Xinfei Liu, Xin He, Zhiyong Wang, Peng Wang, Tengfei Miao, Prof. Zuhong Xiong, Keyu Pi, Yan Li, Yong Pu, Wanyoung Jiang, Zhen Chen. Together we shared a lot wonderful memories and our friendship will be cherished a lifetime.

Throughout my five years at UCR, playing table tennis has become an important part of my life. Thanks to Qiguo Jing, Gang Liu (so many boys named "Gang Liu" in China….) and Gang Xia, I recoganize all memories we enjoyed TT ball and all tournaments in which we played together.

Lastly and most importantly, I am grateful to all my family members for their constant support and love through my entire life. Though I did not spend much time with you within the last five years, I have dreamed you so much, I love you all.

ABSTRACT OF THE DISSERTATION

Electrical and Mechanical Properties of Graphene

by

Wenzhong Bao

Doctor of Philosophy, Graduate Program in Physics
University of California, Riverside, March 2012
Dr. Chun Ning Lau, Chairperson

Graphene is an exciting new atomically-thin two-dimensional (2D) system of carbon atoms organized in a hexagonal lattice structure. This “wonder material” has been extensively studied in the last few years since it’s first isolation in 2004. Its rapid rise to popularity in scientific and technological communities can be attributed to a number of its exceptional propertiess. In this thesis I will present several topics including fabrication of graphene devices, electrical and mechanical properties of graphene.

I will start with a brief introduction of electronic transport in nanosclae system including quantum Hall effect, followed by a discussion of fundamental electrical and mechanical properties of graphene. Next I will describe how graphene devices are produced: from the famous “mechnical exfoliation” to our innovative “scratching exfoliation” method, together with the traditional lithography fabrication for graphene devices. We also developed a lithography-free technique for making electrical contacts to suspended graphene devices. Most of the suspended devices

presented in this thesis are fabricated by this technique.

Graphene has remarkable electrical properties thanks to its crystal and band structures. In Chapter 3, I will first focus on proximity-induced superconductivity in graphene Josephson transistors. In this section we investigate electronic transport in single layer graphene coupled to superconducting electrodes. We observe significant suppression in the critical current I_c and large variation in the product I_cR_n in comparison to theoretic prediction; both phenomena can be satisfactorily accounted for by premature switching in underdamped Josephson junctions.

Another focus of our studies is quantum Hall effect and many body physics in graphene in suspended bilayer and trilayer graphene. We demenstrate that symmetry breaking of the first 3 Landau levels and fractional quantum Hall states are observed in both bilayer and trilayer suspended graphene devices. A surprising finding in these systems is the observation of insulating states in both suspended bilayer and trilayer graphene devices, which arises from electronic interactions. In bilayer graphene, we observe a phase transition between the single-particle metallic state and the interaction-induced insulating state in ultra-clean BLG, which can be tuned by temperature, disorder, charge density n and perpendicular electric field $E_\perp$. In trilayer graphene we demonstrate dramatically different transport properties arising from the different stacking orders, and an unexpected spontaneous gap opening in charge neutral ABC-stacked trilayer graphene.

One of graphene's unique properties is that it is nature's thinnest elastic

membrane with exceptional mechanical properties. In chapter 7 I will describe the first direct observation and controlled creation of one- and two-dimensional periodic ripples in suspended graphene sheets, using both spontaneously and thermally generated strains. We are able to control ripple orientation, wavelength and amplitude by controlling boundary conditions and exploiting graphene's negative thermal expansion coefficient, which we measure to be much larger than that of graphite. In addition, we also study the morphological change of suspended graphene sheets by apply gate voltages, which is a simple and direct method to strain and buckle graphene.

Our experimental results contribute to the fundamental understanding of electrical and mechanical properties of graphene, and may have important implications for future graphene based applications.

Table of Contents

List of Figures

List of Tables

Chapter 1. Introduction

For the past few years, when people ask “what you do in the lab”, I replied two words: *nano science*, which is at both self-explanatory and cool-sounding– just imagine iPod-Nano®.

Fig. 1-1 A boy and an iPod Nano

More specifically, I use another word *graphene* [1, 2] starting from 2010, thanks to the Physics Nobel Prize awarded Geim and Novoselov, who have started the field and made “graphene” into a household term.

The thesis is structured as follows. Chapter 1 contains a brief introduction of transport in nanosclae system and fundamental electronic properties of graphene. In Chapter 2 I will describe standard and new methods of isolating graphene and device fabrication, with particular emphasis on ultrclean suspended graphene devices.

The rest of my thesis could be naturally divided into two parts: electrical and mechanical properties, which correspond to chapter 3-6 and chapter 7-8, respectively.

In Chapter 3, I will first focus on proximity induced superconductivity in graphene Josephson transistors, which is also my first Ph.D. project. Next in chapter 4 I will discuss quantum Hall effect in graphene and focus on our experimental works of suspended bilayer and trilayer graphene. Moreover in chapter 5 and 6 I will also discuss an electronic-interaction driven effect -- insulating state in both suspended bilayer and trilayer graphene devices, while the latter has a stacking order dependence.

In Chapter 7, we will investigate mechanical properties of suspended graphene. We will characterize suspended graphene ripples and exploit the effective control of this ripple texturing, and discuss the gating-induced morphological change of suspended graphene sheets in chapter 8.

Chapter 9 concludes the thesis with a brief discussion of future outlook.

1.1 Two Dimensional Electron Systems

If the thickness of a conductor is smaller than the size of the electron wavelength, the conductor forms a two-dimensional electron system (2DES). When Coulomb interactions are ignored, the electrons can be approximated as a "gas" of free particles, which roam freely in the 2D plane and their motion in the third dimension could be ignored. Interesting quantum effects could arise in this system. Typically, 2DES could be realized in 1) MOSFETs (metal–oxide–semiconductor field-effect transistor), as shown in Fig. 1.2(a); 2) HEMTs (high-electron-mobility transistors), as shown in Fig. 1.2(b); and 3) the surface of a material such as free electrons floated on the surface of liquid helium [3], or graphene sheets [4, 5], using the field effect.

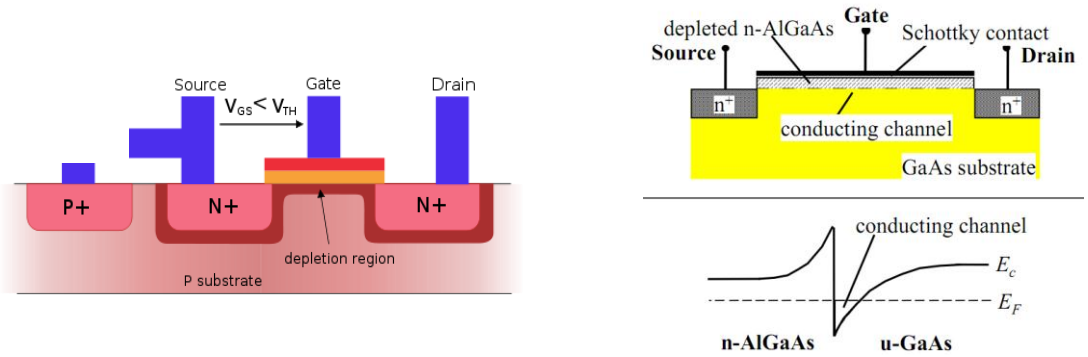

Fig. 1-2 (a) A cross section of MOSFET device. (http://en.wikipedia.org/wiki/File: MOSFET _functioning_body.svg) (b) A schematic and cross section band structure of a GaAs/AlGaAs HEMT device (http://www.ecse.rpi.edu/shur/sdm2/Notes/Notes pdf /18HFET.pdf)

1.2 One Dimensional Quantum Wire Systems

Now we consider a one-dimensional (1D) wire, which is long in the longitudinal direction but short in the transverse directions so that its width and thickness are comparable to the Fermi wavelength of the electrons. Because of quantum confinement of conduction electrons in the transverse directions, their transverse energy is quantized into a series of discrete values. In the transverse direction, in the absence of impurities, electrons propagate and we can view the wire as a waveguide for transmission of electron quantum waves between two reservoirs.

One consequence of 1D propagation of electron wavefunctions is that the Ohm's Law, in which the electrical resistivity of a wire $R=\rho l/A$, is no longer valid. Here ρ is the resistivity, l is the length, and A is the cross-sectional area of the wire. Instead, in such a system conductance is quantized, which can be easily derived. In 1-D the current I is equal to the current density, which is given by:

$$j = I = -ev(\mu_1 - \mu_2)\frac{dn}{dE},$$

where v is the group velocity of an electron at the Fermi energy E_F in one channel, $(\mu_1 - \mu_2)$ is the difference in electrochemical potential between the two reservoirs shown in Fig. 1.3, and $\frac{dn}{dE}$ is the density of energy states (per unit length) at E_F, then we can write it as:

$$\frac{dn}{dE} = \left(\frac{dn}{dk}\right)\left(\frac{dk}{dE}\right).$$

Since $\frac{dn}{dk} = 1/2\pi$, $\frac{dE}{dk} = \frac{\hbar^2 k}{m} = v\hbar$ and $(\mu_1 - \mu_2) = -e\Delta V$,

$$I = -ev(\mu_1 - \mu_2)\frac{dn}{dE} = -\frac{e(\mu_1 - \mu_2)}{2\pi\hbar} = \frac{e^2\Delta V}{h}.$$

Thus

$$G = \frac{I}{V} = \frac{e^2}{h}.$$

If the there are N waveguide channels are populated, the total conductance is then

$$G = N\frac{2e^2}{h}.$$

Here the factor 2 is included owing to the spin degeneracy.

Fig. 1-3 One dimensional wire connecting two reservoirs with different chemical potentials.

Carbon nanotube (Fig. 1.4(a)) could be an ideal quantum wire system [6], together with other one-dimensional chemically grown nanowires (Fig. 1.4(b)). Both types of systems have been extensively studied [7-11].

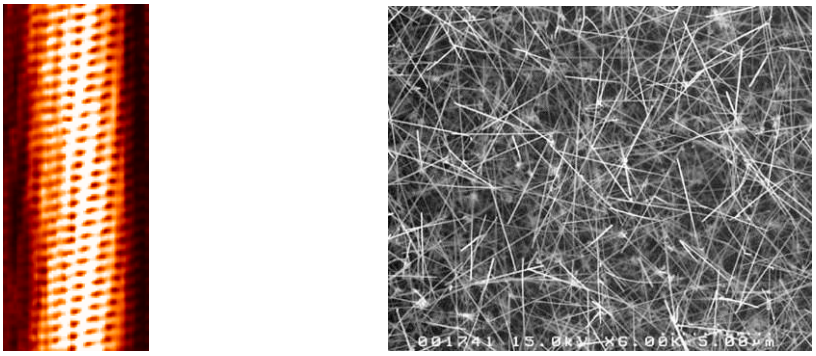

Fig. 1-4 (a) An atomically resolved STM image of chiral carbon natube. (http:// www.ncnr.nist.gov/staff/taner/nanotube/types.html) (b) An SEM image of silicon nanowire grown in CVD http://www.firstnano.com /applications/sinanowire/1/)

1.3 Zero Dimensional Quantum Dots

A quantum dot (QD) is a conductor that is confined in all three spatial dimensions [12-17]. Typically, QDs are conducting island connected to reservoirs of electrons by tunnel barriers (Fig. 1.5). The number of electrons in the island can be changed by a nearby electrostatic gate.

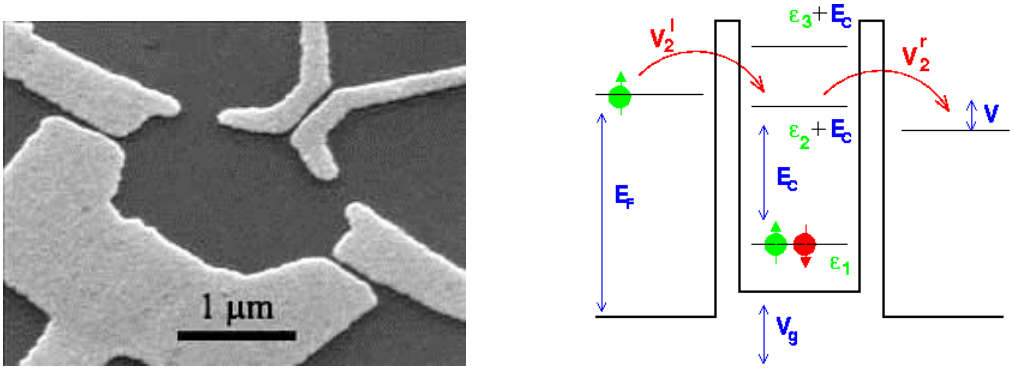

Fig. 1-5 (a) A quantum dot defined by 5 metallic gates fabricated on the surface of a GaAs based heterostructure, in which a two-dimensional electron gas recides (http://pages.unibas.ch/ phys-meso/Pictures/pictures. html). (b) A theoretical sketch of a QD (http://www.fkf.mpg.de/ metzner/research/qdot/qdot.html).

The Coulomb interaction among electrons in the QD creates an energy barrier so that exactly an integer number of electrons N is localized within the dot. When an electron tunnerls onto the dot, the total energy of the dot increases by $e^2/2C$, the charging energy (C is the total capacitance of the QD). Therefore in the zero-bias limit, it is impossible to add or remove electrons if added engergy is smaller than $e^2/2C$, resulting in zero or very low conductance. This phenomemon is known as Coulomb blockade.

To properly localize a discrete number of electrons on the dot, the charge energy $e^2/2C$ needs to exceed the quantum energy uncertainty $\Delta E \approx \frac{\hbar}{\Delta t} \approx \frac{\hbar}{RC}$ associated with the RC time constant, which is also the lifetime of charges on the island. Thus we obtain:

$$R \geq \frac{2\hbar}{e^2} = \frac{2}{\pi}\left(\frac{2\pi\hbar}{2e^2}\right) = \frac{2}{\pi}\left(\frac{h}{2e^2}\right) \approx \frac{h}{2e^2} \sim 12.9\ \text{k}\Omega,$$

which is also the quantum resistance we derived in the previous section. Secondly, the thermal fluctuation energy $kT < e^2/2C$ is also required to avoid thermal fluctuations washing out the features, which requires that the capacitance of QD (and hence QD itself) should be rather small.

When we increase the gate voltage V_g, more electrons can be added. Adding each electron onto QD will result in

$$\Delta V_g = e/C_g,$$

where C_g is the gate-QD capacitance. Actually applying source-drain voltage V_{sd} has a similar effect if

$$\Delta V_{sd} = e/C_{total},$$

where

$$C_{total} = C_g + C_{source} + C_{drain},$$

and C_{source} and C_{drain} are contacts-QD capacitance, Therefore by fixing the V_{sd} and changing V_g, a series of spikes of measured current I_{QD} could be observed and the spacing is ΔV_g.

1.4 Density of states of 2D, 1D and 0D

The density of states (DOS) of an *n*-dimentional system describes the number of states per interval of energy at each engergy level. If the dispersion relation of a system is

$$E = E_0 + c_k k^p .$$

Therefore

$$k = (\frac{E - E_0}{c_k})^{1/p} .$$

We also define $\Omega_n(k) = c_n k^n$ as the volume in *n*-dimentions *k* space containing wave vectors smaller than *k* (here $c_1 = 2$, $c_2 = \pi$, $c_3 = 4\pi/3$), then the substitution of dispersion relation gives the volume of occupied states

$$\Omega_n(E) = \frac{c_n}{c_k^{n/p}} (E - E_0)^{n/p} .$$

Differentiating this volume with respect to the energy gives the DOS of such a dispersion relation:

$$DOS_n(E) = \frac{d\Omega_n(E)}{dE} = \frac{nc_n}{pc_k^{\,n/p}}(E - E_0)^{n/p-1}.$$

Assuming a parabolic dispersion relation $E = \frac{\hbar^2}{2m^*}k^2$, the DOS for *n*-dimentional system is shown in Fig. 1.6. In chapter 1.6.2 we can also use this to calculate 2D DOS of graphene using derived dispersion relation in graphene.

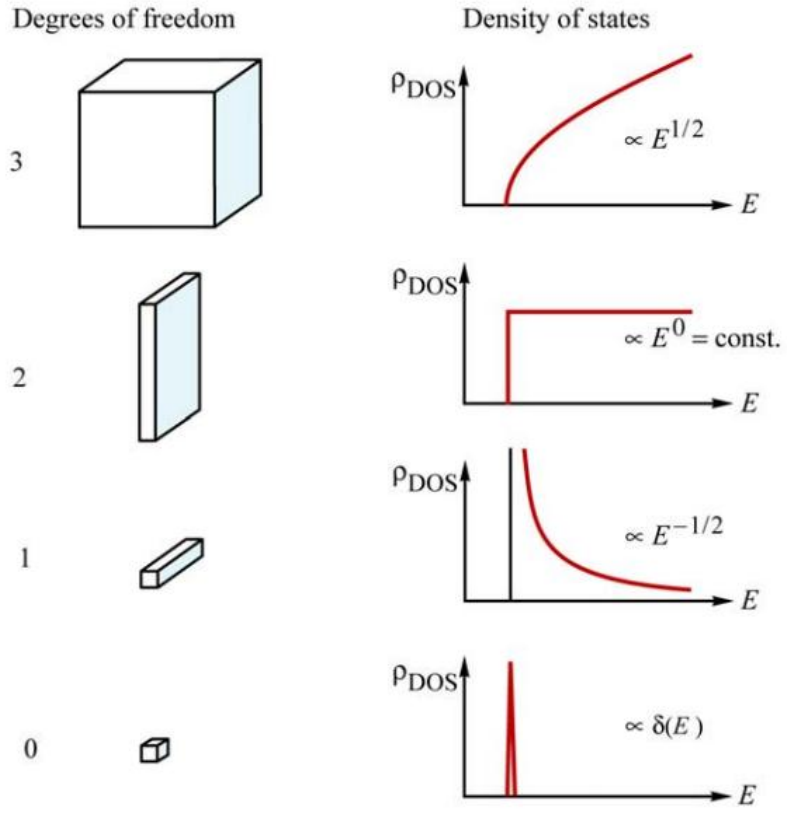

Fig. 1-6 DOS of 3,2,1 and 0 dimentional systems.
(http://www.ecse.rpi.edu/~schubert/)

1.5 Quantum Hall effect

The classical Hall effect is observed when a current flows in a conductor placed in a magnetic field. As shown in Fig. 1.7, a uniform current flow I along the x-direction results in a longitudinal voltage drop V_{xx}=(V1-V2), and transverse (or Hall) voltage drop V_{xy}=(V2-V3). Therefore we can define Hall and longitudinal resistivities:

$$\rho_{xx} = \frac{V_{xx}}{I}\frac{W}{L} \quad \text{(Longitudinal) and} \quad \rho_{xy} = \frac{V_{xy}}{I} \text{ (Hall),}$$

and the corresponding Hall and longitudinal conductivities are

$$\sigma_{xy} = \frac{\rho_{xy}}{\rho_{xx}^{\,2} + \rho_{xy}^{\,2}} \quad \text{and} \quad \sigma_{xx} = \frac{\rho_{xx}}{\rho_{xx}^{\,2} + \rho_{xy}^{\,2}}\,.$$

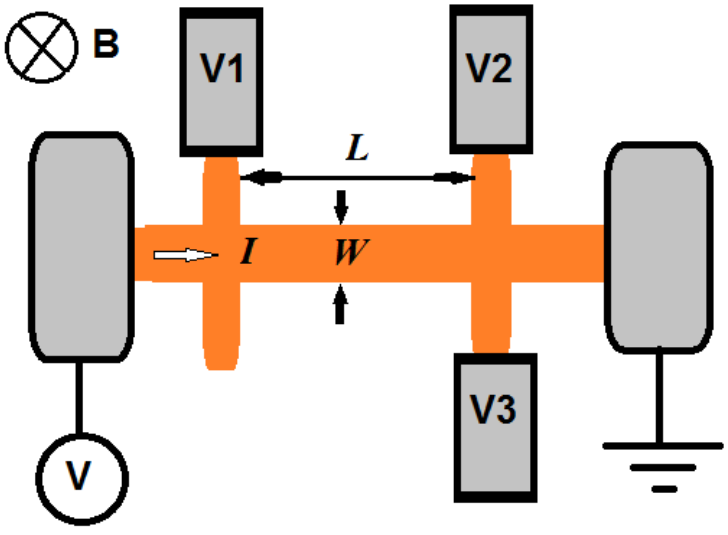

Fig. 1-7 Two dimensional electronic device with Hall bar geomety.

German physicist Klaus von Klitzing first studied the Hall (ρ_{xy}) and

longitudinal (ρ_{xx}) resistivity of 2-D Si MOSFET samples in 1980 [18]. In strong magnetic field and at low temperature, he found that at low density Hall resistivity exhibits quantized plateaus at values of

$$\rho_{xy} = \frac{h}{ne^2}.$$

This quantization is referred to as the quantum Hall effect (QHE) [19, 20]. The longitudinal resistivity ρ_{xx} vanishes at the plateaus, as shown as in Fig. 1.8, implying that the transport is non-dissipative.

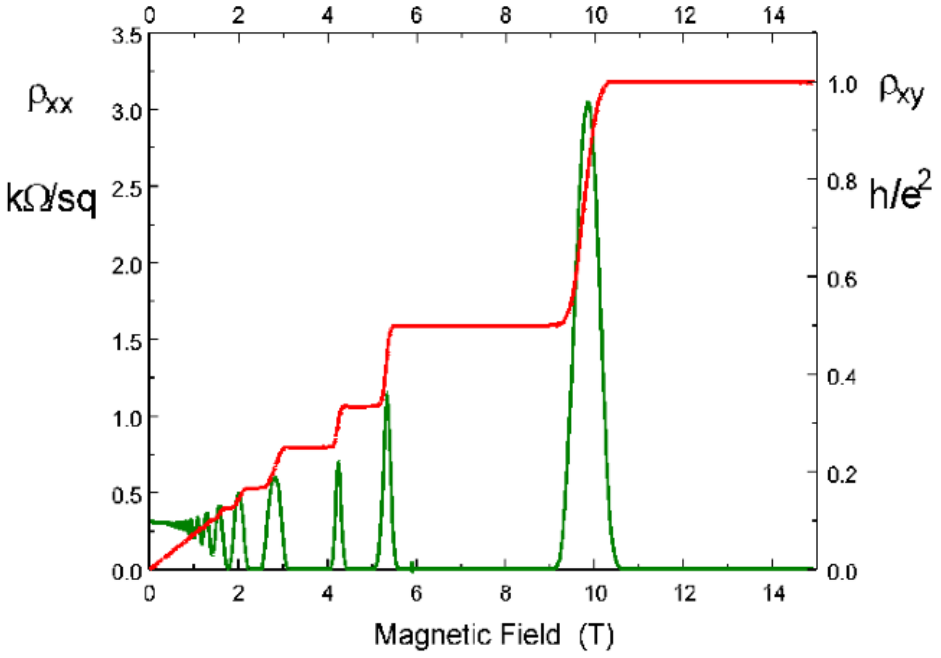

Fig. 1-8 Typical measurement of the integer quantum Hall effect in a GaAs-GaAlAs heterojunction (Image created by D.R. Leadley, Warwick University).

The vanishing of ρ_{xx} therefore also results in the quantization of Hall conductivity:

$$\sigma_{xy} = \frac{\rho_{xy}}{\rho_{xx}^{\ 2} + \rho_{xy}^{\ 2}} = n\frac{e^2}{h}.$$

The oscillations in ρ_{xx} at small B are called as Shubnikov-deHaas (SdH) oscillations, arising from that the DOS of 2-DEG breaks up into a sequence of δ-function Landau levels (LL, see definition below) spaced by $\hbar\omega_c$ at high magnetic fields:

$$DOS(E,B) \approx \frac{2eB}{h}\sum_{n=0}^{\infty}\delta\left[E-(n+\frac{1}{2})\hbar\omega_c\right],$$

where n is integer numbers, B is magnetic field and $\omega_c = eB/m$ is the cyclotron frequency. Therefore at a fixed charge density n_s, filled LLs also changes with B. ρ_{xx} then goes through a maximum every time this number is half-integer, when Fermi energy lies at the center of a LL. If B_1 and B_2 correspond to two successive maximums, they must be related by:

$$\frac{n_s}{2eB_1/h} - \frac{n_s}{2eB_2/h} = 1,$$

thus

$$n_s = \frac{2e}{h\left(\frac{1}{B_1}-\frac{1}{B_2}\right)}.$$

In this equation we also notice that the period $\Delta\left(\frac{1}{B}\right)$ in SdH oscillation is constant and we can use this to determine charge density.

To understand plateau features of Hall conductivity in QHE, we derive the electronic spectrum by solving the Schrödinger equation in a rectangular conductor:

$$E_n = (n+\frac{1}{2})\hbar\omega_c + U(y).$$

Actually each set of wave functions with the same value of *n* is called a *Landau level*. This is illustrated in Fig 1.9 and here $U(y)$ is a confining potential resulted from boundary condition. The dispersion of the LLs readily implies the existence of the conducting 1-D channels propagating along the edge. These edge states are distributed on opposite sides of the 2-DEG system; they are well separated and travel in opposite directions, therefore it completely diminishes backscattering and makes system dissipationless. At filling factor υ, there are υ (due to diminishing of at the same edge) conducting edge channels, which give rise to quantized Hall conductivity of $\upsilon\frac{e^2}{h}$. More discussion about the QHE could be found in [21].

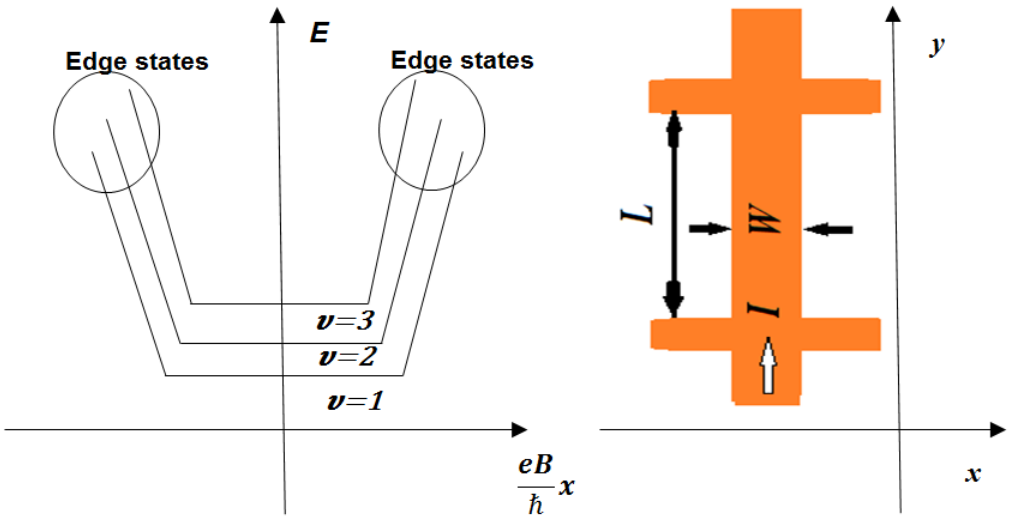

Fig. 1-9 Edge states topologically separated by the magnetic field. In the absence of scattering the quantum of conductance e^2/h carried by each channel contributes into the quantization of the Hall conductivity σ_{xy}.

1.6 Introduction to Graphene

As conventional electronics already pushes Moore's law to extremely high densities, the traditional Si-CMOS technology faces several critical challenges such as self-heating due to increased dissipated power density, mobility degradation, and leakage currents due to charge tunneling. Thus researchers have been seeking for alternative electronic materials to supplement or replace Si-CMOS technology.

Graphene has been proposed to be a very important candidate for future generation nanoelectronics. As the thinnest isolated materials ever discovered, graphene was only first isolated from graphite several years ago [5, 22], it has quickly become a "wonder" material in condensed matter physics field [23].

The linear energy-momentum relation of charges in single layer graphene and quadratic relation in bi-layer graphene are among the most interesting electronic properties of graphene. Beyond this, due to its remarkably high electron mobility [24, 25], special thermal [26], mechanical [27-30] and optical properties [31-34], graphene is a promising material with many potential applications, such as chemical and biological detection, components in integrated circuits, transparent electrodes, ultra-capacitors and quantum computers using anionic circuits [35].

1.6.1 Graphene Lattice structure

Graphene is an allotrope of carbon, consisting of one-atom-thick planar sheets of sp^2-bonded carbon atoms that are densely packed in a honeycomb crystal lattice. Each carbon atom has six electrons which occupy the atomic orbitals $1s^2$, $2s^2$ and $2p^2$. The two electrons in the $1s^2$ orbital are strongly bonded; the four remaining valence electrons $2s$, $2p_x$, $2p_y$ and $2p_z$ (excitation of one $2s$ electron into $2p_z$) have very similar energies, hence their wavefunctions can mix up in a process called hybridization. The resulting states are shown in Fig. 1.10. Three states lie in the xy-plane and the adjacent two has an angle of 120^o. These are the so-called σ states that form covalent bonds with their neighbors and give rise to the hexagonal lattice structure of graphene. The remaining state is the $2p_z$ orbital, the π state, is aligned to the z-direction. Electrons in this state are weakly bonded and can hop easily between neighboring atoms.

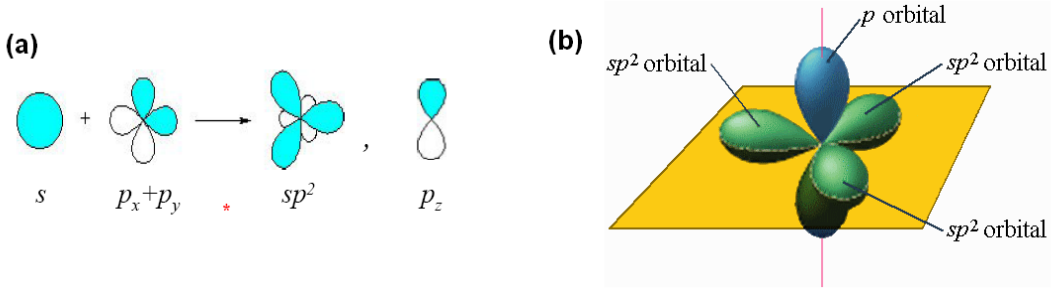

Fig. 1-10 (a) By combining the s-orbital with two p-orbitals, three sp2 orbitals plus a single p orbital are produced, each containing a single electron. (b) The shape of an SP^2 hybridized orbitals

As shown by Figure 1.11(a), graphene is monolayer of carbon atoms arranged by honeycomb lattice. Such lattice can be seen as a triangular lattice with a basis of two atoms per unit cell (Here gray rhombus and hexagon indicate two representations of the unit cell, each containing two atoms).

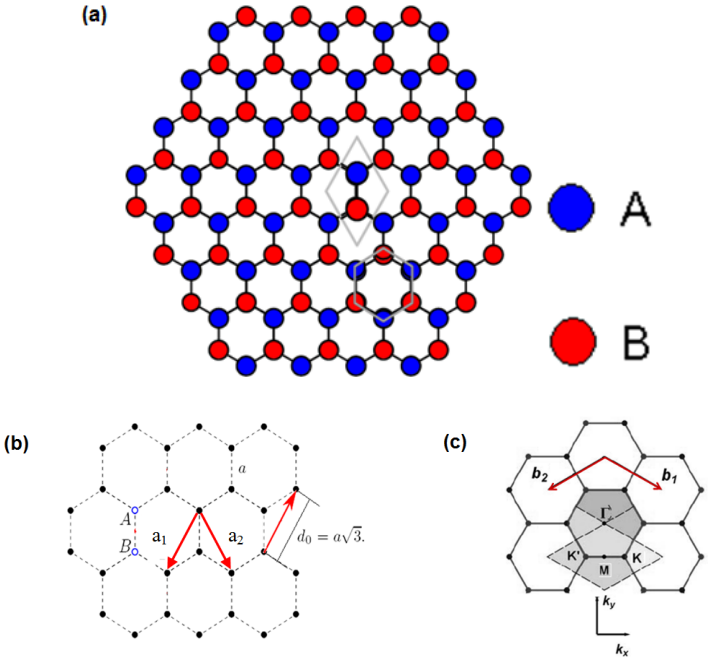

Fig. 1-11 (a) Graphene hexagonal lattice. The gray rhombus and hexagon are two representations of unit cell. (b) Real space of Graphene lattic with primitive vectors. (c) Graphene reciprocal lattice with primitive reciprocal vectors and high-symmetry points Γ, K and M.

The graphene lattice has two primitive vectors (as shown in Fig. 1.11(b)):

$$\vec{a}_1 = a_0(\frac{\sqrt{3}}{2}, \frac{1}{2}), \quad \vec{a}_2 = a_0(\frac{\sqrt{3}}{2}, -\frac{1}{2}),$$

where a_0 =2.46Å is the lattice spacing constant. Correspondingly the primitive reciprocal lattice vectors are given by (as shown in Fig. 1.11(c)):

$$\bar{b}_1 = \frac{1}{a_0}\left(\frac{2\pi}{\sqrt{3}}, 2\pi\right), \quad \bar{b}_2 = \frac{1}{a_0}\left(\frac{2\pi}{\sqrt{3}}, -2\pi\right).$$

Here we notice that $\bar{a}_i \cdot \bar{b}_j = 2\pi\delta_{ij}$, which satisfies the standard definition of reciprocal space. In Fig. 1.1**1**(c) there are two high-symmetry inequivalent *K* points at the corners of the hexagonal Brillouin zone labeled *K* and *K'*.

1.6.2 Unique Dispersion Relation of Graphene

Given that the honeycomb lattice of graphene has two atoms per unit cell, one can use Bloch's theorem to write down the eigenstate of the lattice Hamiltonian. The tight-binding approximation uses linear combinations of atomic wavefunctions to calculate the wavefunction for the lattice,

$$\begin{aligned}\psi^k(\bar{r}) &= c^A(\vec{k})\psi^{Ak}(\bar{r}) + c^B(\vec{k})\psi^{Bk}(\bar{r}) \\ &= \frac{1}{\sqrt{N}}\sum_j e^{i\vec{k}\cdot\vec{R}_j}[c^A(\vec{k})\phi(\bar{r}-\vec{R}^A) + c^B(\vec{k})\phi(\bar{r}-\vec{R}_j{}^B)]\end{aligned}$$

where N is the number of an elementary cell, and the functions $\phi(\bar{r})$ are the wavefunctions of the p_z orbitals of the carbon atoms. The coefficients c_l are chosen so that $\psi^k(\bar{r})$ is an eigenstate of the tight-binding Hamiltonian. $\vec{R}_j = n\vec{a}_1 + m\vec{a}_2$ indicates the positions of the A and B atoms, with $j = (n, m)$ specify the position of each graphene unit cell. The three nearest neighbor B atoms surrounding the A atom could be described as:

$$\boldsymbol{\tau_1} = a_0\left(\frac{\sqrt{3}}{2}, \frac{1}{2}\right), \ \boldsymbol{\tau_2} = a_0\left(-\frac{\sqrt{3}}{2}, \frac{1}{2}\right), \ \boldsymbol{\tau_3} = a_0\,(0, -1).$$

The Hamiltonian matrix ***H*** can be written as:

$$H = \begin{pmatrix} 0 & f(\vec{k}) \\ f^*(\vec{k}) & 0 \end{pmatrix},$$

where $f(k) = -t\sum_l e^{-i\vec{k}\cdot\vec{\tau}_l}$, where t is the nearest neighbors hopping energy ≈2.8 eV.

From $H\psi(r) = E(k)\psi(r)$, the energy bands are derived to be:

$$E_{\pm}(k) = \pm\left|f(\vec{k})\right| = \pm t\sqrt{1+4\cos^2\frac{a_0}{2}k_x + 4\cos\frac{a_0}{2}k_x\cos\frac{\sqrt{3}a_0}{2}k_y}\ .$$

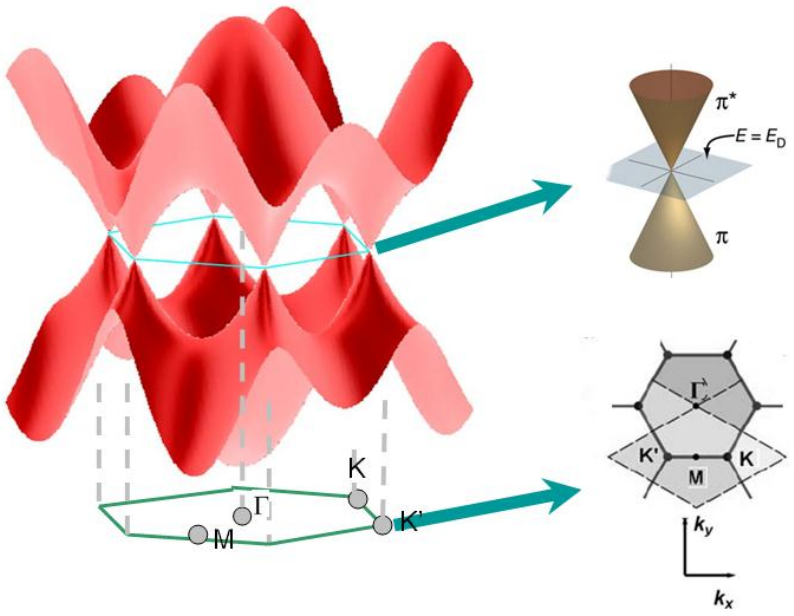

Fig. 1-12 Energy dispersion relation of graphene. Right top: linear dispersion relation close to Dirac points. Right bottom: corresponding high symmetric points in *k*-space.

Clearly, at K and K' points, $E_{\pm}(K) = E_{\pm}(K') = 0$. In their vicinity, after Taylor expansion in terms of $\Delta k = \left|\bar{k} - \bar{K}^{(')}\right|$ we obtain conical dispersion relation corresponding to relativistic massless Dirac Fermions as shown in Figure 1.12:

$$E_{\pm}(\bar{k}) = \pm\frac{\sqrt{3}}{2}a_0 t\left|\bar{k} - \bar{K}^{(')}\right| = \pm\hbar v_F\left|\bar{k} - \bar{K}^{(')}\right|,$$

where $v_F = \sqrt{3}\, a_0 t/2 \approx 1\times10^6$ m/s, or 1/300 the speed of light in vacuum. Such a linear dispersion relation is in contrast to the usual parabolic case $E = \frac{\hbar^2 k^2}{2m^*}$ in metals and semiconductors, where *m** is the effective mass of the charge carriers. Therefore charge carriers in graphene behave like relativistic particles with an effective speed of light given by the Fermi velocity. This behavior is one of the most intriguing aspects about graphene, and underlies the tremendous interest generated by graphene.

1.6.3 Chirality of graphene

We notice that for electrons within ~1eV of the Dirac point K, the Hamiltonian resembles that of low-energy massless Dirac fermions:

$$H_k = \hbar\begin{pmatrix} 0 & k_x - ik_y \\ k_x + ik_y & 0 \end{pmatrix} = \hbar v_F \vec{\sigma}\cdot\vec{k}\,.$$

Similarly, close to the K' point, $H_{k'} = \hbar v_F \vec{\sigma}^*\cdot\vec{k}$, where $\vec{\sigma}$ is the Pauli matrices and * denotes the complex conjugate. $\vec{\sigma}$ describes a quantity that is analogous to, but completely different from the 'real' spin, therefore is named "pseudospin", and it accounts for contributions from different sublattices A and B.

This special effect is also called chirality which has another physical description: the propagating direction and phase of an electron in *k*-space are not independent.

The concepts of chirality and pseudospin are important because many electronic processes (such as Klein tunneling [36-38]) in graphene can be understood as a consequence of the conservation of these quantities.

An alternative view on the origin of the chirality in graphene is based on the concept of "Berry phase" [2, 39, 40]. Since the electron wave function is a two-component spinor, it has to change sign when the electron moves along the closed contour. Thus the wave function gains an additional phase π.

This Berry's phase can further be probed in the magnetic field regime in single layer graphene, in which a semi-classical magneto-oscillation description holds:

$$\Delta R_{xx} = R(B,T)\cdot\cos[2\pi(B_F / B + \tfrac{1}{2} + \beta)] .$$

Here *R(B,T)* is the SdH oscillation amplitude, B_F is the frequency of the SdH oscillation in 1/B, and β is the associated Berry's phase. β=0 (or 1) corresponds to the trivial case, and β=1/2 is an indication of new physics, implying the existence of Dirac particles.

The band structure of bilayer graphene is gapless and the fermions in BLG, as in SLG, are also chiral but with a Berry phase equal to 2π instead of π.

1.6.4 Stacking order of graphene

Bilayer is stacked in a regular Bernal AB configuration which is usually named as Bernal staking, while trilayer graphene (TLG) has two natural stable allotropes: (1)

ABA or Bernal stacking, where the atoms of the topmost layer lie exactly on top of those of the bottom layer (Fig. 1.13a); and (2) ABC or rhombohedral stacking, where one sublattice of the top layer lies above the center of the hexagons in the bottom layer (Fig. 1.13b).

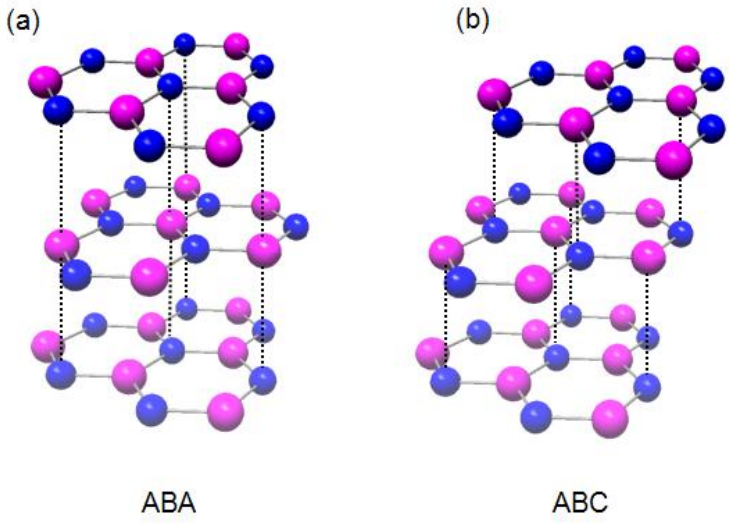

Fig. 1-13 ABA (B-stacked) and ABC (r-stacked) stacking of TLG

This subtle distinction in stacking order results in a dramatic difference in band structures. The dispersion of B-TLG is a combination of the linear dispersion of single layer graphene (SLG) and the quadratic relation of bilayer (BLG) (Fig. 1.14a), whereas the dispersion of r-TLG is approximately cubic, with its conductance and valence bands touching at a point close to the highly symmetric K and K' points (Fig. 1.14b) [41-44].

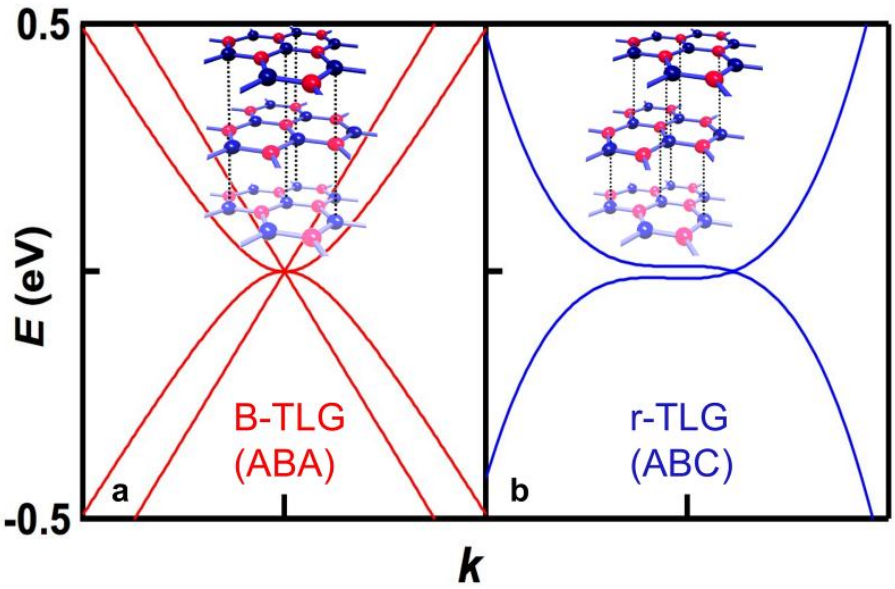

Fig. 1-14 (a) and (b): Band structures (main panel) and schematics (inset) of B- and r-stacked TLG, respectively.

1.6.5 Mechanical Properties of graphene

The static mechanical properties of an isotropic 2D membrane are described by four parameters: the in plane Young's modulus *Y*, the Poisson ratio ν, the breaking stress/strain, and the bending rigidity *B*. These parameters are detailed in table 1.1, and they dictate, *e.g.* response to strain, bending rigidity, or the resonant frequency of a graphene nanoelectromechanical resonator [28, 45], etc.

Graphene's static mechanical properties are as impressive as its electrical properties. As of 2009, graphene appears to be one of the strongest materials ever tested [30]. Measurements have shown that graphene has a breaking stress 200 times greater than steel, with a 2D tensile stress of 42 N/m corresponding with a stran of 25%. Its Young's modulus is about 1000 GPa, which also differs from that of the

bulk graphite.

	definition	formula
Young's modulus	The relation between the linear restoring force σ_x in a membrane due to a linear (uniaxial) strain ε_x on the membrane.	$\sigma_x = -Y\varepsilon_x$
Poisson ratio	A measure of how much a membrane contracts along a direction perpendicular to an applied (uniaxial) strain. (for a perfectly incompressible object since it deformes elastically at small strains it would have a Poisson's ratio of exactly 0.5, and for a very soft object it is almost 0.)	$\varepsilon_y = -\nu\varepsilon_x$
Breaking stress/strain	The point at which the graphene membrane breaks due to in-plane stress/strain.	
Bending rigidity	The amount of energy per unit area needed to bend an object. (R is a radious of curvature, A is area)	$\frac{E_{bend}}{A} = \frac{B}{2}\frac{1}{R^2}$

Table 1-1 Expression of parameters related with material's mechanical properties

From these values, we can see that graphene is very strong and rigid, and is a promising candidate for NEMS applications such as pressure sensors and resonators. Another interesting feature in graphene is its susceptibility to ripple formation [46-53], that arises from the nonlinear coupling of the bending modulus to the strain

in a membrane through the Poisson ratio. This will be discussed in details in chapter 7.

Chapter 2. Fabrication and Experimental Setup

In this chapter I will describe some essential techniques for graphene device fabrication. The most difficult aspects include:

1) Isolation and identification of graphene sheets from bulk graphite.

2) Fabricating electrodes with transparent contacts to graphene

3) Fabricating suspended graphene devices.

This chapter will start with the well-known “Scotch tape method” (section 2.1) followed by introduction of our improved “scratching exfoliation method” (section 2.2). We will then describe regular lithography fabrication in section 2.3.1 and finally a detailed introduction of an innovative lithography-free technique for singe gated (section 2.1.2) and double gated devices (section 2.1.2).

2.1 Graphene Exfoliation

The most well-known method to obtain exfoliated graphene is so-called “Scotch tape” or “mechanical exfoliation” method. It was well-known within the scanninng tunneling microcopy community that scotch tape can be used to peel layered compounds, though Geim group popularized this technique. It was described in an article in *Scientific American* in 2008 [54]: anyone with a chunk of graphite, a roll of scotch tape and a clean wafer can start to produce graphene in a few days.

Table 2.1 shows the scotch tape technique for producing graphene. The procedure is also demonstrated on Youtube:

http://www.youtube.com/watch?v=rphiCdR68TE.

1. Wafer preparation	1. Clean the Si/SiO_2 wafers by sonicating in acetone for ~15 minutes. 2. Remove wafers from acetone, rinse with isopropyl alcohol (IPA) and sonicate in IPA for 20 min. 3. Blow dry in nitrogen (N_2) gas.
2. Peel off thin graphite flakes onto tape	Attach a small piece of Kish graphite flake to single sided plastic sticky tape. Fold the tape right next to the flake so that you sandwich it between the tape's sticky sides. Press down then peel the tape apart slowly so that the graphite cleaves smoothly in two. Repeat until graphite spreads all over the tape. 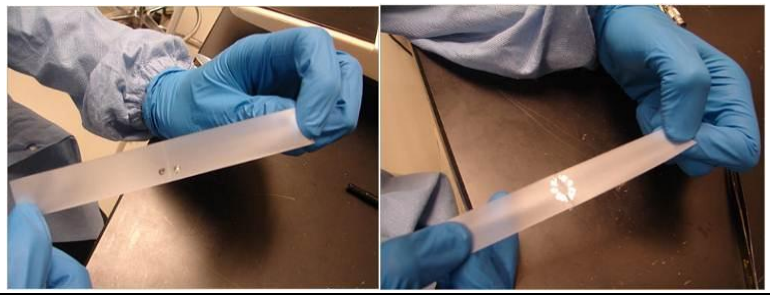
3. Attach tape to wafer then peel of the tape	Carefully lay the cleaved "graphite tape" onto the clean wafer. Using soft tools to gently press and squeeze out any air between the tape and sample. Then slowly peeling off the tape. 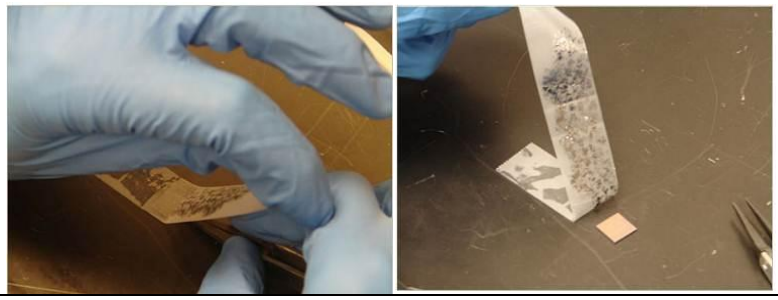

Table 2-1 Procedure of "Scotch tape" mechanical exfolication of graphene

During my five years of “exfoliation career”, I also developed another method to exfoliate relative large graphene flakes, which were used in all projects covered in this thesis. I named this method “scratching exfoliation” as described below:

Wafer preparation	Same as table 2.1
Peel off thin graphite flakes and attach them to wafer directly	1. Prepare a small stick such as L-wrench. 2. Use double-sided tape to attach a Kish graphite (or HOPG) to one end of the stick (make sure the tape is fully covered by graphite flake to prevent glue residues) 3. Use the scotch tape to peel and expose a fresh surface of the graphite. Then press it directly to a clean wafer.
Press and scratch	1. *First* use a soft object (better with surface covered by same graphite material) to rub on the peeled graphite until it is well adhered to the substrate surface. 2. *Then* use a clean and sharp knife to scratch the graphite, usually graphene flakes are located close to the areas that are scratched by the knife.

Table 2-2 Procedure of “scratching exfoliation” of graphene flakes

2.2 Graphene Location and Layer Identification

After mechanical exfoliation of graphene flakes on Si/SiO_2 wafers, we need to identify the number of graphene layers and locate their position for further device fabrication.

Si wafers cover by 300-nm thick SiO_2 yield the best color contrast for identifying graphene[55], thus allowing us to identify and locate graphene under optical microscope (Figure 2.1). The confirmation of single layer, bilayer graphene, and even trilayer graphene can be performed by either Raman spectroscopy [31, 34] or quantum Hall effect measurements [1, 2, 56].

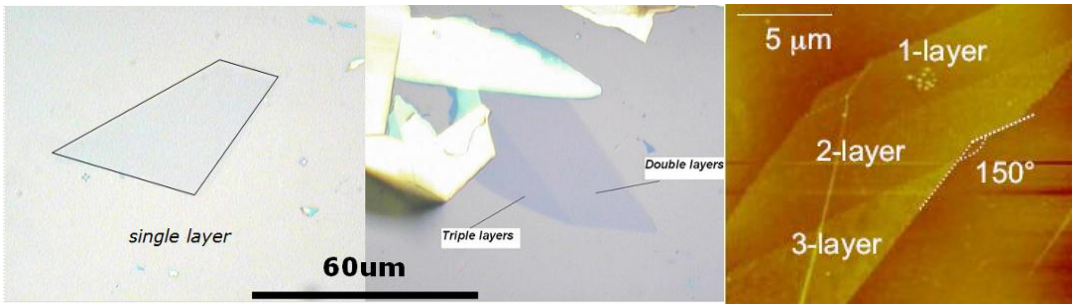

Fig. 2-1 (a) Optical microscope images of single layer graphene and (b) bilayer and trilayer graphene attached with a multiple layer bulk graphite. (c) AFM image of single layer, bilayer and trilayer graphene in serious.

Tapping mode Atomic Force Microscopy (AFM) is also used to observe mesoscopic features of the graphene flakes, as shown in Figure 2.1 c. The measuree thickness of single layer graphene flake is around 0.8-1 nm, which is larger than graphite interlayer spacing 0.34 nm, possibly because of the presence of a “dead”

layer (such as water or contaminants) on graphene or between graphene and the substrate.

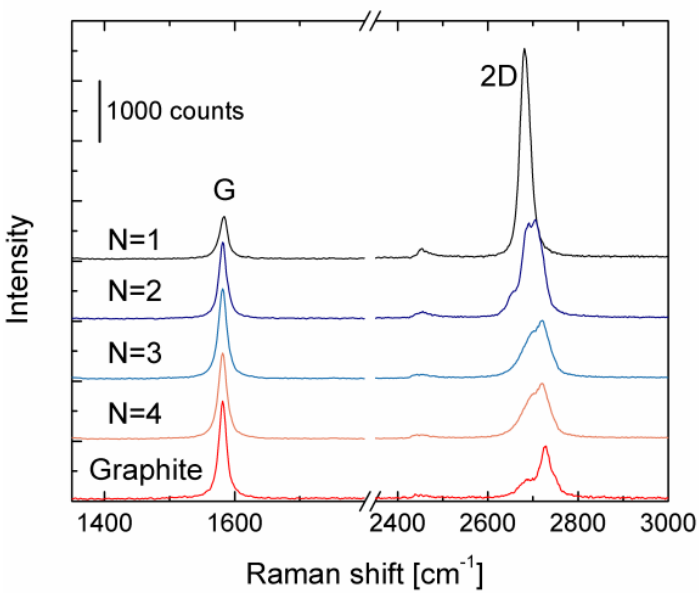

Fig. 2-2 Layer dependence of graphene Raman spectrum. Figure adapted from (Yu, 2010).

2.3 Electrodes Fabrication

To date mechanically exfoliated graphene has much higher quality than that of CVD grown graphene. Thus current electrical transport studies mainly focus on exfoliated graphene based devices. In the next three sections we will demonstrate fabrication procedures of electrically contacted graphene devices. We will give a detailed description of the lithography-free processes and highlight the key innovations in this method.

2.3.1 Electron-beam lithography fabrication

We usually use electron-beam lithography (EBL) to pattern electrodes with complicated geometries. Two steps of EBL are necessary for patterning graphene devices: the first step puts a large array of alignment marks (Ti) close to targeted graphene for accurate alignment in the second step that patterns electrodes. Between these two steps of EBL, we anneal our devices in a furnace at 300°C in oxygen, in order to clean resist residues induced by the first EBL step. We found that this step is very important for obtaining good electric contacts between electrodes and graphene.

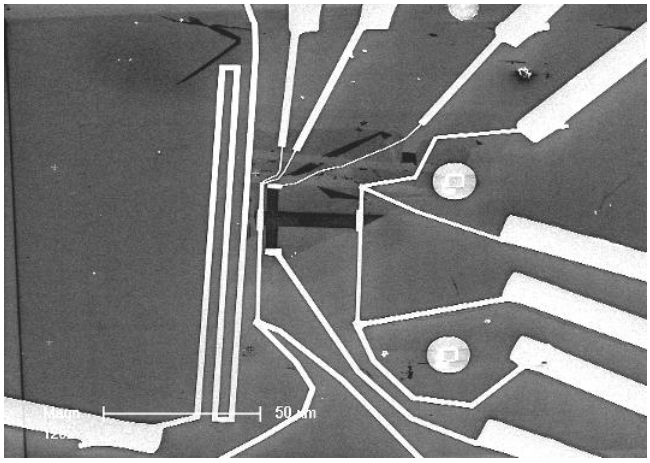

Fig. 2-3 An SEM image of a graphene device whose geometry was designed for thermal power measurement. Notice that two allignment marks are coverd by circular metal due to the exposure during the second step of EBL.

The standard EBL fabrication processes consist of several steps described in table 2.3 and shown in Fig. 2.4.

1	Spin coat MMA/PMMA double layer Ebeam resist (8.5 MMA EL 9 and PMMA 950 A4 from Microchem) and bake at 170°C for 10 minutes for each layer.
2	Perform EBL (LEO SUPRA 55) to pattern designed electrodes designed by DesignCAD LT2000 (typical area dosage used is ~460 nC/cm^2 for 120pA beam current to write patterns smaller than 20 μm. For bonding pads, typical area dosage used is ~400 nC/cm^2 for 4300pA beam current to write features smaller 150 μm). Develop samples in Methyl Isobutyl Ketone/Isopropyl Alcohol **(**MIBK/IPA) (1:3) for 65 seconds followed by 1-min rinsing in IPA.
3	Deposit electrodes metal in Ebeam evaporator (Temescal BJD 1800 system); the pressure of vacuum during evaporation is usually below 8×10^{-6} torr. A 5-nm adhesion layer of Ti or Cr is deposited at a rate of ~1Å/s, followed by 50nm of Al or Au at a rate of ~2 Å/s.
4	Immerse samples in hot acetone (60°C to 80°C) for ~3 hours. Then rinse the samples in IPA for a few minutes and blow them dry in N_2 gas. Metals deposited on unexposed resist will be lifted off.

Table 2-3 Procedure of E-beam lithography for graphene devices.

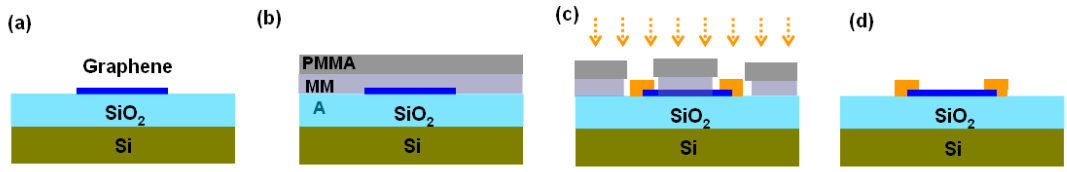

Fig. 2-4 Schematics of EBL fabrication. (a) Graphene flake on SiO_2/Si substrate; (b) Spin coating double layers of positive electron-beam resist; (c) Electron-beam exposure on pre-designed regions; followed by metal evaporation; (d) Lift-off metals deposited on unexposed resist.

2.3.2 Lithography-free electrodes fabrication for single gated devices

Lithographical processes described above, which have been used to fabricate almost all graphene devices to date, are known to be detrimental to the mobility of graphene devices. As graphene consists of only a single atomic layer, it is particularly sensitive to surface contaminants, including resist residues left by lithographical processes, which locally modify the electrochemical potential and provide extra scattering sites [57, 58]. Though annealing techniques have been demonstrated to improve device mobility [58, 59], they are not well-controlled and do not always produce consistent results. Lithography-free fabrication techniques have been reported [60, 61]; however, the procedures are complicated and yield devices that are restricted to simple geometries. We develop a lithography-free device fabrication technique [62] for graphene devices, via metal evaporation through silicon hard masks. This technique is simple, inexpensive, and does not require any resist processing; thus, it greatly increases device throughput, produces

transparent contacts between graphene and electrodes, and yields high quality graphene devices. Additionally, hard masks, and hence devices, with complex patterns can be readily fabricated. Using this technique, we fabricate both substrate-supported and suspended devices.

The first and most crucial step in our fabrication procedure is the synthesis of hard silicon shadow masks, as illustrated in Fig. 2.5(a). Here we use 500-μm double-side-polished, {100} orientation silicon wafers that are 1 x 1 cm^2 in size. Firstly, a 200-nm layer of chromium is evaporated on one side of the wafer, followed by the deposition of a thin layer of poly (methyl methacrylate) (PMMA) E-beam resist. This chromium layer will serve as an etching mask for later KOH and inductively coupled plasma (ICP) etching processes. Since controllable etching of thick (>100-μm) Si layer is difficult, we reduce the thickness for the final pattern etching by using photolithography and KOH etching to open a large, 400-μm deep window on the *back* of the wafer, leaving a 100-μm thick Si layer to be etched in the final step. The shadow mask structure is then patterned on the front side using e-beam lithography. After exposing and developing the resist, we use a chromium etchant (1020AC) to remove the exposed chromium layer. Finally, the shadow mask is completed by using ICP to etch through the exposed silicon layer, creating a Si wafer with patterned openings.

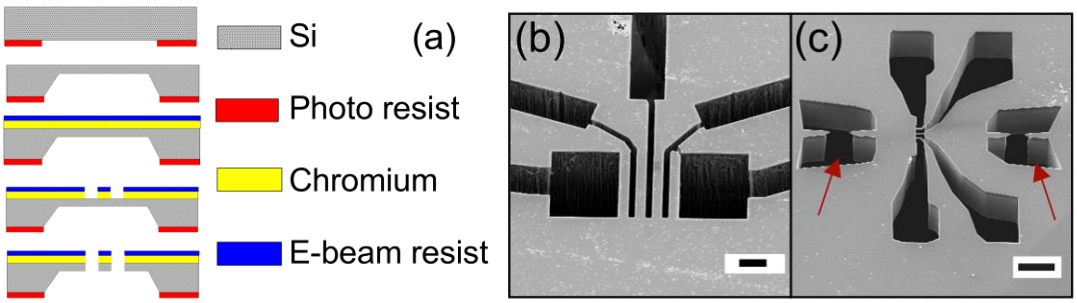

Fig. 2-5 Fabrication of silicon shadow masks. (a). Schematic illustration of the fabrication process. (b, c). SEM images of two silicon shadow masks. The red arrows in (c) indicate the alignment windows. Scale bars: 5 μm and 50 μm respectively.

SEM images of two ready-to-use silicon shadow masks with different geometries are shown in Fig. 2.5 (b) and (c). Features as small as 100 nm can be reliably fabricated. The masks typically also contain alignment windows that assist with precision alignment during fabrication, as indicated by the red arrows in Fig. 2.5(c). These shadow masks are exceedingly robust, and can be used more than 50 times. We note that traditional shadow masks, which consist of silicon nitride Si_3N_4 membranes that are partially released from Si substrates [63-66], often exhibit distorted edges [63, 65, 66]. In contrast, our silicon shadow mask has a flat sample-contacting surface, and is sufficiently rigid for complicated structures such as Hall bar geometries as shown in Fig. 2.6.

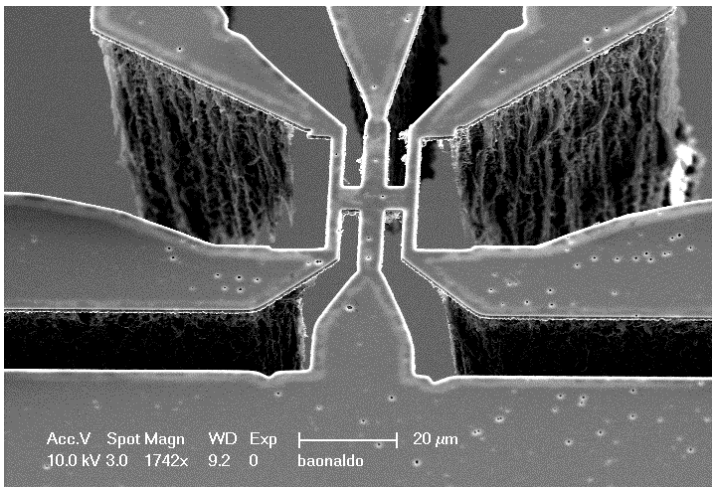

Fig. 2-6 Si shadow mask with Hall bar geometry.

To fabricate graphene devices, we exfoliate graphene sheets on standard Si/SiO_2 wafers. With the help of alignment windows, we use micromanipulator XYZ translation stages to carefully align the shadow mask to identified graphene sheets, and then place the entire assembly in a vacuum chamber as shown in Fig. 2.7(a) for further metal deposition. The mask nominally rests closely on the substrate (Fig. 2.7b and c), though the effective mask–substrate separation, which is typically about few hundred nanometers, is determined by the thickness of the graphite residues on the substrate surface.

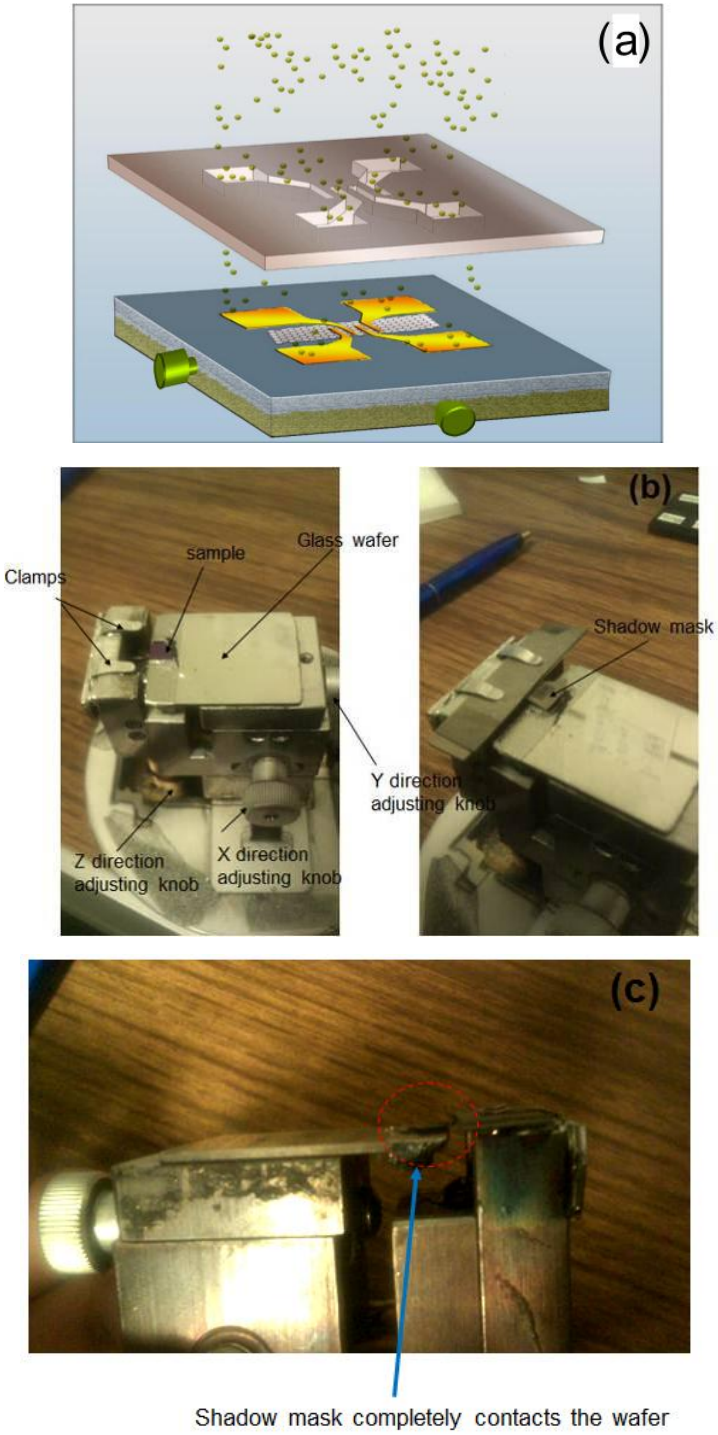

Fig. 2-7 (a) Graphene devices can be fabricated by direct deposition of metallic electrodes through these masks. (b,c) top and side views of shadow mask and sample combination.

In completed devices, we find that the metal electrodes typically extend beyond the shadow mask openings by ~0.2–0.5 μm, due to the extended size of the metal source and the finite mask–device separation, which is illustrated in Fig. 2.8.

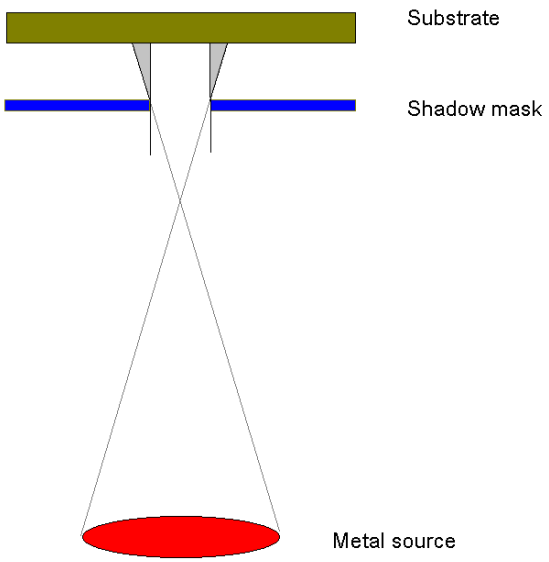

Fig. 2-8 Schematic of metal diffusion, The gray area indicates an extension of metal deposition.

To compare the qualities of graphene devices made by conventional E-beam lithography and shadow mask evaporation, we fabricate devices using both techniques *on the same graphene sheet*. To this end, we use a shadow mask to deposit four electrodes (labeled A, B, C, D in Fig. 2.9), and subsequently e-beam lithography to deposit three additional electrodes (E, F and G in Fig. 2.9), on a single-layer graphene sheet. The electrodes are designed to yield devices with

similar aspect ratios. After *each* fabrication, the device was characterized by atomic force microscope (AFM) imaging and electrical measurements.

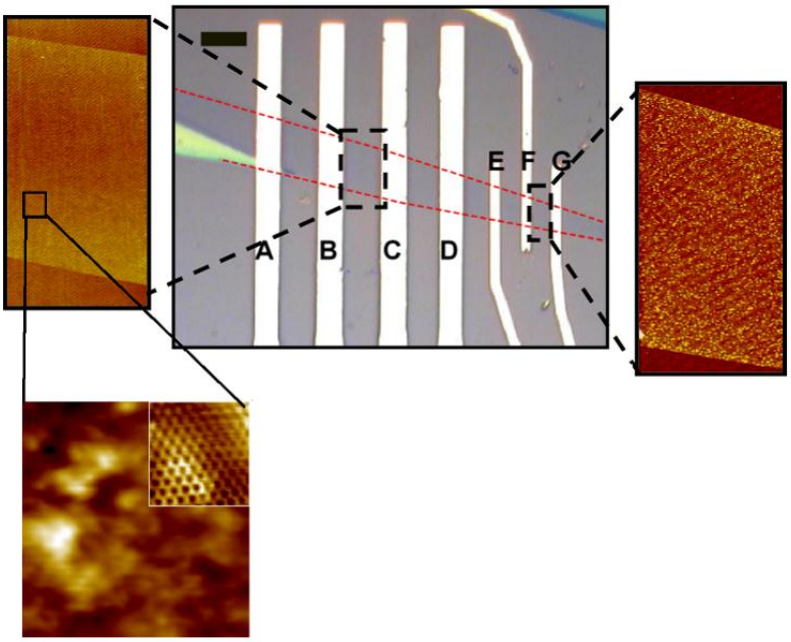

Fig. 2-9 Optical and AFM (side panels) images of a single-layer graphene sheet device. The electrodes A, B, C and D were deposited by evaporation through a shadow mask, and E, F and G were fabricated using standard electron beam lithography. Scale bar in the optical image: 5 μm. Left lower is an STM image of an as-fabricated device using the shadow mask technique. The main panel displays an image of 85 nm x 85 nm area, and the inset shows the atomic lattice over an area of 2.5 nm x 2.5 nm.

The right panel of Fig. 2.9 displays an AFM image of the graphene surface after lithography, revealing a thin layer of resist residue. The device was annealed in an H_2/Ar atmosphere at 200 ℃ for 45 minutes to remove the contaminants. Using standard lock-in techniques, the two-terminal conductance, G, of the devices were measured as a function of the back gate voltage, V_g, that controls the density n and

type of the charge carriers. The device mobility μ was calculated from the slope of the plots of G vs. V_g:

$$\mu = \frac{W}{L}\frac{t}{\varepsilon}\frac{\Delta G}{\Delta V_g},$$

where t is the thickness of the silicon oxide layer, W and L are the width and length of the source-drain channel and ε=3.9 is the dielectric constant of silicon oxide. For a typical device fabricated by lithography, μ was found to be 1500 and 3000 $cm^2/(V\ s)$ at room temperature and 4.2 K, respectively (Fig. 2.10 (b)).

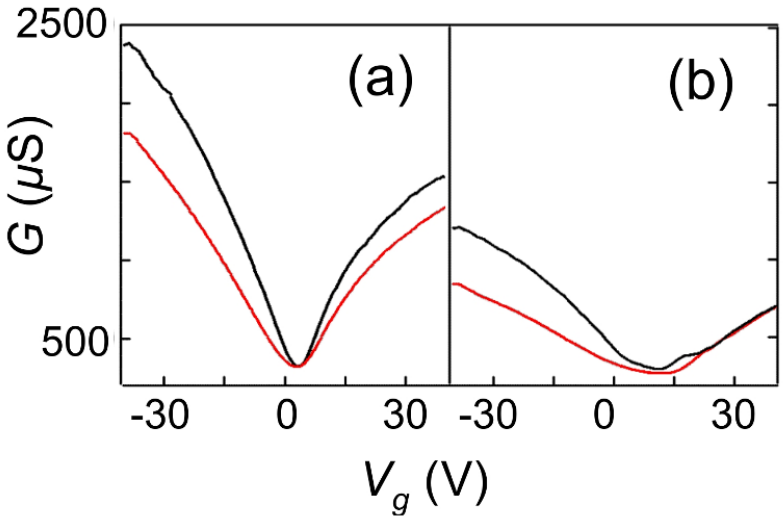

Fig. 2-10 Plots of two-terminal conductance (G) vs. back gate voltage (V_g) for the electrode pairs (a) BC and (b) FG at room temperature (red) and 4.2 K (black).

In contrast, for devices fabricated by shadow mask evaporation, the graphene surface remains clean after evaporation, as shown by the AFM images (left panel, Fig. 2.9). Atomic resolution images of the honeycomb lattice over large areas can be

obtained using scanning tunneling microscopy, without any annealing treatment (Fig. 2.9 left lower). From transport measurements, the device mobility is ~4000 $cm^2/(V\ s)$ at room temperature, and increases to ~7000 $cm^2/(V\ s)$ at 4.2 K (Fig. 2.10(a)). Thus, eliminating lithography yields devices with significantly higher mobility.

This shadow mask technique can be applied to fabricate devices with a variety of geometries. As another demonstration of its power and versatility, we extend it to the fabrication of suspended devices via two complementary methods. In the first technique (Fig. 2.11a–c), a completed device supported on a substrate was fabricated on the substrate, followed by etching by hydrofluoric acid (HF), which releases the graphene sheet from the SiO_2 layer, and critical point drying. Here the Cr/Au electrodes double as etch masks, and HF etches anisotropically and preferentially along graphene [25], resulting in suspension of the entire graphene sheet. The HF-etched devices are annealed using current-induced Joule heating [59]. The mobilities were found to be 20,000 and 120,000 $cm^2/(V\ s)$, respectively, at room temperature and 4.2 K. The plots of G vs. V_g display pronounced sub-linear curvature, indicating the high mobility of the material [24, 25] (Fig. 2.11d).

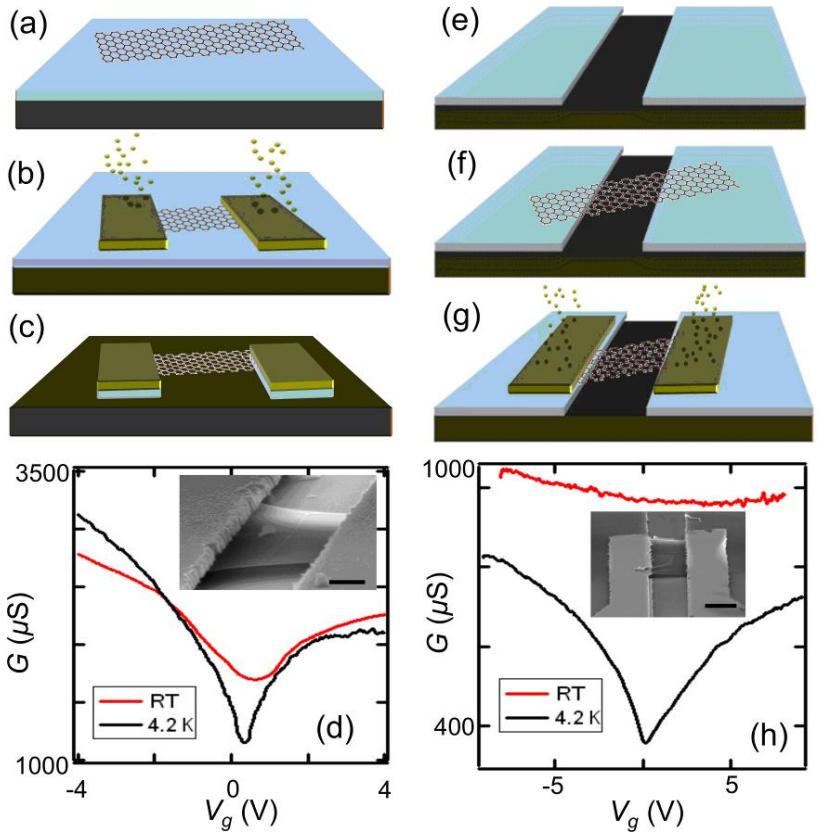

Fig. 2-11 (a–c) Fabrication of suspended graphene devices via HF etching. (d) Plots of two-terminal conductance (G) vs. back gate voltage (V_g) for an HF-released single layer graphene device at room temperature (red) and 4.2 K (black). Inset: SEM image of such a device. Scale bar: 1 μm (e–g) Fabrication of suspended graphene devices over pre-defined trenches on the substrate. (h) Plots of G vs. V_g for a bi-layer graphene device over a trench at room temperature (red) and 4.2 K (black). Inset: SEM image of such a device. Scale bar: 3 μm

Using the second technique to fabricate suspended devices, a graphene sheet is directly exfoliated across pre-defined trenches on the substrate; electrodes are deposited by evaporating through shadow masks that are carefully aligned with the trenches (Fig. 2.11e–g). The inset in Fig. 2.11(h) shows an image of a bi-layer device fabricated using this technique. Since these suspended devices do not undergo any chemical processing, they are extremely clean. The device mobility of this

bi-layer device was measured to be ~2000 $cm^2/(V\ s)$ at room temperature, and 60000 $cm^2/(V\ s)$ at 4.2 K (Fig. 2.11h).

In conclusion, we have demonstrated a lithography-free technique for fabrication of high quality graphene devices, which may be either substrate-supported or suspended. Applications of this technique include ultra-clean devices for scanning tunneling microscope (STM) and optical measurements, or devices coupled to specialized (e.g. superconducting or ferromagnetic) electrodes. In particular, it provides an especially powerful approach for investigation of the mobility bottleneck for graphene devices, as it allows fabrication of ultra-clean devices that are free of both lithography contaminants and substrates.

2.3.3 Lithography-free double gated electrodes fabrication

Doubly gated suspended devices (Fig. 2.12) are capable to independently control perpendicular electrical field $E_\perp$ and charge carrier density n. Using Eq. (2.1) and (2.2) we can tune $E_\perp$ and n independently in the suspended BLG by applying top and back gate voltages V_{tg} and V_{bg}.

$$E_\perp=(\alpha V_{tg}-\beta\ V_{tg})/2e\varepsilon_o \tag{2.1}$$

$$n_{tot}=(\alpha V_{bg}+\beta\ V_{tg}) \tag{2.2}$$

Fig. 2-12 Schematic diagram of doubly suspended graphene device

This fabrication technique is based on basic shadow mask fabrication method described in the last section. Fig. 2.13 illustrates the entire fabrication process. We first exfoliate graphene sheets on Si/SiO_2 (500 μm/300 nm) wafers with pre-patterned trenches which are 250nm in depth (Fig. 2.13b), then source and drain electrodes are fabricated by direct deposition of Ti/Au (5nm/100nm) metals through shadow masks that are carefully aligned to selected suspended graphene sheets (Fig. 2.13c). Subsequently, another piece of Si/SiO_2 (100 μm / 300nm) wafer is added with the SiO_2 surface contacting the whole device (Fig. 2.13e). The two wafers are then combined by epoxy. We note that the separation between two wafers is usually limited by dust particles left between wafers, therefore the surface of wafers need cleaning and whole process is performed in cleanroom. A smaller size of the top wafer is also preferred to decrease this separation.

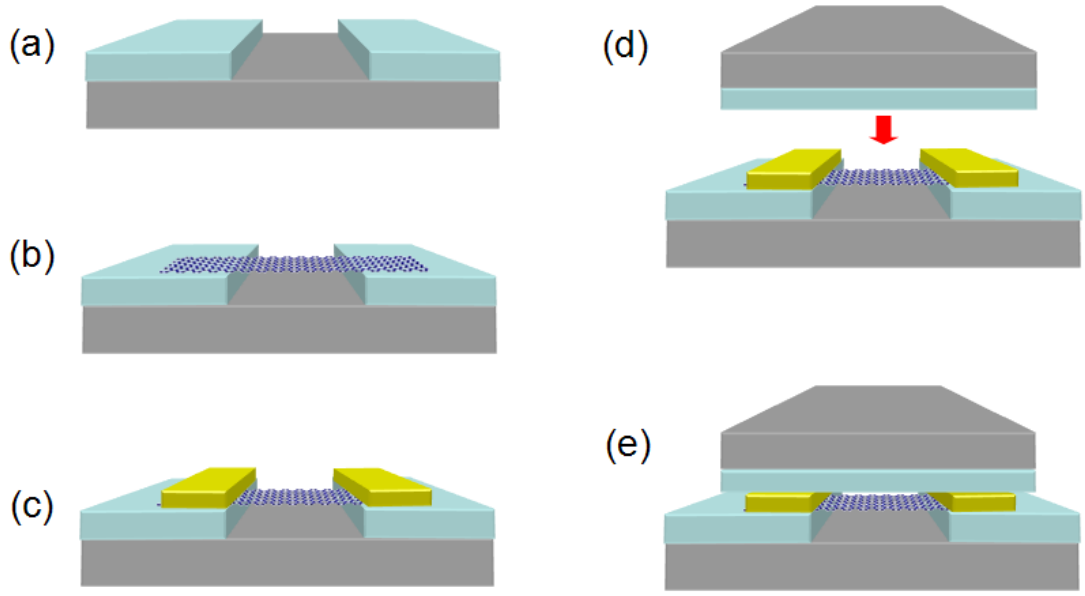

Fig. 2-13 Fabrication procedure of doubly suspended graphene device.

2.4 Experimental Setup

After successful fabrication of graphene devices, we first mount them onto chip carriers and use wire-bonder to connect electrodes to carrier's pins, then insert the whole chip carrier into our measurement system (He3 or He4 cryostat) and perform measurement. The procedures are detailed Ph.D. theses of Feng Miao[67] and Gang Liu[68].

Chapter 3. Proximity Induced Superconductivity in Graphene Josephson Transistors

Graphene coupled with superconducting electrodes yields graphene Josephson junctions. In this chapter, we will discuss our study of proximity induced superconductivity in graphene Josephson transistors.

We will start this chapter by introducing graphene Josephson junctions in section 3.1. Then we will discuss two main characteristics of graphene Josephson junctions -- multiple Andreev reflections and the proximity induced bi-polar supercurrent. We observed large depression in the critical current I_c and large variation in the product I_cR_n (where R_n is the normal state resistance of the junction) with gate voltage, in contrast to theoretical predictions in ballistic model. In section 3.4 we will investigate the important role of thermal fluctuations in electronic transport in graphene Josephson transistors. We will also introduce a RCSJ (resistively and capacitively shunted junction) model, in which the depression of I_c can be explained by premature switching in underdamped Josephson junctions. In section 3.5, we calculate the gate dependence of product I_cR_n by considering the effect of premature switching, and its agreement with experimental data shows evidence of premature switching in our graphene Josephson junctions. In the last section we briefly describe our efforts toward suspended graphene Josephson transistors.

3.1 Introduction of Graphene Josephson Junctions

Graphene can be easily coupled to special electrodes such as superconductors with controllable interfaces. Thus, coupling graphene to superconducting electrodes provides an ideal platform for investigating the interplay between superconductivity and relativistic quantum electrodynamics, which will be useful for understanding of high temperature and heavy-element superconductors[69]. Superconducting order is also predicted to emerge in pure and doped graphene [70].

Coupling superconducting electrodes to graphene yields a Josephson junction (JJ). In contrast to traditional JJ, in which the weak links are insulators, normal metals (N) or constrictions (Fig. 3.1(a)), a superconductor/graphene/superconductor (SGS) JJ consists of a 2D relativistic system with gate-tunable (and potentially ballistic) conductance (Fig. 3.1(b)) [71, 72].

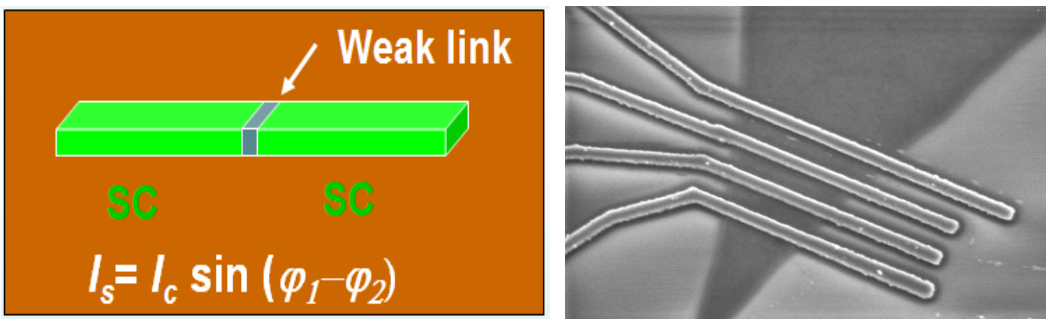

Fig. 3-1 (a) Schematic diagram of Josephson junction. (b) An SEM image of a graphene Josephson junction device.

Several unusual phenomena have been predicted to arise in this novel system, such as specular Andreev reflection [73], novel propagating modes of Andreev

electrons [74] and oscillation of tunneling probability with barrier width [75]. Experimentally, the observation of a bi-polar supercurrent and multiple Andreev reflection (MAR) in graphene Josephson junctions has been reported by several groups [76-78].

In SGS junctions, the electronic transport in graphene is strongly affected by the so-called proximity effect, in which Cooper pairs in superconducting electrodes penetrate into graphene and render it superconducting. Experimentally, proximity induced superconducting phenomena in graphene include multiple Andreev reflections and bi-polar supercurrent in graphene.

3.2 Multiple Andreev Reflections in Graphene

Andreev reflection is a type of particle scattering that occurs at interfaces between a superconductor (S) and a normal (N) state material, as illustrated in Fig. 3.2. During an Andreev reflection, an electron in the normal metal incident on the N/S interface is retro-reflected as a hole, while transferring charge 2*e* to the superconducting Cooper pair condensate [79].

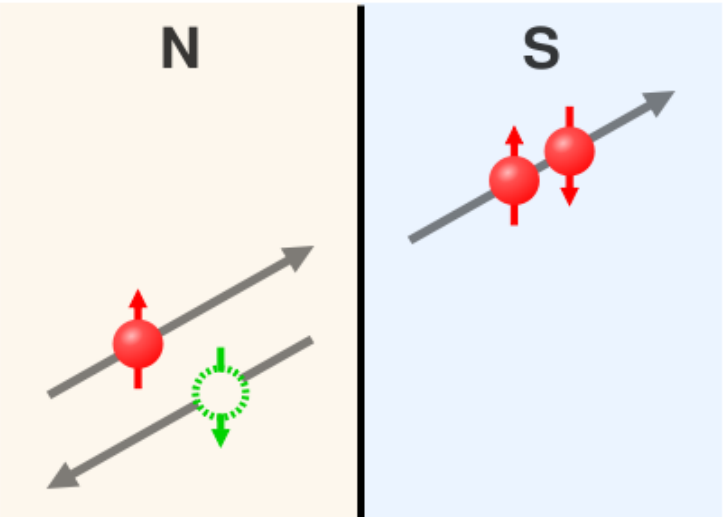

Fig. 3-2 An electron (red) meeting the interface between a normal conductor (N) and asuperconductor (S) produces a Cooper pair in the superconductor and a retro reflected hole (green) in the normal conductor. Vertical arrows indicate the spin band occupied by each particle

In SNS junctions, an electron in graphene can be reflected back and forth several times between the two N/S interfaces, gaining energy eV each time when it transverses the junction (electrons and holes, moving in opposite directions, are both accelerated by the bias voltage V), until it accumulates sufficient energy to exit graphene into a superconducting electrode as a quasiparticle (Fig. 3.3). Thus multiple Andreev reflection (MAR) gives rise to features [80].

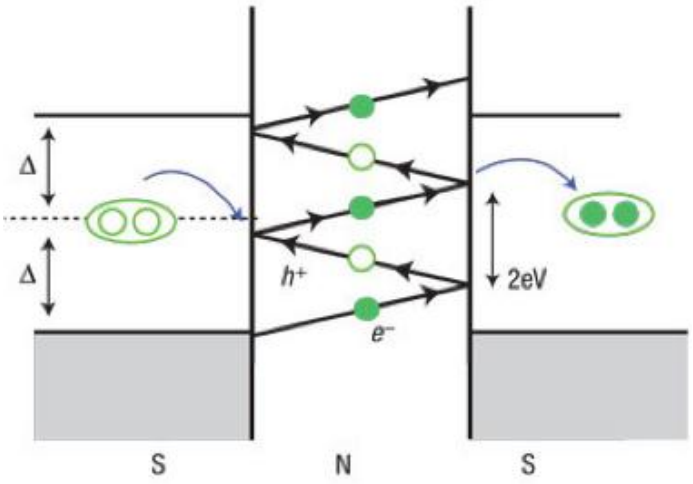

Fig. 3-3 Schematic energy diagram of the multiple Andreev reflection process in an SNS junction with an energy gap Δ. The electron is retro-reflected as a positively charged hole, creating a Cooper pair in the superconductor; conversely, retro-reflection of a hole *annihilates* a Cooper pair.

To observe MAR in SGS junctions, we measured differential conductance of devices as a function of voltage across the junction, as shown in Fig. 3.4, for a typical device at V_g=0V. The giant center peak at V=0 indicates the proximity-induced supercurrent. The peaks at V=±202 μV mark the onset of quasiparticle conductance and correspond to 2Δ, where Δ is the superconductor energy gap. Thus, for this SGS junction, we infer Δ=101 μeV, which is smaller than 180 μeV for bulk Aluminum. For our other devices, Δ ranges from 90 to 120 μV.

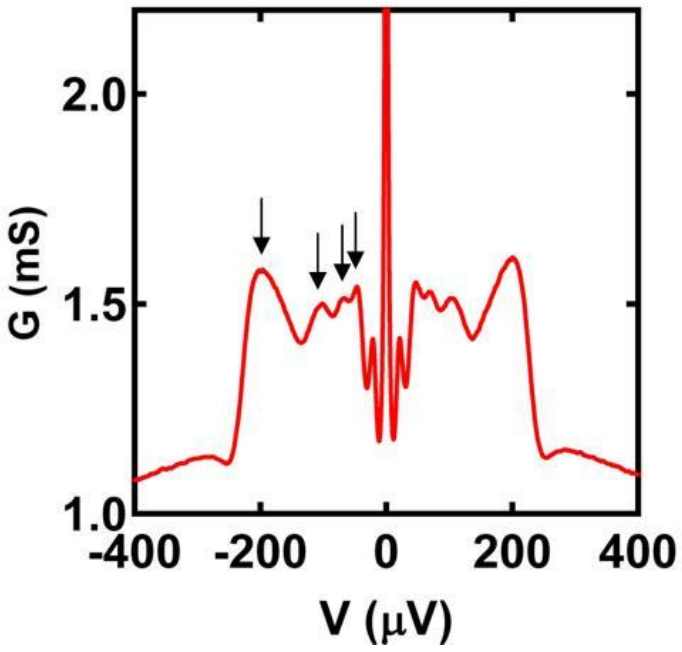

Fig. 3-4 Differential conductance vs. voltage showing MAR peaks corresponding to n = 1, 2, 3 and 4 (arrows, left to right).

At V<2Δ, there are a series of smaller conductance peaks and such sub-gap features arise from the phenomenon of MAR in conductance. This MAR gives subharmonic features [80] at differential conductance when bias $V_n=2\Delta/ne$, where Δ is the energy gap of superconducting electrode, n is an integer and e is electron charge. From Fig. 3.4, the sub-gap features occur at V=100, 68.7 and 47 μV, corresponding to n=2, 3 and 4, respectively. The observation of MAR demonstrates the high transparency of graphene/superconducting electrode interfaces. Similar observations were also reported by several other research groups [76, 77].

We also note that specular Andreev reflection was not observed in our SGS devices. In specular Andreev reflection, when the electron-hole conversion occurs at

the N/S interface, the trajectory of the reflected hole is specular to that of the incident electron. Just like in the more common retro-Andreev reflection, the electron is converted into a hole, but the reflection angle is inverted, as shown in Fig. 3.5.

This was predicted to occur in weakly doped graphene for $E_F << \Delta$, where Δ is the superconducting gap, and E_F is the Fermi energy. Thus, the Fermi wavelength in graphene is required to be large compared to the superconducting coherence length [73]. This regime is difficult to achieve experimentally, requiring very high mobility devices with extremely sharp Dirac point, and specular Andreev reflection has not been observed to date.

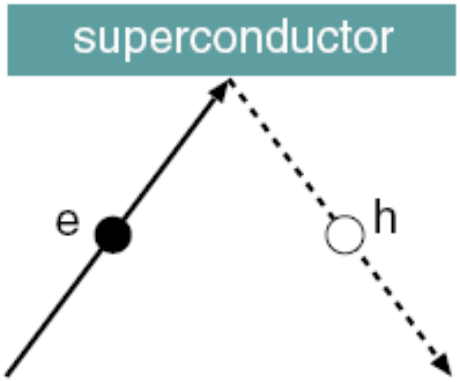

Fig. 3-5 Schematic diagram of the specular Andreev reflection process.

3.3 Bi-polar Supercurrent in Graphene

Besides MAR, the proximity effect is also evident from the observation of supercurrent in graphene Josephson junctions. We current biased the device and measured voltages dropped on graphene (color) as a function of both bias current

(*y*-axis) and gate voltage (*x*-axis), as plotted in Fig. 3.6 (a) and (c) for two different devices. The separations L between two electrodes of the devices are less than 300n. Supercurrent was observed in all devices (>10) with transparent graphene/superconducting electrode interfaces.

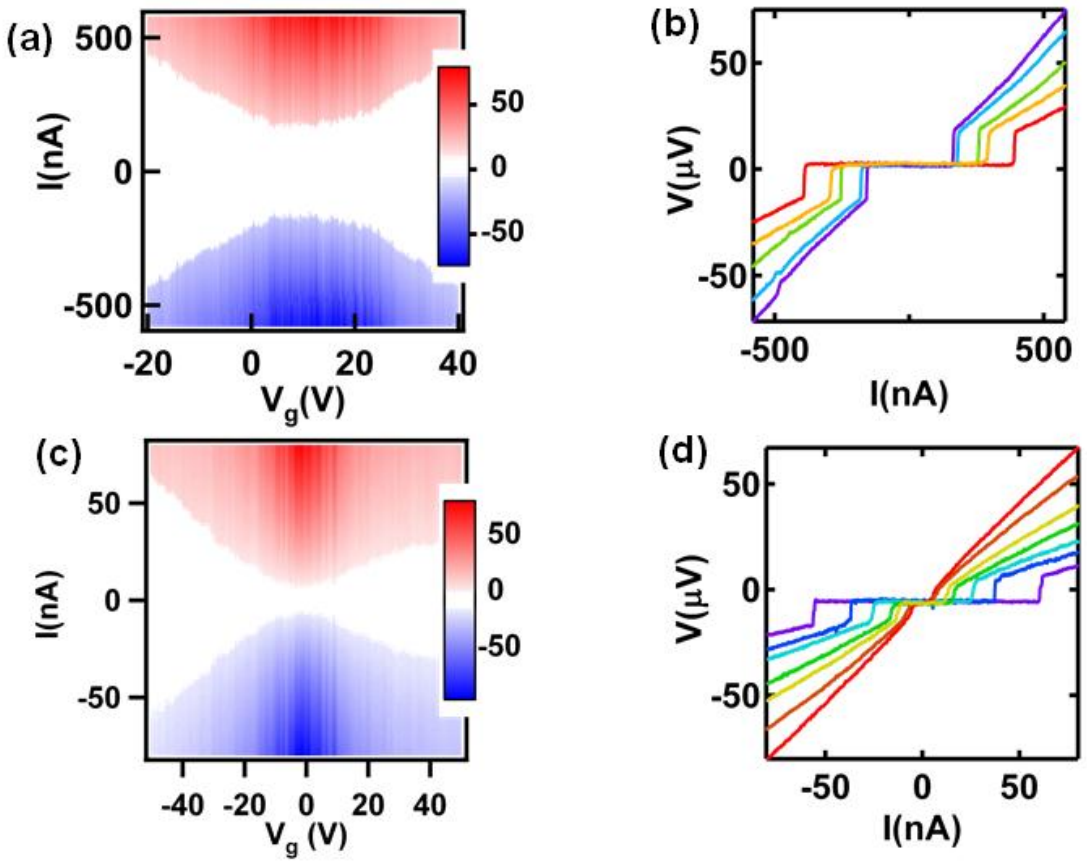

Fig. 3-6 Supercurrent in graphene. (a) Voltage across the junction as a function of biased current (*y*-axis) and gate voltage (*x*-axis). The color scale of voltage is in units of μV; (b) *V-I* line traces at different gate voltages taken from (a); (c) and (d) are the similar data sets from another device.

Strikingly, supercurrent is observed in electron-doped, hole-doped and even around the charge neutrality point which has nominally zero charge density. The

values of critical current, at which the junction switches from zero resistance state to a resistive state, are strongly dependent on the applied gate voltages, as shown by *V-I* curves at different gate voltages in Fig. 3.6 (b) and (d). For this particular device corresponding to Fig. 3.6 (a), the critical current is about 200nA around Dirac point and about 450 nA at highly doped regions. Similar observation of gate-dependent supercurrent in graphene has recently been reported by other groups [76, 77].

The observation of gate tunable supercurrent sets SGS junctions apart from conventional Josephson junctions, whose *V-I* characteristics are typically fixed at a certain temperature and magnetic field. In Josephson junctions, the critical current I_c is a parameter indicating the strength of the weak link between two superconducting electrodes, which is about $2\Delta/eR_n$ for diffusive SNS or S/Insulator/S (SIS) junctions or about $2\pi e\Delta/h$ for two superconductors coupled via a single quantum channel with perfect transmission [81]. Thus, both I_c and the product I_cR_n are expected to be constants for a given device, and the latter is only determined by the energy gap Δ of superconducting electrodes. However, for SGS junctions, both quantities are gate dependent, as shown in Fig. 3.6 (a) and (b).

Josephson effects in graphene were first calculated for the ballistic case in reference [82] as shown in Fig. 3.7(a) Here μ stands for Fermi energy, which is related to gate voltage by

$$E_F = \upsilon_F \sqrt{\pi \cdot 7.2 \times 10^{10} \cdot V_g} ,$$

where $\upsilon_F \approx 1\times10^6$ m/s. At T=0, for a wide and short strip of graphene coupled to

superconducting electrodes, the values of I_c and I_cR_n are predicted to be:

$$I_c = 1.33\frac{e\Delta W}{\hbar\pi L} \quad \text{and} \quad I_cR_n = 2.08\frac{\Delta}{e}. \tag{3.1a}$$

At the Dirac point they reach asymptotic values when highly doped:

$$I_c = 1.22\frac{e\Delta}{\hbar\pi}k_F W \quad \text{and} \quad I_cR_n = 2.44\frac{\Delta}{e}. \tag{3.1b}$$

In these expressions, W and L are the channel width and length of the graphene, respectively, h is the Planck's constant and k_F is the Fermi wavelength.

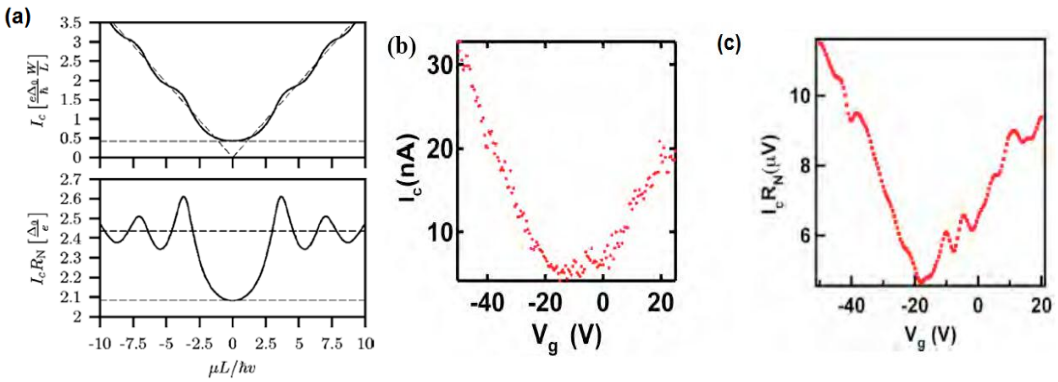

Fig. 3-7 (a) Critical current I_c and Product of I_cR_N of a ballistic Josephson junction, as a function of the Fermi energy μ in the normal region. (b) Critical current I_c vs. gate voltage showing bi-polar supercurrent; (c) Product of I_cR_N as a function of gate voltage for the same device.

Our experimental results shown in Fig. 3.7 (b) and (c) qualitatively agree with them, *e.g.* I_c and I_cR_n attain their minimum values at the Dirac point, and increase with charge density. However, the agreement fails at the quantitative level. Taking W/L=10 and Δ=110 μV extracted from MAR measurements, theory yields I_c~110nA at the Dirac point, where the experimental value is observed to be 6 nA. Another important discrepancy is that the I_cR_n product is predicted to have relatively weak

dependence on gate voltage – it increases by ~20% from half filling to highly doped regimes, in contrast to the experimentally observed increase of 200-300%. Similarly large variations in I_cR_n vs V_g were also reported by other groups [76, 77].

3.4 Premature Switching in RCSJ Model and Suppression of I_c

The discrepancies between theoretical and experimental values of I_cR_n and I_c were tentatively attributed to disorder [83]. Here we explore the roles played by thermal fluctuations in SGS Josephson junctions. The strong depression of I_c is reminiscent of the behavior of premature switching in underdamped junction described in RCSJ model, in which the junction is shunted by a resistance R_j and a capacitance C_j [84]. For SNS junctions, we can take $R_j \sim R_n$. Within this model, the *superconducting phase* across the junction has the mechanical analogue of a particle in a titled washboard potential (Fig. 3.8), with a frictional force (dissipation) that scales with $1/R_n$. Hence, the bias current corresponds to the tilting slope of the "washboard", the superconducting state of the junction corresponds to the particle localized within one of the potential minima, and the resistive state to that rolling continuously down the potential.

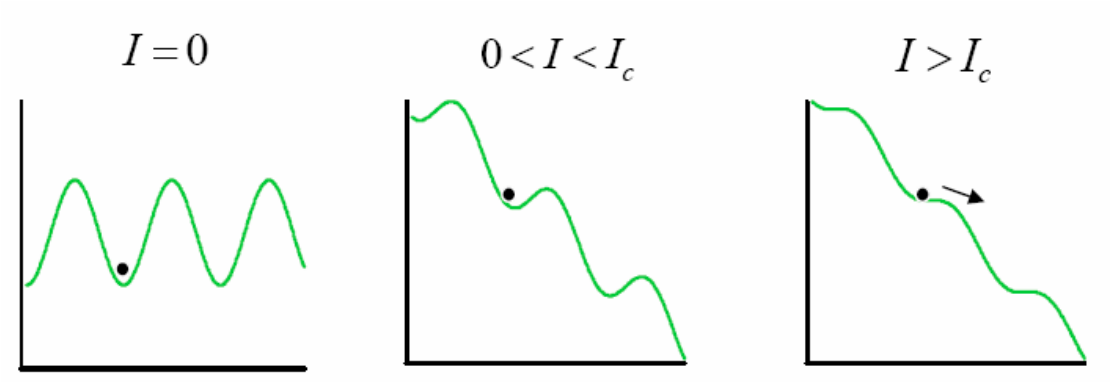

Fig. 3-8 The "tilted washboard" model

The RCSJ model is usually parameterized by the "quality factor" Q, which is defined by:

$$Q = \omega_p R_j C_j,$$

where $\omega_p=(2eI_{c0}/\hbar C)^{1/2}$ is the plasma frequency of the junction and I_{c0} is the intrinsic critical current in the absence of fluctuation. The parameter Q indicates the dissipation experienced by the particle: the junction is *overdamped* if $Q<<1$, and *underdamped* if $Q>1$.

Experimentally, an underdamped junction can be uniquely identified by its hysteretic *V-I* characteristics, that is, the retrapping current I_r (at which the junction switches from the resistive state to the superconducting state) occurs at a lower value than I_c, reflecting the effect of the inertia of a particle moving in a low friction potential. On the other hand, a junction with non-hysteretic *V-I* characteristics may either be overdamped, or under-damped but with weak Josephson coupling or strong thermal fluctuations. Examining our SGS devices, hysteretic *V-I* curves were

observed in the majority of the junctions, indicating that most, if not all, of the devices are underdamped. As shown in Fig. 3.9, we also observe that the hysteretic feature in SGS junctions is gate tunable: the hysteresis becomes much smaller or even vanishes when V_g tunes graphene from highly doped to zero doping regimes.

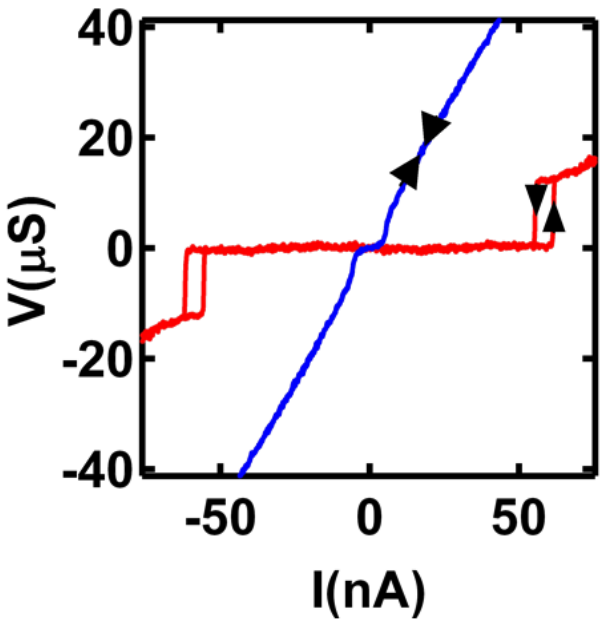

Fig. 3-9 *V-I* curves at different gate voltage showing gate tunable hysteresis observed in SGS junctions

In the presence of thermal and other fluctuations, premature switching is expected to occur in underdamped junctions, as the particle is thermally activated over the energy barrier. Due to the low damping, once an event of "escape" happens, the particle accelerates down the washboard and is never re-trapped. This premature switching is stochastic and induces a distribution in measured values of I_c, the average of which can be much smaller than I_{c0}. The mean value of I_c can be

approximated by the formula [84]:

$$I_c = I_{c0}\{1-[(k_BT/2E_J)\ln(\omega_p\Delta t/2\pi)]^{2/3}\}, \quad (3.2)$$

where k_BT is the thermal energy, $E_J=\hbar I_c/2e$ is the Josephson couple energy and Δt~0.1s is the sweeping time of the biased current through the dense part of the distribution of observed I_c values. Thus I_c will be significantly reduced from its "intrinsic" value I_{c0} at finite temperature, if thermal fluctuation is non-negligible compared with the Josephson coupling energy.

For our devices, ω_p~ 10^{11} – 10^{12} Hz, so the logarithmic term yields ~ 21-23. At the Dirac point, if we estimate I_c=110nA from Eq. (3.1a), the ratio $k_BT/2E_J$ is ~0.05. This implies that the critical current is almost completely suppressed, and that the junction's *V-I* curves is non-hysteretic due to thermal fluctuations, in agreement with experimental observation. When graphene is highly doped, the ratio $k_BT/2E_J$ decreases proportionally with increasing I_{c0}, indicating the decreasing importance of thermal energy. Thus premature switching can readily account for the much-reduced values of I_c observed in all experiments to date, as well as *V-I* characteristics that are hysteretic at high charge carrier density, and non-hysteretic at the Dirac point.

We now seek to understand the unexpectedly strong dependence of I_cR_n on V_g within the model of premature switching in underdamped Josephson junctions. The gate-dependent R_n, which sets SGS apart from other JJs, plays a vital role here: changing gate voltage can effectively tune I_{c0} and all other parameters that depend on I_{c0}, including E_J, ω_p, and Q. Thus, as V_g increases from the Dirac point, R_n decreases,

leading to a smaller $k_BT/2E_J$ ratio and a less-suppressed I_c. Such relative increase in I_c is more than compensates of the decrease in R_n, resulting in a larger I_cR_n product.

Quantitatively, we assume $I_{c0}R_n$=constant from Eq. (3.1) and calculate I_{c0} using measured values of $R_n(V_g)$; then the values of $I_c(V_g)$ in the presence of thermal fluctuation are readily calculated using Eq. (3. 2) and multiplied by R_n. The resulting $I_cR_n(V_g)$ are normalized to the value at the Dirac point (hence the exact value of the constant is inconsequential), and shown in Fig. 3.10 (a). For comparison, normalized data are shown in Fig. 3.10 (b). In the simulation, between the Dirac point and the highly doped regimes, I_cR_n varies by a factor of ~3-3.5, in reasonable agreement with the factor of 2.2-2.8 observed in the data.

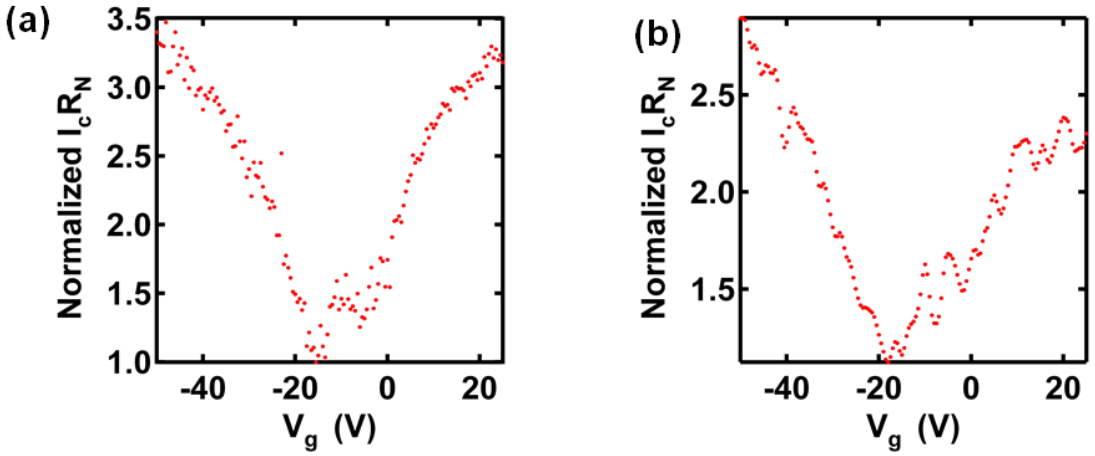

Fig. 3-10 (a) Calculated and (b) experimental curves of normalized I_cR_n vs. V_g, where I_cR_n is normalized to the value at the Dirac point.

We also note that our simple simulation assumes I_cR_n=constant, and does not

take into account the 20% variation predicted by Eq. (3.1). This can partially explain the larger variation in I_cR_n in the simulation. Moreover, although our calculation is motivated by theoretical predictions for transport in the ballistic regime, both the RCSJ model and the assumption of a constant, "intrinsic" I_cR_n product are quite general; hence our results should have wide applicability.

Finally, the gate dependence of the junction's resistance leads to similar tunable behavior in its quality factor Q or dissipation. This is similar to the gate-tunable dissipation observed in carbon nanotube JJ [67, 85]. Because of its relatively large range of tunable R_n, graphene can be used to provide a tunable shunt resistor in other JJ for study of dissipation and quantum coherence [86].

In summary, our observation of depression of critical current I_c and the strong dependence of I_cR_n on charge density of SGS junctions can be satisfactorily accounted for by premature switching in underdamped Josephson junctions.

3.5 Seeking for superconductivity in suspended graphene

The key to observation of specular Andreev reflection in graphene is high mobility and sharp, well-defined Dirac points. Thus, we attempted to produce suspended-graphene Josephson transistors using lithography-free and ultranarrow-separation shadow mask technique (Fig. 3.11). Though preliminary results showed signatures of proximity-induced supercurrent, it is difficult to get devices with both high mobility and large I_c at the same time.

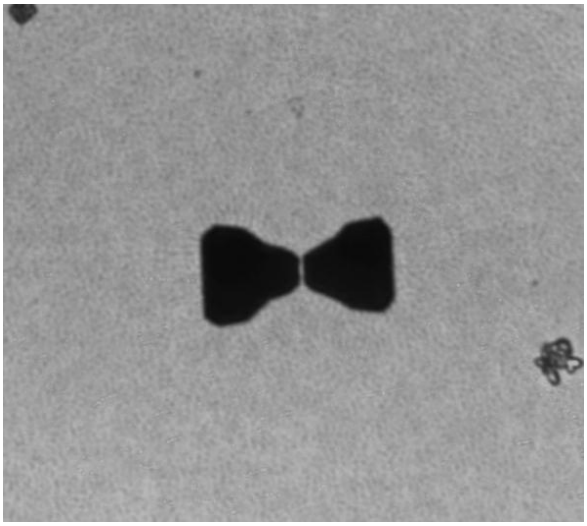

Fig. 3-11 Si shadow mask with 100-nm separation between two electrodes.

Chapter 4. Quantum Hall effect in graphene

The integer quantum Hall effect (IQHE) is a prototypical quantum phenomena arising in 2DES. The key experimental signature is that, under a strong magnetic field, the Hall conductivity σ_{xy} of 2DES is quantized in integer numbers of e^2/h, while the longitudinal resistivity vanishes. Furthermore, similar experiments on 2DES with higher mobility and/or in higher magnetic fields reveal a fractional quantum Hall effect (FQHE) [87], where quantization of the Hall conductivity quantized at fractional values of e^2/h. Although transport behaviors in FQHE and IQHE are quite similar, the underlying physical mechanisms are completely different. While the IQHE is essentially due to single-particle localization, the FQHE is due to many-body effects of strongly correlated electron liquids, with the quantization of the σ_{xy} resulting from localization of collective electronic excitations [87]

In this chapter we will start with a brief introduction of QHE in graphene and followed by discussion of our experimental observation of IQHE and FQHE in both bilayer (section 4.2) and trilayer graphene (section 4.3). In section 4.3.2 we will also report a split of QH plateaus in rhombohedral-stacked trilayer graphene (r-TLG). Such splitting is a signature of Lifshitz transition, a topological change in the Fermi surface, which could be found BLG or r-TLG.

4.1 Introduction to QHE in graphene

4.1.1 Integer QHE in single layer and bilayer graphene

Fig 3.12 illustrates the first experimentally measured transport data of single layer graphene (SLG) from A. Geim's group [1] at 14T. The Hall conductivity exhibits a set of quantized plateaus situated symmetrically with respect to the Dirac point, with quantized values 2, 6, 10, 14….[1, 2]:

$$\sigma_{xy} = 4\times(N+\frac{1}{2})\frac{e^2}{h},$$

and the energy of massless relativistic fermions in quantized fields

$$E_N = \mathrm{sgn}(N)\sqrt{2\hbar e v_F{}^2 B|N|},$$

where v_F is Fermi velocity. The factor of 4 in the conductivity expression is due to the double *spin* and double *valley* degeneracies. Notably, this expression differs from that in standard 2DES by the extra ½ constant in the parentheses; as a result, there is no plateaus at E=0, and the first quantized plateau occurs at $2e^2/h$ in the electron-doped regime and $-2e^2/h$ in the hole doped regime. Thus this is often referred to as the anomalous "half-integer" QHE. The behavior of the longitudinal resistivity ρ_{xx} is largely similar to that observed in GaAs and Si based systems, except that at E=0 it has a berry phase β=1/2. The Berry's phase also arises due to the zero effective carrier mass near the Dirac points in SLG. On the other hand, studies of the temperature dependence of the Shubnikov-de Haas oscillations in SLG reveal that the carriers have a non-zero cyclotron mass [1], despite their zero

effective mass from the *E-k* relation.

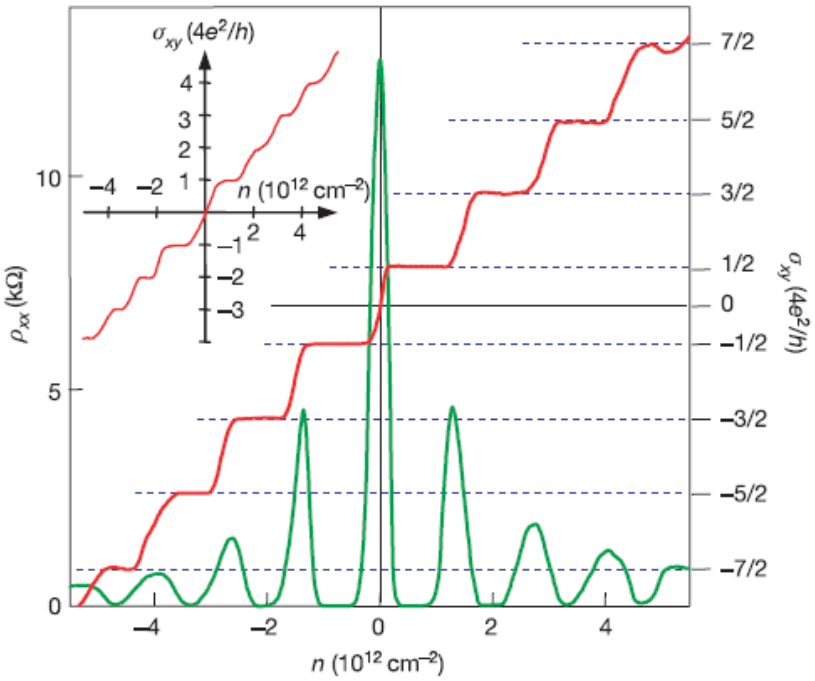

Fig. 4-1 Integer quantum Hall effect in single layer graphene. The inset shows IQHE of bilayer graphene [1].

The observed half-integer QHE is due to the linear dispersion relation in SLG. A different example is that in BLG, which has parabolic bands touching at zero energy, exhibits a different integer QHE at sufficiently high magnetic fields:

$$\sigma_{xy} = 4 \times N \frac{e^2}{h},$$

where N=-3, -2, -1, 1, 2, 3…and experimental results are shown in the inset of Fig. 4.1. This is similar to the behavior in other conventional 2-DEG materials, except that there is no $N=0$ state. So the step between the two lowest quantum Hall plateaus is 8 e^2/h, arising from BLG's 8-fold (spin, valley and orbital) degeneracy at zero energy.

In magnetic fields the LL (see section 1.5 for definition) energies of BLG are:

$$E_N = \pm \frac{\hbar eB}{m^*} \sqrt{N(N-1)},$$

where m^*~0.02 -- 0.04m_e is the effective mass of charge carriers in BLG and m_e is electron's rest mass. Therefore the *QHE signature provides a tool to distinguish SLG and BLG*.

Unlike normal metals, the longitudinal resistivity of SLG shows maxima rather than minima for integral values of the Landau filling factor in measurements of the Shubnikov-de Haas oscillations, which show a Berry's phase shift of π, known as Berry's phase [2], which has already been discussed in chapter 1.6.3.

4.1.2 Spin and valley split QHE states in SLG and BLG

In sufficiently high magnetic field and/or high mobility samples, new quantized plateaus can appear [88] [89]. This is illustrated in Fig.4.2, which show evolution of the Hall conductivity σ_{xy} as B increases from 9T to 45T. At B<15T the quantized values are still given by the half-integer sequence 2, 6, 10…, and at higher fields

$$\sigma_{xy} = 0, \pm 1, \pm 4 \frac{e^2}{h}$$

start to develop. This is illustrated in the lower left inset in Fig. 4.2, indicating the lifting of the valley and spin degeneracy of the n=0 LL, and the lifting of valley or spin degeneracy of $n = \pm 1$LLs.

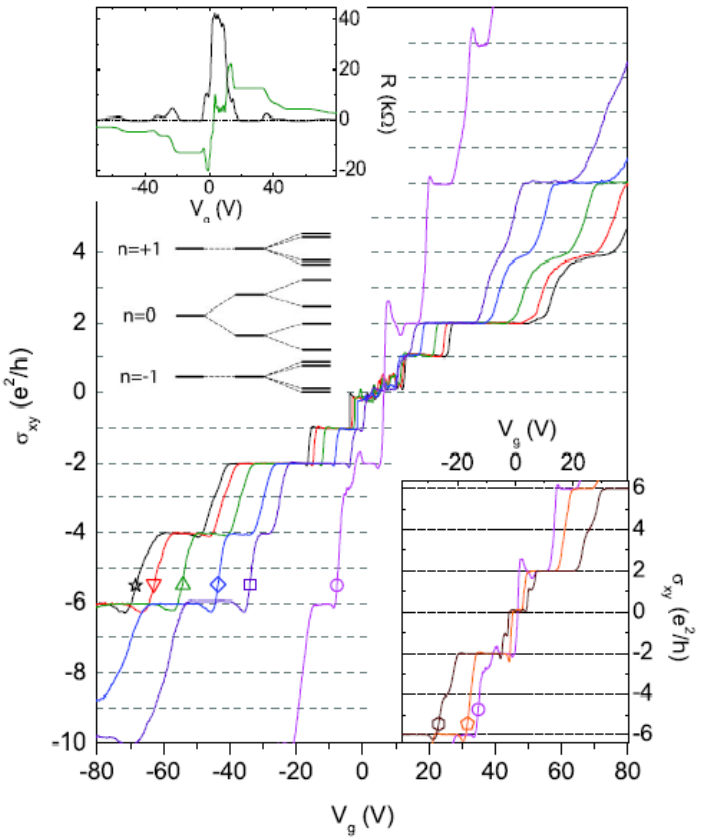

Fig. 4-2 σ_{xy} as a function of V_g at different magnetic fields: 9 T (circle), 25 T (square), 30 T (diamond), 37 T (up triangle), 42 T (down triangle), and 45 T (star). Left upper inset: Longitudinal and Hall resistivity for the same device measured at B =25 T. Left lower inset: a schematic drawing of the LLs in low (left) and high (right) magnetic field. Right inset: detailed Hall conductivity data near the Dirac point for B = 9 T (circle), 11.5 T (pentagon), and 17.5 T (hexagon) [88].

The longitudinal resistivity ρ_{xx} at $\nu=\pm1,\pm4$ plateaus vanishes, similarly to the conventional QHE, however the $\nu=0$ state is rather special, despite exhibiting a clear plateau in σ_{xy} the longitudinal resistivity ρ_{xx} does not vanish, but monotonically increases as function of magnetic field at B>10T [88]. Origin of this insulating ν=0 state is controversial [89]

At $\nu=\pm1,\pm4$, ρ_{xx} also exhibits activated temperature dependence [90], from

which gaps between split LLs can be extracted. The gaps at $\nu = \pm 1$ have a square root *B* dependence [90], and are much larger than the bare Zeeman splitting, thus indicating the interacting nature of these split QH states. Furthermore the sensitivity of the gaps at $\nu = \pm 4$ to the in-plane magnetic field suggests that they are spin split rather than valley split.

In bilayer graphene, besides spin and valley degeneracy, *layer* can provide another degree of freedom for each electron, the lowest LL at zero energy has eight-fold degeneracy. All degeneracies of the lowest LL can be completely lifted by many-body interactions in high magnetic field [91-93] as shown in Fig. 4.3. Like SG, the ν=0 state is also insulating, and as we show in Chapter 5, is related to the ground state of BLG at the charge neutrality point.

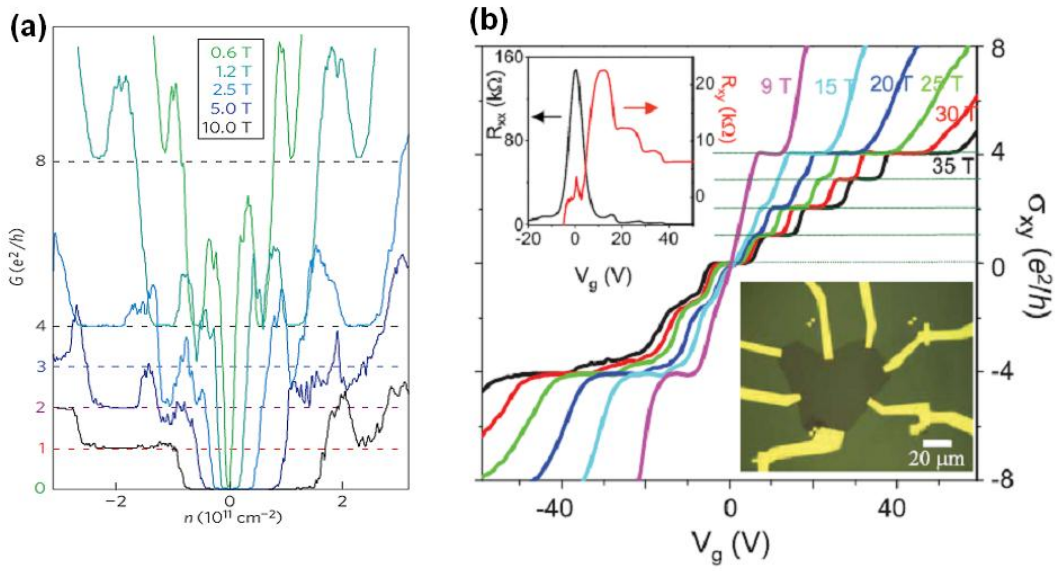

Fig. 4-3 Symmetry breaking in (a) suspended bilayer graphene and (b) substrate supported bilayer graphene at ultra-high field. The 8-fold degeneracy is lifed for the lowest LL level.

4.1.3 Fraction QHE in single layer graphene

FQHE is due to many-body effects of strongly correlated electron liquids, it can be understood as the realization of the integer QHE for weakly interacting quasiparticles called composite fermions, which could be described as an even number of magnetic flux vortices interact with an electron to form a particle with reduced effective charge that is a fraction of *e*.

In graphene, FQHE was first observed in suspended single layer graphene (Fig. 4.4(a) and (b)) [94, 95]. A recent measurement from a h-BN supported graphene (Fig. 4.4(c)) with Hall-bar geometry showed filling factors appear in the following sequence [96]:

$$\pm\frac{1}{3},\pm\frac{2}{3},\pm 1,\pm\frac{4}{3},\pm 2,\pm\frac{7}{3},\pm\frac{8}{3},3,\pm\frac{10}{3},\pm\frac{11}{3},4,\pm\frac{13}{3}....$$

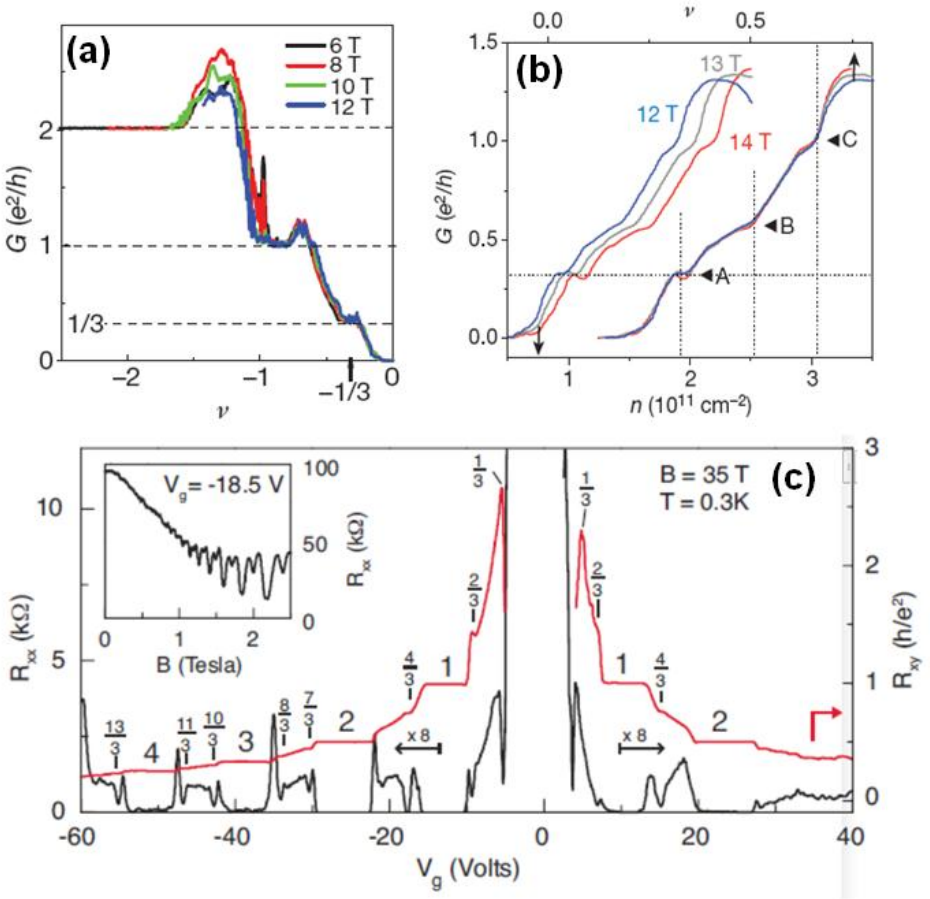

Fig. 4-4 (a) and (b) FQHE in suspended graphene. (c) h-BN supported graphene exhibits multiple plateaus at fatrational filling factors [96].

4.2 Symmetry Breaking and Evidence for Fractional Quantum Hall States in Suspended BLG

4.2.1 Device fabrication and chracterization

The graphene devices are fabricated by "scratching exfoliating" of Kish graphite over pre-defined trenches on degenerately doped Si/SiO_2 substrates. BLG sheets are identified by color contrast in an optical microscope and/or Raman spectroscopy. The trenches are 250 ± 50 nm deep, with typical areas ~10-100 μm^2 (Fig. 4.5). Since the graphene sheets do not undergo any chemical processing, they are exceedingly clean.

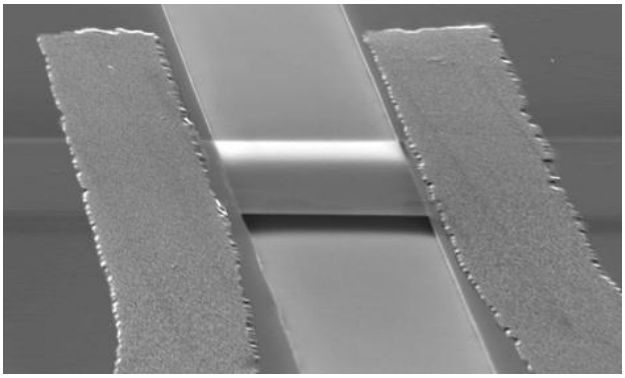

Fig. 4-5 SEM image of a suspended BLG device.

The devices are measured at low temperatures using standard lock-in techniques. The blue curve of Fig. 4.6 displays the two terminal conductance *G vs.* gate voltage V_g, for an as-fabricated BLG device at 4.2 K; BLG's Drude mobilities

are typically ~10,000-30,000 cm^2/Vs, where σ is the two terminal device conductivity and e is the electron charge. After current annealing, which is

performed at a current density of ~ 0.1 – 0.2 mA/μm/layer, the $G(V_g)$ characteristics displays much sharper Dirac points that are closer to zero (red curves, Fig. 4.6). For a typical post-annealed BLG device, Drude mobilities μ_D ranges from 100,000 to 274,000 cm^2/Vs at n~10^{10} cm^2, while their field effect mobility $\mu_{FE} = \frac{1}{e}\frac{d\sigma}{dn}$ ranges from 28,000 to 200,000. These values are exceedingly high, especially considering that the mobility of a BLG device is typically an order of magnitude lower than that of SLG. Thus, both the mobility values and the device areas of our devices are significantly larger than those previously reported.

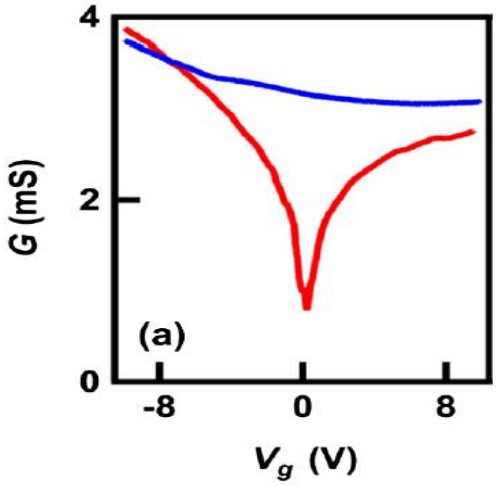

Fig. 4-6 $G(V_g)$ for a BLG device at T=4.2K. The blue and red curves are taken before and after current annealing, respectively.

4.2.2 SdH oscillation and integer QH features

We now examine the conductance of a bilayer device BL1 in finite B at T=300mK (similar data were observed on 2 other samples). As shown by Fig. 4.7(a),

which plots *G vs. 1/B* at 10 different gate voltages, *G* displays pronounced SdH oscillations, which are discernible at *B* as low as 0.2 T.

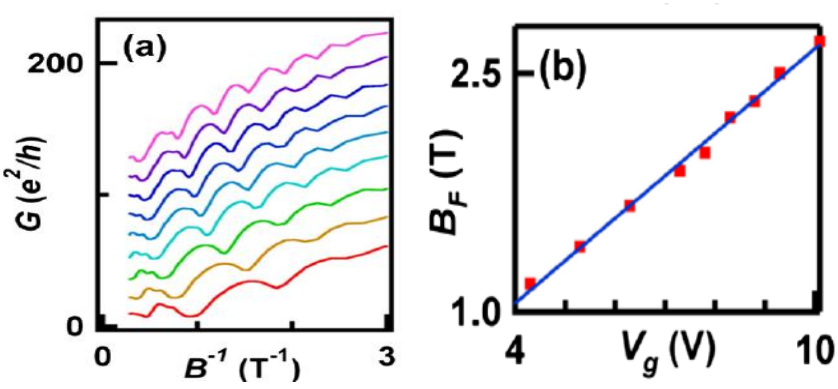

Fig. 4-7 Data from a bilayer device BL1 at 300mK. (a). *G vs.* 1/*B* at V_g=3, 4, 5, 6,7, 7.5, 8, 8.5, 9 and 9.8V (bottom to top). The traces are offset for clarity. (b). B_F *vs.* V_g. The straight line is a linear fit to the data points.

The exceedingly high mobility of the devices, together with the low field at which SdH oscillations become visible, underscore the high quality of our devices. Yet, the device conductance is not properly quantized, even at the highest attainable magnetic field. This absence of quantization is not fully understood, but could be attributed to 3 factors: Firstly, the devices' two-terminal geometry leads to conductance comprising of both longitudinal and transverse contributions [97]. The non-square geometry of the device then gives rise to non-monotonous dependence of *G* on *n*, and, for sufficiently broadened LLs, non-quantized conductance. Another possible reason is the presence of strain and/or ripples in our devices [52], which are up to 5 μm long and rests on the rigid banks of the trenches. Their deflection under

applied V_g, which scales with the 4/3 power of the length, could produce significant strain close to their rigid boundaries, which in turn result in gauge fields [49] that partially destroy the conductance quantization [98, 99]. A third possible factor is the small substrate-supported area of the device (typically <10% of the total device area), which presumably has lower mobility and may not exhibit QHE at low B, thus destroying the overall conductance quantization.

Despite the lack of conductance quantization, it is still possible to extract information on QH states from the data. For this device that is short and wide, filling factors ν of the conductance minima can be used to identify QH features [97]. To this end, we note that $B_F = nh/4e = (\alpha V_g)h/4e$, where $1/B_F$ is the period of the SdH oscillations, and $\alpha = n/V_g$ is the coupling efficiency of the back gate (here V_g is measured from the Dirac point). Plotting the measured values of B_F *vs.* V_g indeed yields a straight line, with a best-fitted slope of a=0.26 T/V (Fig. 4.7b). This indicates $\alpha = a(4e/h) \approx 2.5 \times 10^{10}$ cm^{-2} V^{-1}, in agreement with that independently estimated from the device geometry. We can thus *unequivocally* determine the filling factor corresponding to any given data point:

$$\nu = nh/Be = 4a(V_g/B) \approx 1.05(V_g/B). \quad (3.3)$$

To examine the data more closely, we plot several $G(V_g)$ traces at different values of B (Fig. 4.8). The conductance exhibits pronounced oscillations, with the minima occurring at V_g that correspond to integer ν, as calculated using Eq. (3.3). The filling factor of each minimum is labeled.

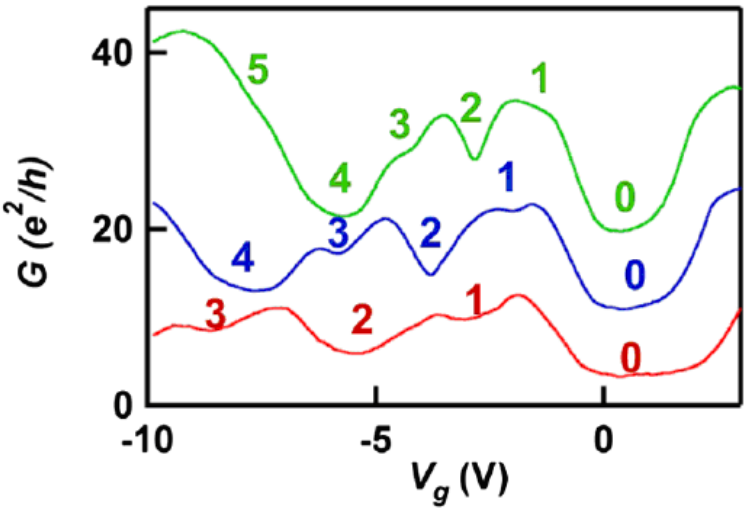

Fig. 4-8 $G(V_g)$ at B=3, 2 and 1.5T (bottom to top). For clarity, the upper two curves are offset by 7 and 15 e^2/h, respectively. The numbers indicate the $|\nu|$ values that correspond to the local conductance minima.

For instance, clear conductance minima for $-4 \leqslant \nu \leqslant 0$ are visible at B=2T, and resolved successively in the order ν=-4, 0, -2, -3, -1. This is reminiscent of the data reported in ref. [91, 92], in which the ν=0 QH plateau appears at the lowest field, followed by the plateaus ν=2, 3 and 1. Hence, the observations of conductance minima at integer filling factors, and their resolution in the same order as in previous reports, suggest that these minima arise from integer QH effect in BLG, with the orbital, spin and valley degeneracies lifted.

To demonstrate scaling of the integer QH features with magnetic field B, we take line traces $G(V_g)$ at different magnetic fields (Fig. 4.9 left panel). These traces are then replotted as a function of filling factor ν, which is calculated using Eq. 3.3. As shown by the right panel in Fig. 4.9, the curves are nicely ordered, with the

conductance minimum occurring at $\nu \approx 0$, -1, -2, and -3, respectively, suggesting that they indeed arise from the spin- and valley- resolved QH states.

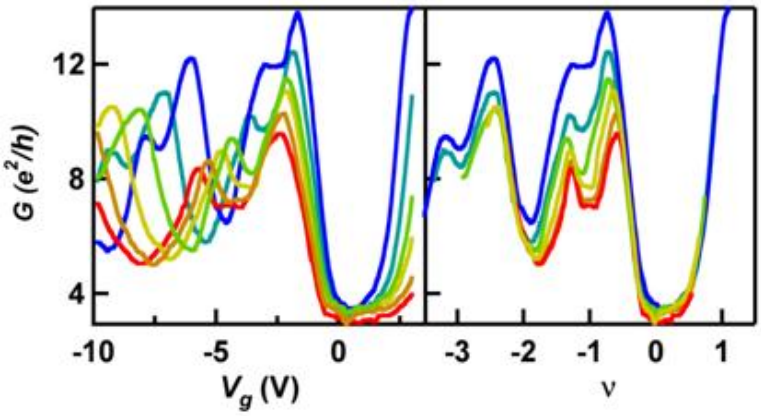

Fig. 4-9 $G(V_g)$ and $G(\nu)$ taken at B=2.5, 3, 3.5, 4, 4.5, and 5T.

We also plot the evolution of G in units of e^2/h (upper panel) and dG/dV_g (lower panel) as functions of B and V_g (Fig. 4.10). The bands of colors that radiate from V_g~ 0.3V, which is inferred to be the Dirac point, mark the onset of SdH oscillations. The MC can be seen more clearly by differentiating G with respect to V_g, where the blue (red) regions indicate negative (positive) values of dG/dV_g; the local conductance minima appear as white regions in the V_g-B plane, as outlined by the dotted lines.

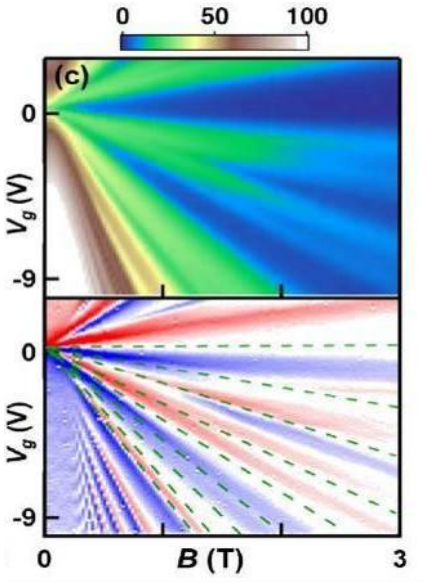

Fig. 4-10 (upper) and dG/dV_g (lower panel) vs B and V_g. The dotted lines correspond to features with integer ν between ν=0 and -8.

Strikingly, from their slopes in the V_g-B plane and Eq. (3.3), the filling factors of these minima are identified to span all integers between 0 and -8 when the device is hole-doped (albeit the ν=-5 and -6 minima are just barely distinguishable); for the electron doped regime, because of the limited V_g range, only minima with ν=2 and 4 are identified. Such persistence of these conductance dips at integer values of ν, which are observed for *all* accessible values of V_g and B, provides very strong evidence that they indeed arise from orbital-, spin- and valley-resolved QH states. We note that this is the first report of possible symmetry breaking for the N=2 LL, which is expected to exhibit interaction effects. For instance, we observe that the ν=7 state is resolved before the ν=5, 6 states, suggesting a larger energy gap for the former. This is quite surprising, since the even integer states are expected to be resolved first. Further investigation would be necessary to provide further insight

into these symmetry-broken higher LL states in BLG devices.

4.2.3 FQH features in higher magnetic field

We now focus on the BLG device behavior in higher fields 4<*B*<31T. To avoid collapsing of the atomic membranes, we restrict the applied $|V_g|$ to <10V; thus, for B>10T only QH state with $|\nu|$ <1 are experimentally accessible. In the $G(V_g, B)$ plot (Fig. 4.10a), a white/pink feature with a shallow slope is discernible. Its slope in the V_g-B plane is V_g/B~0.32, yielding $\nu \approx 0.33$. This feature can be seen more clearly by taking discrete line traces at different B values (Fig. 4.11b) – it appears as a broadened peak for B<15T, but develops into a small plateau with increasing B. Fig. 4.11c replots these traces as $G(\nu)$, where ν is calculated using Eq. (3.3) with the small offset in Dirac point taken into account. As expected, for B>15T, the traces nearly collapse into one, with the small plateau located at ν=0.33.

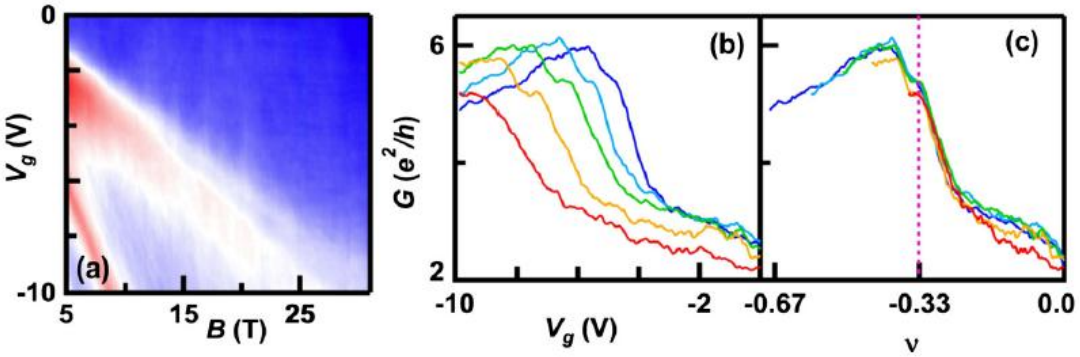

Fig. 4-11 High field data for BL1. (a). $G(V_g, B)$ at 300 mK. (b-c). Line traces from (a) at B=15T, 17.5T, 20T, 23T and 28.5T (right to left in (b)), plotting against V_g and ν, respectively.

Taken together, this provides strong evidence that we have observed the

fractional ν=1/3 QHE state in BLG. In previous works on SLG, the ν=1/3 fractional state is surprisingly robust and persists up to 20K at B=12T, with a large, Coulomb interaction-induced energy gap $\Delta_{1/3}^{SL} \sim 10\ \mathrm{K} \cdot \sqrt{\mathrm{B}}$ [94, 100]. In contrast, there is little theoretical effort on fractional QHE in BLG [101] [102] [103, 104]. Taking the features in our data as an evidence for the 1/3 FQH state in bilayer, we can obtain an order-of-magnitude estimate for $\Delta_{1/3}^{BL}$ by measuring $G(V_g)$ at several different temperatures T (Fig. 4.12).

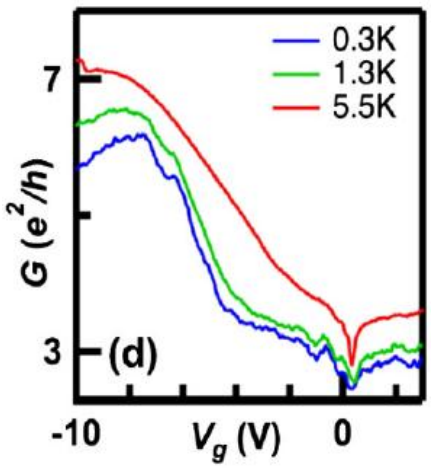

Fig. 4-12 $G(V_g)$ at B=20T and different T. The traces have *not* offset.

At B=20T, the small 1/3 plateau persists at T=1.3K, but disappears completely at T=5.5K, yielding an estimated $\Delta_{1/3}^{BL} \sim 0.4\ \mathrm{K} \cdot \sqrt{\mathrm{B}}$, which is much smaller than that of SLG. The increase in the overall conductance with T also suggests the presence of significant thermally activated conduction through the bulk of the device.

During the last year of my Ph.D. study I improved my device fabrication technique by 1) using better designed aligning windows for shadow mask-graphene

alignment. 2) using Ti instead of Au for contact electrodes since Ti is less mobile on surface of suspended graphene. 3) using well-defined electrodes design to get completely suspended graphene devices. Therefore experimental results show more quantized quantum Hall plateaus in two-probe measurement as shown in Fig. 4.13. In a relative low magnetic field *B*, both devices display QH plateaus with the 8-fold degeneracy of the zero energy Landau level (LL) fully lifted.

A close inspection of Fig. 4.13 (b) and (d) reveals that FQH features are also possibly observed in these devices (black arrows). Comparing with the previous discussed results, the FQH features observed in this work require much lower magnetic fields, indicating an improved sample quality of these devices.

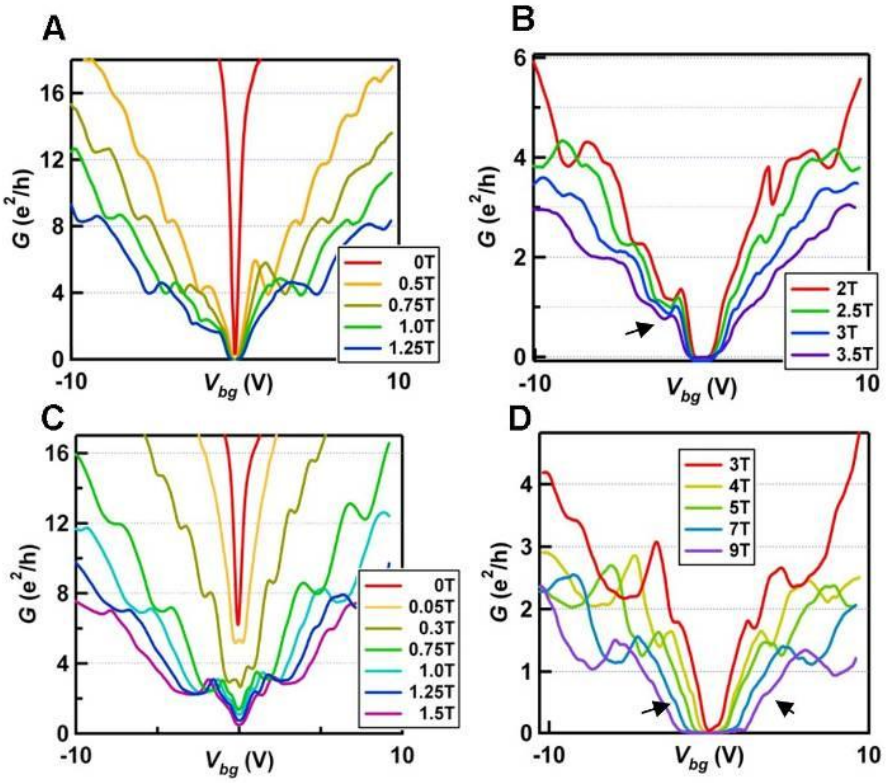

Fig. 4-13 $G(V_{bg})$ taken at different magnetic fields from two BLG devices.

4.3 Quantum Hall effect in Trilayer graphene

4.3.1 Integer and fractional QH features in r-TLG

The exfoliation and fabrication of TLG graphene devices are the same as those for BLG. From tight-binding calculations that include only nearest-layer coupling, the Landau level (LL) spectrum for B-TLG (ABA stacking) is a superposition of those for SLG and BLG [41, 105, 106]:

$$E_{1,N}^{ABA} = \pm\sqrt{2\hbar v_F^2 eB|N|} \quad \text{and} \quad E_{2,N}^{ABA} = \pm\frac{\hbar v_F^{\,2} eB}{t_\perp}\sqrt{N(N-1)}\,.$$

For r-TLG (ABC stacking), the LL energies are given by:

$$E_N^{ABC} = \pm\frac{\left(2\hbar v_F^{\,2} eB\right)^{3/2}}{t_\perp^{\,2}}\sqrt{N(N-1)(N-2)}\,.$$

In these expressions, N is an integer denoting the LL index, v_F~10^6 m/s is the Fermi velocity, e is the electron charge, h is Planck's constant and ~0.2-0.4 eV is the nearest-layer coupling energy. For both types of stacking order, the LL at zero energy is 12-fold degenerate, giving rise to quantized conductance plateaus with integer values ...-10, -6, 6, 10, 14... of e^2/h. When other interlayer and intralayer hopping terms are included, certain degeneracies could be broken [107, 108], though the LL are expected to retain 4-fold degeneracy for B-TLG and 2-fold degeneracy for r-TLG.

Our experimental measurements on a TLG device with μ_{FE} ~μ_D ~50,000 cm^2/Vs at 260mK reveal pronounced MC oscillations. Using the slopes of the conductance features in the V_g-B plane, we identify QH features at ν=0, 11±1, -4, -2, -3 and -1,

which are resolved in the order listed. We note that, albeit without proper quantization, these features' conductances are within ~30% of the expected values. Fig. 4.14(a) displays $G(V_g, B)$ for $2 \le B \le 8$T for such a device TL1. At Dirac point V_g~0.6V, G<5nS, suggesting the presence of an insulating state at $\nu = 0$. Line traces $G(V_g)$ at different B values are shown in Fig. 4.14(b) and Fig. 4.15(a).

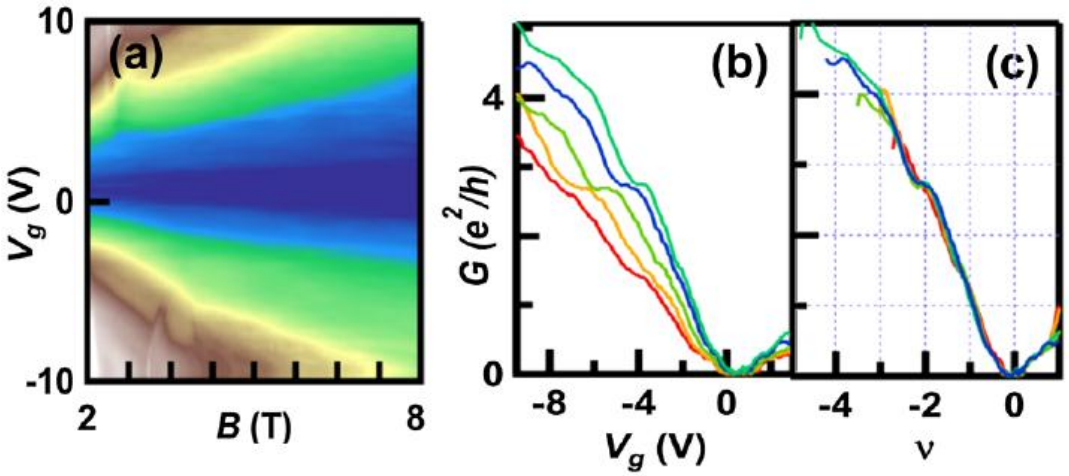

Fig. 4-14 (a). $G(V_g, B)$ at 260mK. (b-c). $G(V_g)$ and $G(\nu)$ at B=2.2, 2.5, 3.0, 3.5, 3.8T.

By plotting the same data as $G(\nu)$, these traces collapse into a single curve (Fig. 4.14c, and Fig. 4.15b), with plateaus or shoulders at integer ν. In particular, Fig. 4.15(b) exhibits two identifiable features: "A" that appears at $\nu = -1.0 \pm 0.03$, and "B" at $\nu = 0.50 \pm 0.07$. Both features are relatively robust in temperature and persist up to 4.5K (Fig. 4.15c).

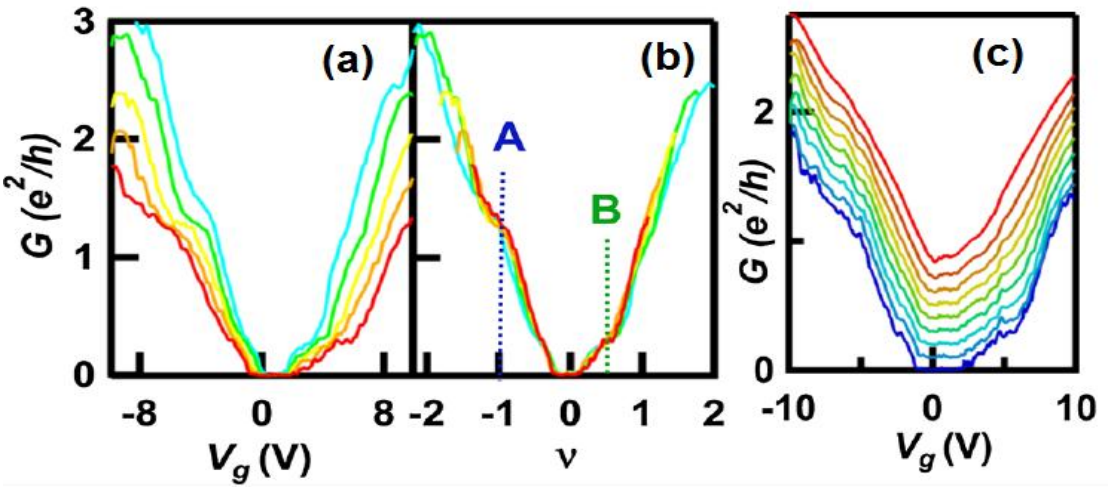

Fig. 4-15 (a) and (b) $G(V_g)$ and $G(\ \ )$ at B=4, 5, 6,7 and 8T. **(c).** $G(V_g)$ at B=8T and T=4.5, 2.7, 1.9, 1.6, 1.3, 1.0, 0.7, 0.4 and 0.26 K(top to bottom). The traces are offset for clarity.

Feature "B" is particularly intriguing, since it may correspond to the ν =1/2 or 2/5 state. A similar feature in SLG has been observed [95], yet its origin is still under debate, since the ν=1/2 feature in R_{xx} in traditional GaAs devices arises from a Fermi liquid state, not FQHE [109]. However, we note that a ν=1/2 FQH state is observed in *bilayer* GaAs devices [110]; thus, though not conclusive, feature "B" may in fact indicate a FQH state in TLG with a relatively large energy gap. The absence of the ν =1/3 state may be attributed to the presence of the ν=0 insulating state, which, if sufficiently wide, is shown to mask signatures of FQH states in suspended single layer devices [94].

4.3.2 Evidence of Lifshitz transition in r-TLG

Fig. 4.16(a) plots the differentiated conductance $dG/dB\ (B, V_g)$ of an **r-TLG** device, which allows the oscillations to be clearly discerned. The QH states appear

as features radiating outward from the CNP at B=0. Since the device has a large aspect ratio (length/width ~3), we use conductance peaks to identify the filling factors of the QH plateaus [97], which are determined from their slopes in the V_g-B plane: $\nu = nh/Be = \alpha V_g h/Be$, where α is estimated to be $2.5\text{x}10^{10}$ $\text{cm}^{-2}\text{V}^{-1}$ from geometrical consideration as well as the periods of SdH oscillations [93]. This is the same as what we discussed in the previous chapter about BLG devices since both type of devices underwent same fabrication process.

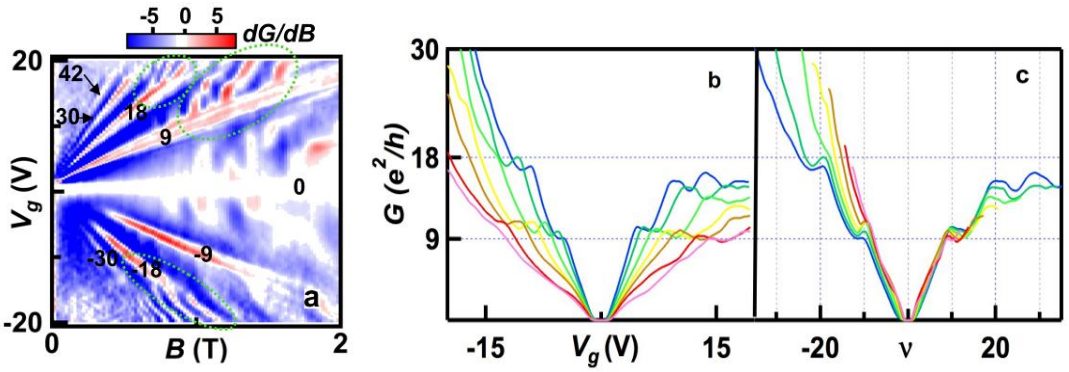

Fig. 4-16 (a) $dG/dB(V_g, B)$. The numbers indicate the filling factors of the features. (b) and (c): $G(V_g)$ and $G(\nu)$ at T=1.5 K and B=0.5(blue), 0.6(cyan), 0.8(green), 1(yellow), 1.2(orange), 1.5(red), and 1.7 T(magenta). 1.25 k has been subtracted from device resistance to account for the contact resistance and line resistance of the cryostat.

Using this relation, the features in Fig. 4.16a are determined to correspond to ν=-30±1.2, -18±1,-9.3±0.5, 0, 9±0.5, 18±1, 30±1.2 and 42±2, respectively, as indicated on the figure. Fig. 4.16(b) plots the device conductance G in units of e^2/h as functions of V_g taken at different values of B; when plotted against ν, the 7 curves almost collapse into one, with plateaus at ~±9 and -18, respectively (Fig. 4.16(c)).

We note that the conductance values approximately agree with the filling factors.

The emergence of filling factors at 9 and 18 are unexpected. A close examination of Fig. 4.16(b) reveals yet another surprising feature -- some plateaus that appear at low fields unexpectedly disappear at higher values of *B*. For instance, the ν = -18 feature is visible at *B*=0.25T and develops into a well-quantized plateau for 0.5<*B*<0.7T, yet it disappears for *B*>0.8T. Similarly, the ν = -9 state is a well-developed plateau at 0.5T, but vanishes for *B* > 1.5T. Instead, each of the $\nu \sim \pm 9$, ±18 and -30 QH features splits into 3 branches at $V_g \sim$ 13-16V and *B*~ 0.6 – 1.3T. The splittings at $\nu \sim 9$, -18 are indicated by the dotted circles in Fig. 4.16 (a). Such apparent 3-fold degeneracy of QH plateaus is highly surprising, and has not been observed in BLG or B-TLG devices with comparable mobility.

Such splittings are signatures of the Lifshitz transition (LT), a topological change in the Fermi surface as a function of electron doping or other parameters such as strain. For multilayer graphene, it may be induced by trigonal warping [106, 111, 112]: at very low *n*, the Fermi surface in r-TLG breaks up into 3-legged pockets, thus leading to triply degenerate LLs [111] as shown in Fig. 4.17; these LLs should split in higher *B* or *n*, corresponding to the merging of the pockets at the LT.

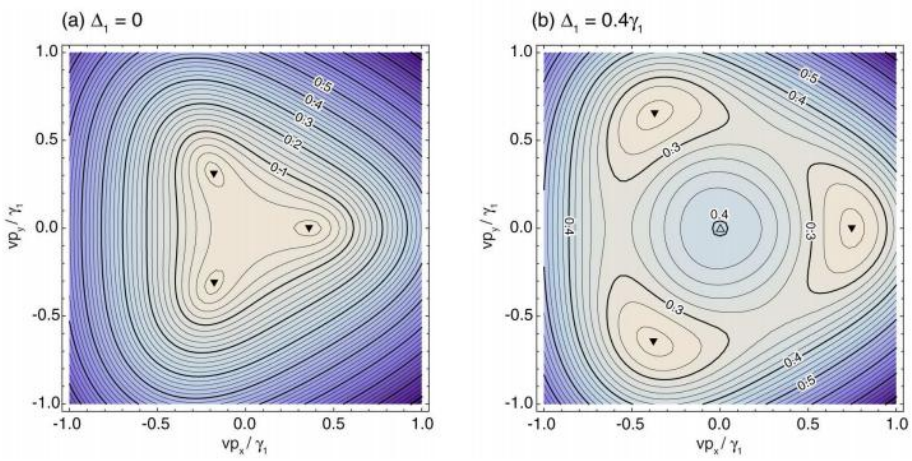

Fig. 4-17 Equi-energy contour plots of the lowest electron band of ABC trilayer graphene, with different values of nearest-layer coupling

Indeed, the observed splittings occur at $|V_g|$~15V and B~1T, within 60% of the theoretically predicted values. The overall device behavior is in semi-quantitative agreement with theoretical simulations of r-TLG's density of states (Fig. 4.18), which is satisfactory, considering that the simulation uses bulk graphite parameter values that are likely different for sheets of atomic thickness.

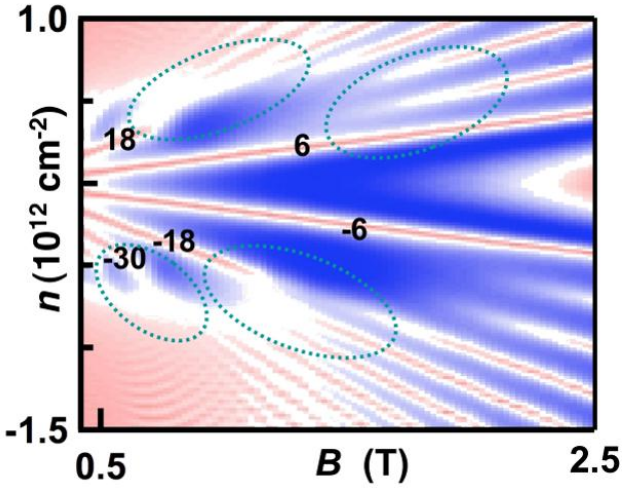

Fig. 4-18 Calculated density of states for r-TLG *vs. B* and *n*.

We note that the biggest discrepancy between the data and simulation lies in the filling factor of the first non-zero plateau. Theoretically, one expects the ν=6 plateau to be the most energetically stable; however, ν~9 was observed instead, suggesting the presence of large valley and spin splitting.

Chapter 5. Insulating state and Phase Transitions in Ultra-clean Bilayer Graphene

In this chapter we will discuss an electronic-interaction driven effect -- the insulating state in charge neutral suspended bilayer graphene devices.

We will start from a systematic study of the minimum conductivity σ_{min} in a large number of single-gated and double-gated BLG samples, with mobilities ranging from 500 to 2000 cm^2/Vs for substrate-supported samples, and 6000 to 350,000 for suspended samples. We find a surprisingly constant σ_{min} value ~ 2-3 e^2/h for the majority of devices, independent of device mobility and the presence or absence of substrates. However, the best devices manifest an insulating state with an energy gap ~ 2-3 meV. This insulating behavior in BLG at the CNP is only observed in devices with both high mobility and low charged impurity density.

We also observe a phase transition between the single-particle metallic state and the interaction-induced insulating state in ultra-clean BLG, which can be tuned by temperature, disorder, charge density n and perpendicular electric field $E_\perp$.

5.1 Introduction

Bilayer graphene (BLG) has provided a fascinating new platform for both post-silicon electronics and exotic many-body physics [40, 56, 113, 114] . Because its conduction and valence bands touch at two points in momentum space and have approximately quadratic dispersion with associated sublattice pseudospin chirality,

charge neutral BLG is likely to have a broken symmetry ground state in the absence of disorder [112, 115-119]. Theoretical work on the character of the ground state in neutral bilayer graphene has argued for a variety of distinct states including gapped anomalous Hall states and layer antiferromagnetic states that break time-reversal symmetry and gapless nematic states which alter Dirac point structure and reduce rotational symmetry. Recent experimental advances [120-124] report low-temperature conductivity σ_{min} values for neutral BLG that vary over a large range, from 0.05 to 250 μS. Because radically different transport characteristics are observed in samples that are apparently quite similar, it has been difficult to draw firm conclusions.

5.2 Device fabrication, current-anneal cleaning and characterization

We fabricate single-gated BLG devices using a lithography-free technique (described in section 2.1.3) and a typical device is shown in Fig. 5.1(a), and suspended double-gated BLG by combining acid etching with a multi-level lithographic technique to make devices with suspended top gates (Fig. 5.1b). These double-gated devices [120, 123] allow independent adjustment of induced charge density n and perpendicular electric field $E_{\perp}$.

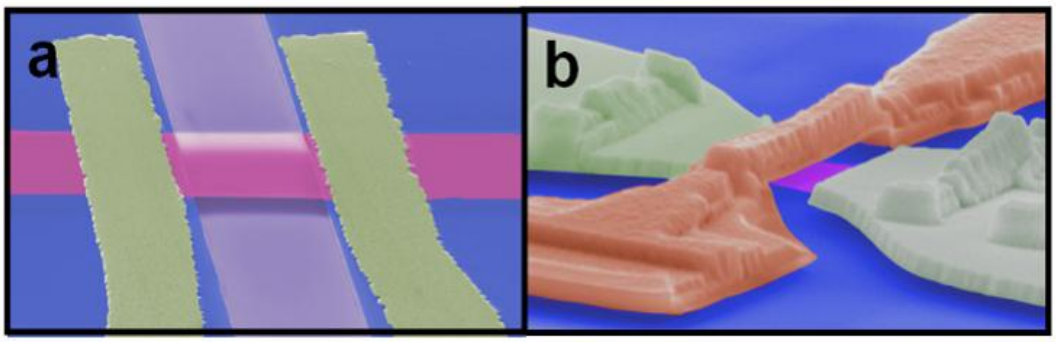

Fig. 5-1 (a) and (b): False-color scanning electron micrograph of BLG device with and without top gate, respectively. Scale Bar: 2um.

After fabrication we transfer our suspended BLG devices into high vacuum cryostat, and current annealing is performed at 1.5K. A typical procedure is shown in Fig. 5.2. We first ramp up the source-drain bias V_{sd} at a rate ~10mV/s, and monitor the current I across the device, while keeping the gate electrode(s) grounded. The I-V curve, which is linear at low bias, becomes sub-linear at larger bias (Fig. 5.2a). At this point V_{sd} is ramped down to zero, and we examine field effect mobility μ and minimum conductivity σ_{min} (inset of Fig. 5.2a). Generally μ significantly increases and σ_{min} decreases. Several cycles of current annealing are performed until current saturation is observed (Fig. 5.2 b-c), and there is no further change in μ or σmin; at this point optimal annealing result is attained. If V_{sd} is increased further, the suspended membrane will start to break due to electromigration, and μ will decrease again.

We also note that the annealing process is typically different for single layer, bilayer and trilayer suspended graphene devices. For instance, current saturation is

not reliably observed in the single layer graphene during annealing process. Such a difference could be attributed to different phonon -electron scattering and capabilities of carrying electrical currents in different layers of graphene.

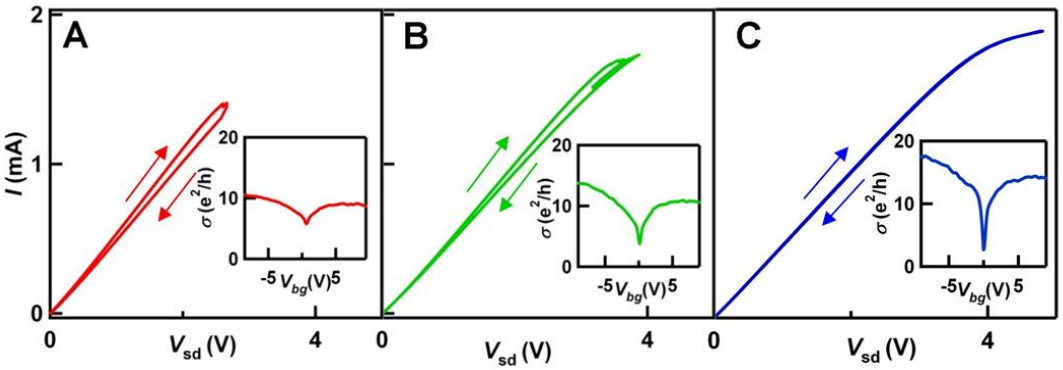

Fig. 5-2 Current annealing cycles displayed as current *I* as a function of source-drain bias V_{sd} in successive sequence (from left to right). Insets: σ (V_{bg}) after eacn current annealing cycle.

Fig. 5.3 displays the two terminal differential conductivity $\sigma=(L/W)dI/dV$ of two suspended BLG devices *vs.* back gate voltage V_{bg} at T=1.5K after current annealing. Here L/W is the aspect ratio of the device. Both curves are steeply *V*-shaped, with CNPs close to V_{bg}=0V. Surprisingly, σ_{min} of the devices are drastically different – 2.5 and 0.02 e^2/h, respectively. The latter insulating behavior is also confirmed by *I*-*V* curves. In a magnetic field *B*, both devices display quantum Hall plateaus with the 8-fold degeneracy of the zero energy Landau level (LL) fully lifted (*24*). From the Landau fan diagram that plots the differential conductance *G* (color) *vs.* V_{bg} and *B* (Fig. 5.3, insets), the ν=0 state is visible for both devices at B>0.5T and persists down to B=0 for the device with very low σ_{min} .

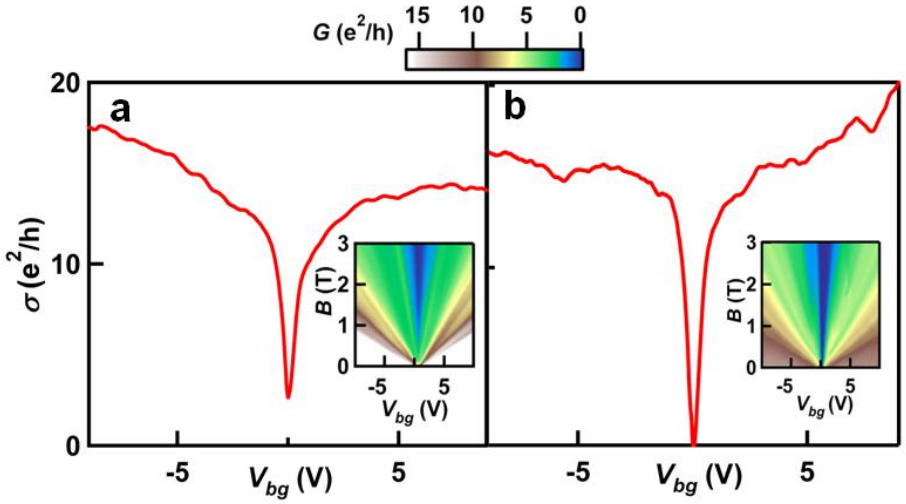

Fig. 5-3 (a) and (b): Main panels and insets: $\sigma\ (V_g)$ and $G(V_{bg}, B)$ for two BLG devices with and without insulating state at CNP (T=1.5K).

Line traces of $G_{min}(B)$ taken at CNP in insets of Fig. 5.3 show that both types of suspended BLG exhibit insulating state at high magnetic field up to 10T; for the suspended BLG that is conductive at B=0, we observe a precipitous transition to an insulating state as B increases to ~1T.

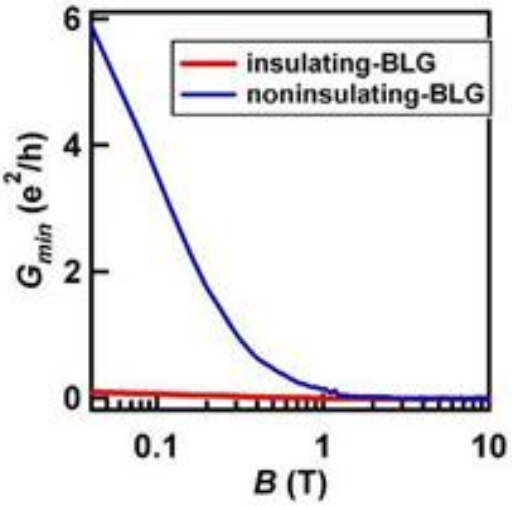

Fig. 5-4 G_{min} as a function of B (in log scale) at CNP for suspended BLG devices shown in Fig. 5.3.

5.3 Minimum conductivity of BLG at Dirac point

With the goal of discovering the origin of the large range of σ_{min}, we investigated 9 substrate- supported BLG devices and 23 suspended BLG devices with aspect ratios between 0.5 and 2, and areas 1-18 μm^2. The results are summarized in Fig. 5.5, which plots σ_{min} as a function of field effect mobility $\mu = \frac{1}{e}\frac{d\sigma}{dn}$ for each device. Evidently, the data points separate into two groups. Most data points fall into group I, in which σ_{min} is almost independent of mobility and similar for suspended and supported devices. Within this class of devices the CNP conductivity ~ 100μS ~*2.8* e^2/h [39, 125-127].

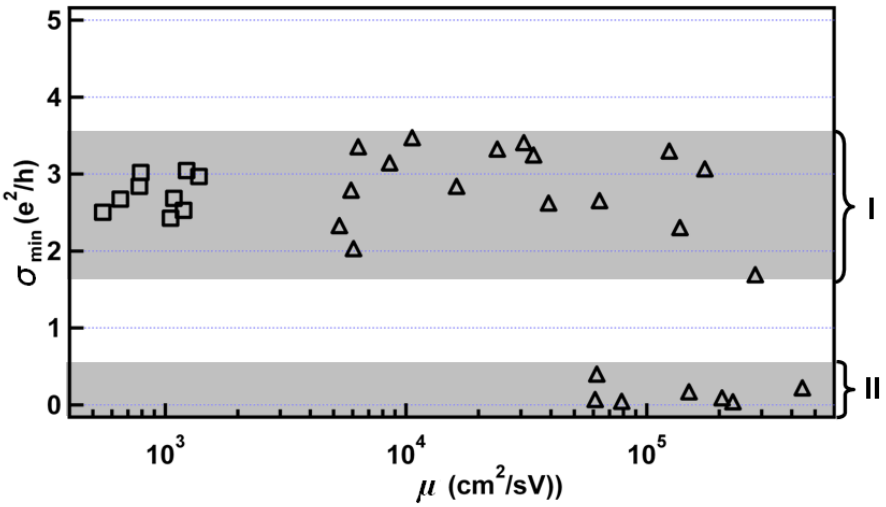

Fig. 5-5 $\sigma_{min}(\mu)$ for 9 substrate supported BLG devices (square symbols) and 23 suspended BLG devices (triangular symbols) at 1.5 K (except for one device in region 2, which was taken at $T=0.3$K)

Very different behavior is found in the 7 devices that fall into group II with very low σ_{min}, which is at most 0.4 e^2/h, and as low as 1 μS. Notably, all 7 devices have very high mobility. To shed further light on the physical difference between the two groups, we also examine V_{CNP}, the devices' applied V_{bg} at the CNP, which indicates the overall doping level. Fig. 5.6(a) and (b) display σ_{min} and μ *vs.* V_{CNP} for all suspended samples with the insulating devices denoted by blue triangles.

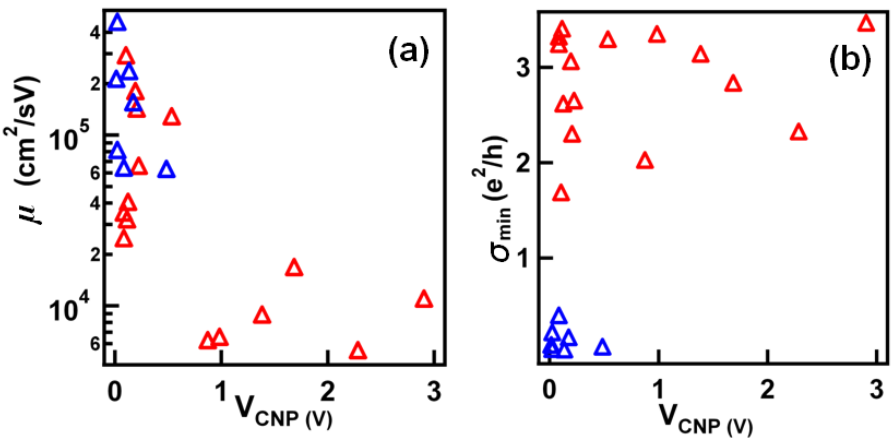

Fig. 5-6 (a) and (b): μ (V_{CNP}) and $\sigma_{min}(V_{CNP})$ for suspended BLG devices. The blue symbols denote devices in region II.

Two striking features are evident: (1) μ decreases with increasing V_{CNP} in agreement with previous reports in substrate supported graphene [57, 128], suggesting that charged impurities remain important scatterers even in these high mobility devices; (2) the insulating-BLG devices in Fig. 5.6 cluster around V_{CNP}=0. Thus, the insulating behavior in BLG at the CNP is only observed in devices with *both* high mobility and low charged impurity density. The insulating state, apparently masked by impurities in group I samples, cannot be explained by single-particle physics.

5.4 Temperature dependence of BLG devices

Fig. 5.7 displays $\sigma(V_{bg})$ at different temperatures T for suspended insulating BLG, suspended non-insulating BLG and substrate-supported BLG devices, respectively. We observe minimal T-dependence for the substrate-supported devices. For both suspended devices, σ at large doping is only weakly temperature dependent, whereas σ at half-filling decreases sharply with temperature. In particular, $\sigma_{min}(T)$ of the

insulating BLG has the strongest *T*-dependence, falling by several orders of magnitudes to ~ 0.05 e^2/h.

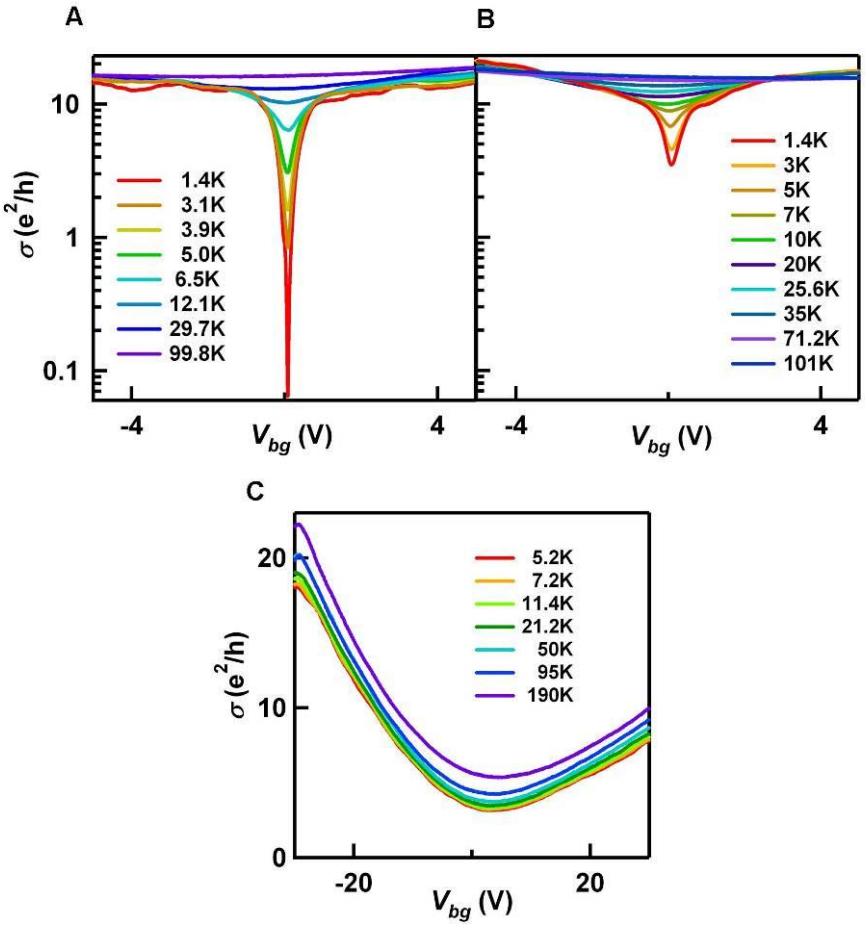

Fig. 5-7 (a) and (b): Temperature-dependent σ (V_{bg}) for suspended insulating and noninsulating BLG devices, respectively. (c): Temperature dependent σ(V_{bg}) for a substrate supported BLG device.

To obtain further insight we compare the temperature dependences of group I and group II devices. Fig. 5.8(a) displays σ_{min} on a logarithmic scale *vs 1/T* for 1.4≤*T*≤100 K for one non-insulating device and two different insulating BLG devices. The inset plots the same data sets $\sigma_{min}(T)$ on linear-log scales. Amazingly,

for 10<T<100K, the $\sigma_{min}(T)$ curve of all 3 devices collapse into a single curve. This is in contrast with the previous work on single layer [129] and trilayer graphene [130, 131], which reported large sample-to-sample variation in $\sigma_{min}(T)$, thus strongly suggesting that we are indeed observing intrinsic attributes of BLG.

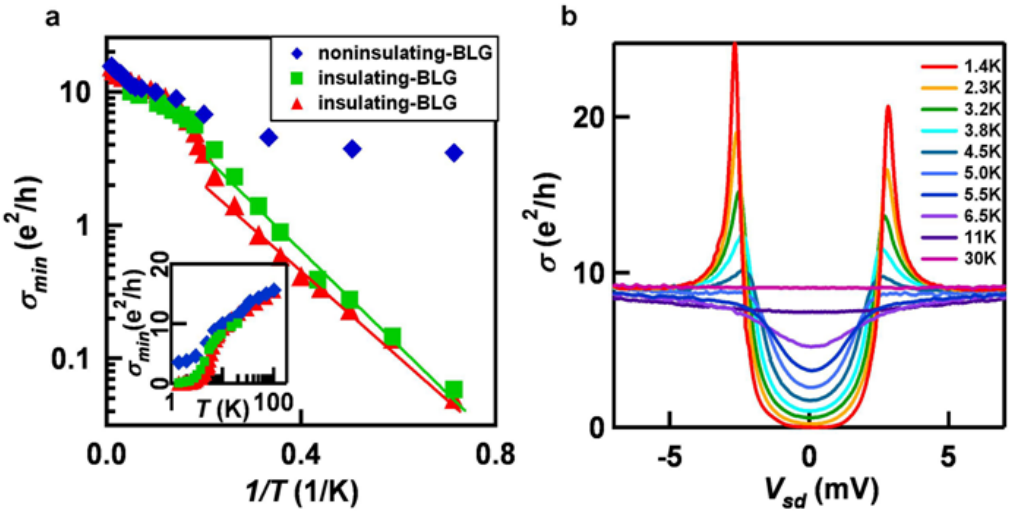

Fig. 5-8 (a) $\sigma_{min}(1/T)$ for insulating and noninsulating-BLG devices. Inset: $\sigma_{min}(T)$ of data set. The solid lines are fits to data T<5K to $\sigma_{min}(T)=Aexp(-E_A/2k_BT)$. (b) T-dependence of $\sigma(V_{sd})$ at CNP for an insulating-BLG device.

Notably, the behaviors of the two types of devices start to deviate at ~ 5-7 K – σ_{min} of the non-insulating device decreases only modestly for T<5K; in contrast, the σ_{min} of both insulating ones exhibit an abrupt change in slope and drops precipitously, where the data are well-described by $\sigma_{min}(T)=A\ exp(-E_A/2k_BT)$ (here A is the pre-factor, E_A is the activation energy and k_B is the Boltzmann constant). The best fit is obtained by using A=17 e^2/h and E_A~18K, indicating thermally activated transport over a gap >~ 1.6 meV.

These data suggest the presence of a gap in insulating devices for T<5K. To investigate this further, we focus on σ *vs.* source drain bias V_{sd} at the CNP [122, 123](Fig. 5.3b). At T=1.4K, σ increases precipitously when $|V_{sd}|$ increases from 0, adopting a "U"-shaped profile and reaching two dramatic peaks at ±2.8 mV, and deceases again to ~ $8e^2/h$ for $|V_{sd}|>5$mV. Such a $\sigma(V_{sd})$ curve strongly resembles the density of states (DOS) for gapped phases such as superconductors or charge density waves, and in particular, the DOS of a gapped BLG near the CNP. Since the device has symmetric coupling to both electrodes, we take the magnitude of the gap to be half of the separation between the two peaks, ~2.8 meV. This is larger than the value ~1.6 meV obtained from thermal activation measurements, but hardly surprising since the gap probably increases with decreasing T. Thus, the $\sigma(V_{sd})$ curves, together with the $\sigma_{min}(T)$ measurements, unequivocally establishes the presence of a low-temperature gap ~ 2-3 meV in group II BLG's spectrum.

We now examine the $\sigma(V_{sd})$ curves of the insulating device at different temperatures (Fig. 5.3b). When T increases from 1.4 K, σ_{min} increases, $\sigma(V_{sd})$ adopts a "V"-shaped profile, and the magnitudes of the two peaks decrease and vanish entirely at ~5K (Fig. 5.3b). All these observations suggest the disappearance of the gap for T>5K. Our data thus provide strong evidence for a finite temperature phase transition to an insulating state with a critical temperature T_c~5K and a gap Δ/k_B (~20-30K). Because the gap disappears with temperature, it cannot be due to single-particle origin, and must arise from many-body interaction effects. The rough correspondence

between the critical temperature and gap scales suggests that the broken symmetry is reasonably well described by mean-field theory.

Our data thus far suggests a *T*-dependent phase transition in charge-neutral BLG between a metallic phase and an interaction-induced insulating phase. This metallic phase could be manifestation of single particle effects, or alternatively, could consist of domains of gapped phases with opposite pseudospin polarizations. Future experiments would be necessary to ascertain the nature of the metallic behavior at the CNP.

5.5 Quantum phase transition in BLG devices

An intriguing possibility is that a quantum phase transition, *i.e.* one that is tuned by parameters other than *T* such as disorder or electric field may take place at T=0. To this end, we examine the $\sigma(V_{sd})$ curves of 2 non-insulating devices, which have mobility 140,000 and 24,000 cm^2/Vs, respectively, at T=1.4K (Fig. 5.9a). Data from an insulating device is also plotted for comparison. Remarkably, the $\sigma(V)$ of both non-insulating devices bear a striking resemblance to those of insulating BLG at higher temperatures. In particular, the device with μ=140,000 cm^2/Vs has a "V-shaped" profile at small V_{sd}, elevated σ_{min} and smaller peaks at V_{sd} ~$\pm$2.5 mV, and resembles the curve in Fig. 5.9(b) at T~4K. For the one with μ=24,000 cm^2/Vs, $\sigma(V)$ is flatter without the side peaks, thus resembling the curve from the insulating device at T~10K. Taken together, charge disorder has a similar effect as temperature

by annihilating the broken symmetry gaps of all the BLG spin-valleys.

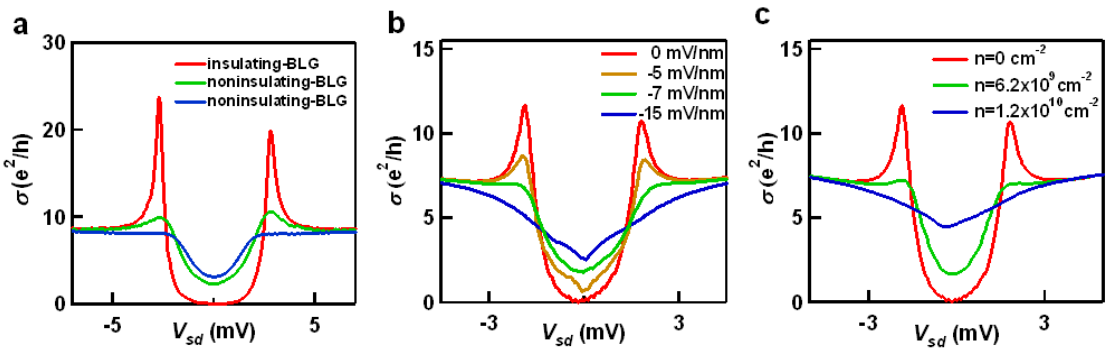

Fig. 5-9 (a) $\sigma(V_{sd})$ for insulating and noninsulating-BLG devices at the CNP. (b) $\sigma(V_{sd})$ at $n=0$ for a doubly gated BLG at $E_\perp$=0, -5, -7 and -15 mV/nm. (c) (V_{sd}) at $E_\perp$=0 for a doubly gated BLG at different values of n.

Finally we examine the influence on the insulating state of changes in carrier density and of an applied $E_\perp$ that induces an interlayer potential difference (*24*). In our doubly gated BLG devices we can control n and $E_\perp$(*24*) independently. Several line traces of $\sigma(V_{sd})$ for different values of $E_\perp$ are shown in Fig. 5.9(b). As $E_\perp$ increases from 0 to -7mV/nm, the "U"-shaped $\sigma(V_{sd})$ curve becomes "V"-shaped, with less prominent side features and an elevated σ_{min}, *i.e.* the gap size appears to be diminished by $E_\perp$. For still larger fields the well-known single-particle gap [44, 113, 132] of unbalanced bilayers gradually emerges. The influence of total carrier density on the insulating state is extremely sharp. At $E_\perp$=0 (Fig. 5.9c) – a small density $n \sim 6.2 \times 10^9$ cm^{-2} is sufficient to significantly obscure the gapped correlated state; when $n \sim 1.2 \times 10^{10}$ cm^{-2}, the gapped feature completely vanishes and σ_{min} reaches $\sim 5e^2/h$.

Our experimental results thus provide strong evidence for a quantum phase

transition between insulating and conducting states that is tuned by $E_\perp$, n or charge disorder. Indeed these transitions are expected in the mean-field theory (MFT) of gapped spontaneous quantum Hall states in BLG. These states break layer inversion symmetry in each spin-valley flavor which improves electronic correlations and induces large momentum space Berry curvatures. Consequently, there are quantized anomalous Hall contributions which change sign with the sense of layer polarization of flavors. Increasing carrier density works against broken symmetry order by Pauli blocking layer polarization and by increasing screening. MFT predicts that the spontaneous quantum Hall states disappear once the carrier density is larger than $1.47 \times 10^{10}\ \mathrm{cm}^{-2}$ which is consistent with our experimental findings. The role of temperature is similar to that in BCS theory of superconductivity and there is no *Anderson Theorem* to mitigate the role of disorder. Quite different with T and n, further increasing $E_\perp$ reopens the gap and induces a phase transition to a layer-polarized state with an abrupt change of the band topology only for two of the four flavors [116, 133]. Such a gap is expected to increase with $E_\perp$ and is enhanced by correlations as well.

Chapter 6. Stacking-Dependent Band gap opening in Trilayer Graphene

In multilayer graphene [130, 134], stacking order provides an important yet rarely-explored degree of freedom for tuning its electronic properties[135]. For instance, Bernal-stacked trilayer graphene (B-TLG) is semi-metallic with a tunable band overlap, and rhombohedral-stacked (r-TLG) is predicted to be semiconducting with a tunable band gap [41-44, 107, 136-139]. These multilayer graphene sheets are also expected to exhibit rich novel phenomena at low charge densities due to enhanced electronic interactions and competing symmetries.

In this chapter we demonstrate the dramatically different transport properties in TLG with different stacking orders, and the unexpected spontaneous gap opening in charge neutral r-TLG. At the Dirac point, B-TLG remains metallic while r-TLG becomes insulating with an intrinsic interaction-driven gap ~6 meV. Our results underscore the rich interaction-induced phenomena in trilayer graphene with different stacking orders, and its potential towards electronic applications.

6.1 Introduction

The distinctive band structures in B-TLG and r-TLG discussed in section 1.6.4 are expected to give rise to different transport properties. For instance, owing to the cubic dispersion relation, r-TLG is expected to host stronger electronic interactions than B-BLG. This is because the interaction strength r_s is approximately the ratio of the inter-electron Coulomb energy to the Fermi energy. In graphene, $r_s \propto n^{-(p-1)/2}$,

where n is charge density and p is the power of the dispersion relation; p=1, 2, 3 for SLG, BLG and r-TLG, respectively[140]. Consequently, at low n, the interaction strength in r-TLG is significantly higher than that in SLG, BLG and B-TLG (the last can be considered as a combination of SLG and BLG) [116]. Hence, r-TLG potentially allows the observation of interaction-driven phenomena, *e.g.* spontaneous gap formation, that are not easily accessible in BLG or B-TLG. Thus we seek to experimentally explore the transport properties of TLG with different stacking orders.

The stacking order of the devices is identified using Raman spectroscopy [141]. In particular, the 2D peak of r-TLG is more asymmetric with a pronounced shoulder than that of B-TLG (Fig. 6.2).

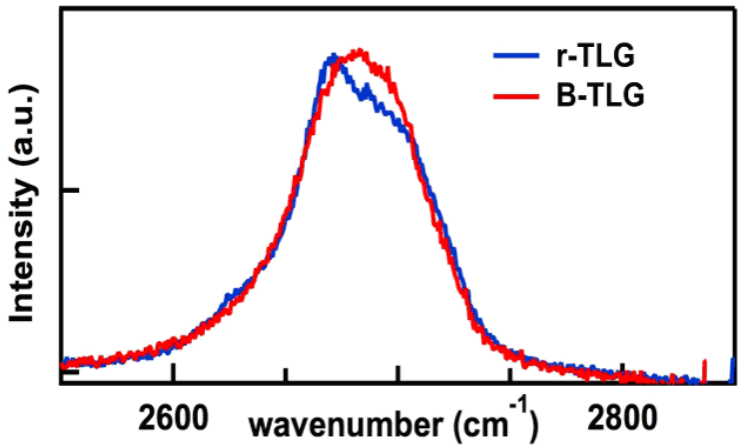

Fig. 6-1 Raman spectroscopy of TLG with different stacking orders.

6.2 Device fabrication, current-anneal-cleaning and chracterization

Graphene devices are fabricated by shadow mask evaporation of electrodes onto graphene sheets that are either supported on substrates or suspended across

pre-defined trenches in Si/SiO_2 substrates. These devices have no contaminants introduced by lithographical processes, with field effect mobility μ ranging from 210 to 1900 cm^2/Vs for non-suspended devices, and 5000 to 280,000 for suspended samples, which are significantly higher than those fabricated by lithography. We measure their electrical properties using standard lock-in techniques in a He^3 or pumped He^4 cryostat.

Similarly to BLG devices, we also current anneal TLG devices before measurement. Such annealing is performed at 4 K in vacuum by slowly ramping up the applied voltage while monitoring the current. Typically, optimal annealing is reached when the measured current starts to saturate (Fig. 6.3(a)); the applied voltage is then ramped down to zero. A representative saturation current is about 0.2mA/μm/layer for both Bernal and rhombohedral stacking suspended TLG samples.

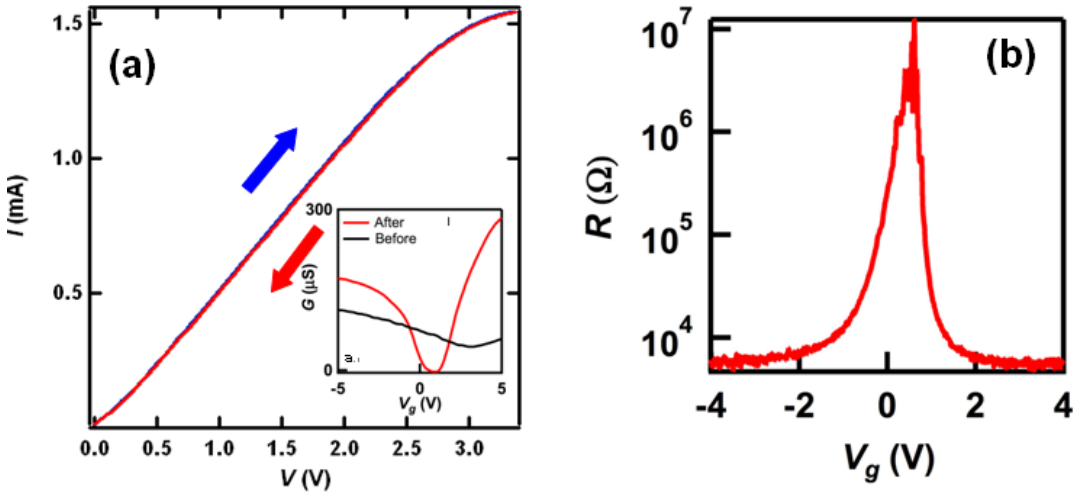

Fig. 6-2 (a) Current-voltage characteristics of a trilayer graphene devices during current annealing. The arrows indicate voltage ramping direction. Optimal annealing is reached when current starts to saturate.

Inset of (a): G(Vg) of an r-TLG device before and after annealing. (b) R(Vg) data of this device in logarithmic scale at T=1.5K. Note that R_{max}~10MΩ.

After current annealing, the devices exhibit much higher mobility, with the charge neutrality point shifting to almost zero. For r-TLG devices, the minimum conductivity decreases significantly with annealing (Fig. 6.3(b)).

Fig. 6.4 displays the two-terminal conductance G of two suspended TLG devices with different stacking orders as a function of back gate voltage V_g at T=1.5K. Both curves are "V"-shaped, characteristic of high mobility samples.

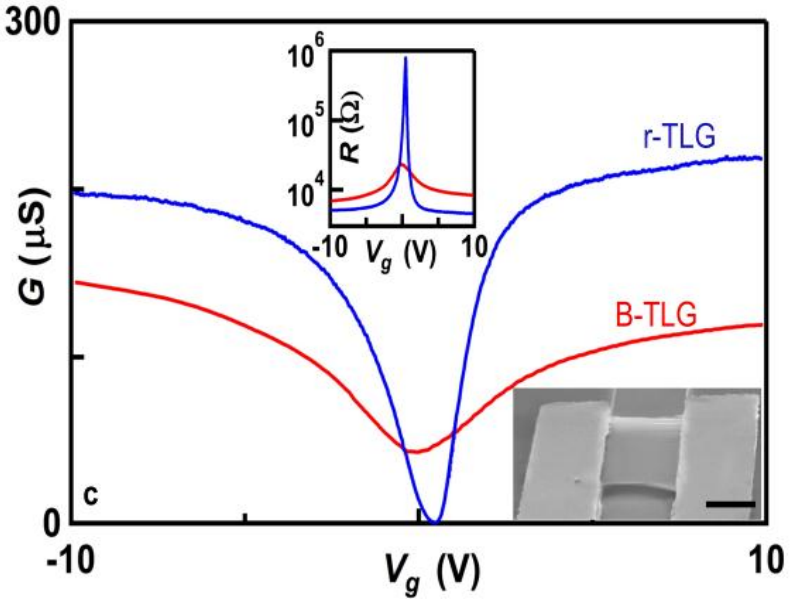

Fig. 6-3 $G(V_g)$ for two different suspended TLG devices at T=1.5K. Upper inset: $R(V_g)$ in log-linear scales for the same devices. Lower inset: SEM image of a suspended graphene device. Scale Bar: 2 μm.

Surprisingly, the two devices display drastically different minimum conductance G_{min} at the charge neutrality point (CNP) – G_{min} for B-TLG is ~ 50 μS, but <~1 μS

for r-TLG. The strikingly large difference in minimum conductivity σ_{min}, as well as the very low σ_{min} in certain high mobility samples, is unexpected and unique to TLG.

6.3 Effect of stacking order on s_{min} of TLG devices

To systematically examine the effect of stacking order on σ_{min}, we investigated 21 substrate-supported and 22 suspended devices. After electrical measurements, the stacking order of the devices are identified using Raman spectroscopy [141]. Our findings are summarized in Fig. 6.5, which plots σ_{min} at T=4K *vs.* the field effect mobility μ, revealing several interesting observations.

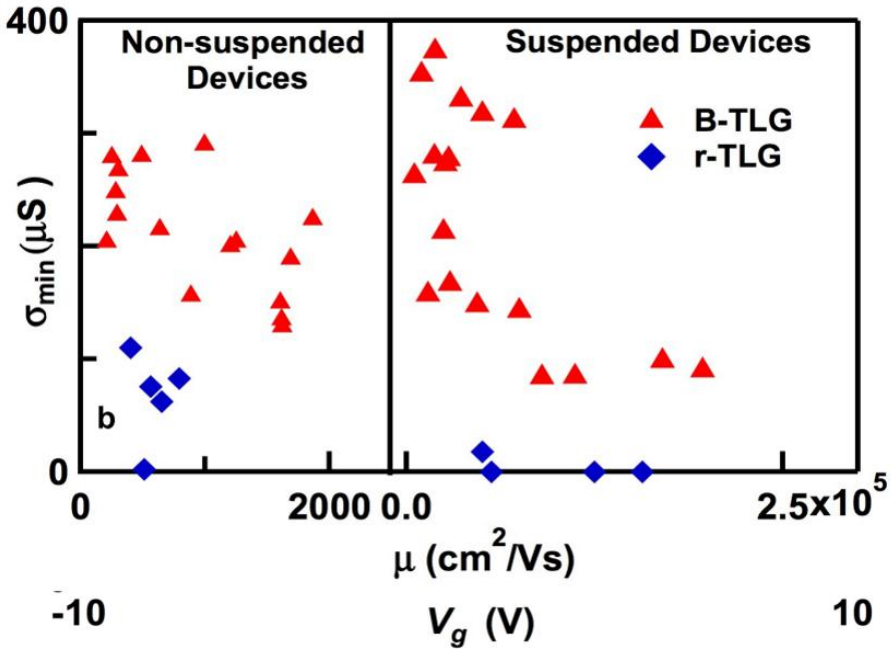

Fig. 6-4 Minimum conductivity σ_{min} *vs.* field effect mobility μ at 4K for suspended and non-suspended graphene devices.

For instance, for all B-TLG devices, σ_{min} decreases with increasing sample

mobility but remains finite, presumably because the same scattering mechanisms that yield low mobility also give rise to electron and hole puddles [142], hence smearing Dirac points and leading to higher σ_{min}. Amazingly, σ_{min} for r-TLG devices is significantly smaller than B-TLG. The difference is at least a factor of 2 or 3 for substrate-supported devices, and becomes dramatic for suspended devices – $\sigma_{min,\ B\text{-}TLG}$ remains almost constant at ~100 μS for $\mu > 5 \times 10^4$ cm^2/Vs, while $\sigma_{min,\ r\text{-}TLG} \sim 0$, suggesting the presence of metallic and insulating states, respectively.

6.4 Temperature dependence of TLG devices

The insulating state in neutral r-TLG is not anticipated from non-interacting electron pictures. To elucidate its nature and compare transport in TLG with different stacking orders, we investigate the devices' temperature dependence. Fig. 6.6 (a) and (b) plot the $G(V_g)$ curve for B- and r-TLG devices, respectively, at T between 1K and 120K.

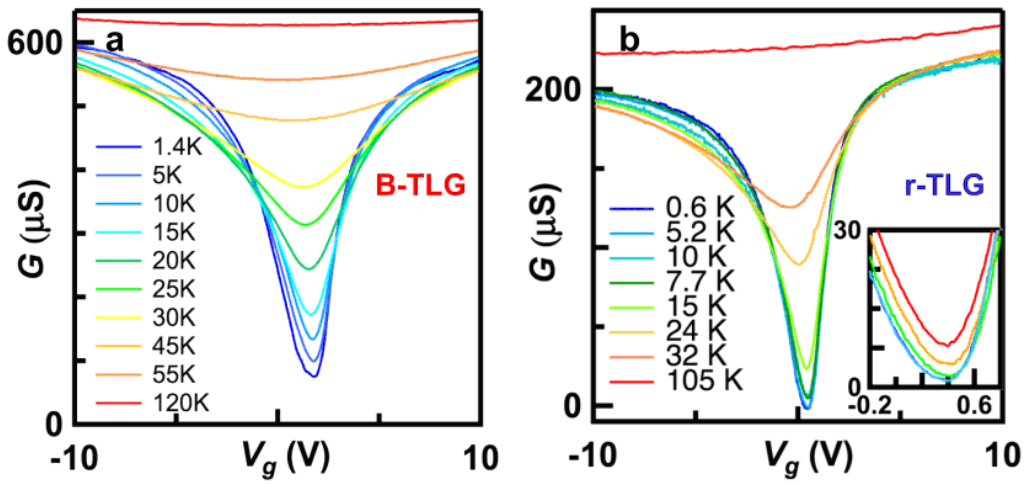

Fig. 6-5 (a) and (b): $G(V_g)$ for B- and r-TLG devices, respectively, taken at different temperatures. Inset in (b): Zoom-in plot of $G(V_g)$ curves at T=0.6, 0.8, 5.2, 7.7 and 10K (bottom to top). The curves at 0.6 and 0.8 K are indistinguishable.

In both data sets, G at small n declines quickly with temperature, but stays almost constant or increases modestly for high n. The opposite $G(T)$ dependence in these two density regimes is similar to that observed in SLG [25, 129], where the weak T-dependence at large n is attributed to electron-phonon interaction [129].

At the CNP, $G_{min,\ B\text{-}TLG}$ displays a moderate T-dependence, typically decreasing by a factor of 2 -8 when T is reduced from 200 to 1.4K (Fig. 6.7 (a)). Variable range hopping, which has an stretched exponential T-dependence, cannot adequately describe the data. We thus compare data in Fig. 6.7(a) to a model of thermally activated transport

$$G_{\min} = G_0 + A\mathrm{e}^{-E_A/k_BT} \tag{3.4}$$

where E_A is the activation energy, k_B the Boltzmann constant, and G_0 and A are fitting parameters. An adequate fit to Eq. (3.4) can be obtained by using E_A=25K, though

the fit is not entirely satisfactory.

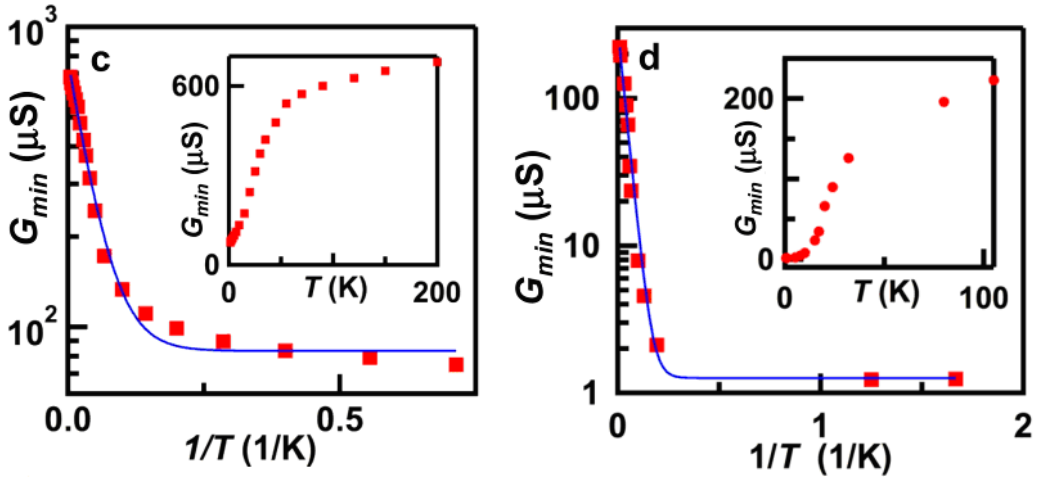

Fig. 6-6 (a) and (b): G_{min} *vs. 1/T*. The blue lines are best fits to Eq. (3.4), with E_A=25K and 32K for B-stacked and r-stacked TLG, respectively. Insets: $G_{min}(T)$ for the same data sets shown in the main panels.

In contrast, G_{min} of r-TLG displays an exceedingly strong temperature dependence – it decreases exponentially with $1/T$ by 2-3 orders of magnitude for 5<T<105K, crossing over to a constant value at lower temperatures (Fig. 6.7(b)). Using E_A=32.0K, we obtain excellent agreement between the experimental data and Eq. (3.4), demonstrating that transport in r-TLG at the CNP occurs via thermal activation through an energy gap of $2E_A$ ~5.5 meV. The constant G_0 is sample-dependent, and decreases from 10 to 0.1 μS with improved mobility, indicating that it arises from scattering from residual impurities on the suspended membranes.

6.5 Insulating state in r-TLG devices

To gain further insight into the insulating state of r-TLG, we measure its differential conductance *dI/dV* at *T*=300 mK *vs.* V_g and source-drain bias *V* (Fig. 6.8(a)). The resulting stability diagram reveals a diamond-like structure centred at CNP, where *dI/dV* ~0 at *V*=0. For *V*>0.7 mV, *dI/dV* increases almost linearly with bias up to 15 mV with a width of ~7.5 mV, consistent with that determined from the activation energy. As *V* increases further to ~21 mV, *dI/dV* rises sharply to ~ 400 μS within 2mV (Fig. 6.8(b)). Such an abrupt jump in *dI/dV* strongly resembles that in charge neutral bilayer graphene as described in Chapter 5, with the difference that the profile of the curve is "V"-shaped as opposed to "U"-shaped. This is reasonable since here our TLG devices are single gated thus we cannot tune the internal electrical field, which can destroy this intrinsic insulating state at the CNP.

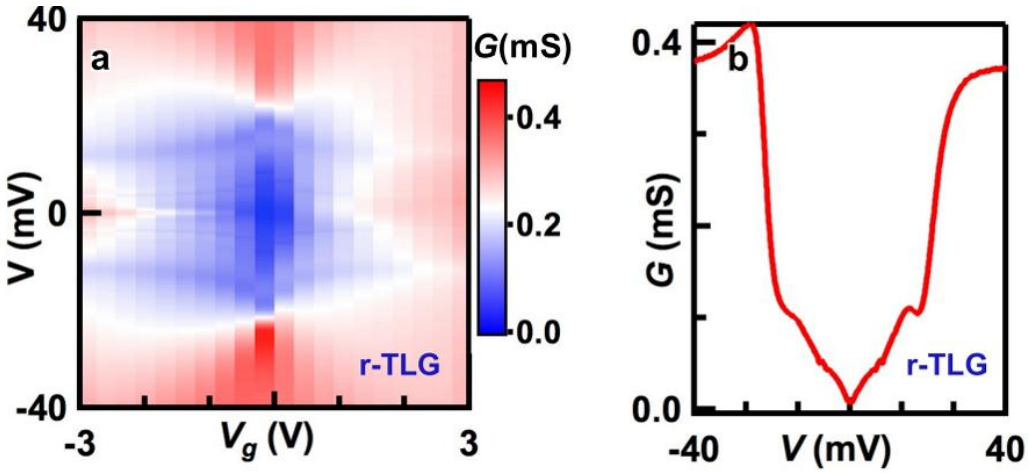

Fig. 6-7 (a) *dI/dV*(V_g,*V*) for an r-TLG at *B=0* and *T*=300mK. (b) Line trace of (a) at V_g=0.

To sum our experimental findings: at B=0, we find that B-TLG remains metallic at the CNP, while r-TLG becomes insulating at low temperatures. G_{min} of the latter is thermally activated for T>5K, with a gap-like feature in its dI/dV curve. Taken together, these results strongly suggest the presence of an intrinsic band gap in r-TLG. Such a gap is not anticipated from tight-binding calculations, and likely arises from electronic interactions, as expected from r-TLG's large interaction parameter r_s. For instance, a band gap may occur if spatial inversion symmetry is broken by strain or an external electric field, or if electronic interactions cause spontaneous symmetry breaking such as those predicted [117, 143, 144] or reported [120] for BLG. Drawing from our BLG data, we believe that the gap opening in r-TLG is interaction-driven, and may be as large as 30 meV (the bias value at which the sharp rise in G occurs), if TLG is double-gated, so that both n and electric field can be tuned to zero.

Chapter 7. Controlled Ripple Texturing of Suspended Graphene

In this chapter we discuss a direct observation and controlled creation of one- and two-dimensional periodic ripples in suspended graphene sheets, using both spontaneously and thermally generated strains.

By elucidating the ripple formation process, which can be understood in terms of classical thin-film elasticity theory, we are able to control ripple orientation, wavelength and amplitude by controlling boundary conditions and thermo-mechanical manipulation. In the end of this chapter we also use *in-situ* SEM imaging to exploit graphene's negative thermal expansion coefficient, which we measure to be much larger than that of graphite.

Our results should lead to a better understanding of suspended graphene devices [145, 146], controlled engineering of thermal stress in large scale graphene electronics, and enabling a systematic investigation of the effect of ripples on the electronic properties of graphene.

7.1. Introduction

Ripples are an intrinsic feature of graphene sheets [147], similar to those seen on plastic wrap tightly pulled over a clamped edge.

Induced by pre-existing and/or thermally generated strains in graphene, ripples in graphene are expected to strongly influence electronic properties by inducing effective magnetic fields and changing local potentials [148-153]. Thus the ability to control ripple structure in graphene could enable device design based on local strain [154] and selective bandgap engineering [155].

On the other hand, despite a theoretical calculations and debate [156-158] over graphene's negative thermal expansion coefficient (TEC), TEC has never been experimentally measured in graphene. In this chapter we will use a special *in-situ* SEM imaging method to exploit graphene's negative TEC, which we measure to be much larger than that of graphite.

7.2. Device fabrication, furnace cleaning and ripple chracterization

Suspended graphene membranes are prepared by the standard mechanical cleavage technique on Si/SiO_2 wafers with pre-patterned trenches. Membranes that are 1, 2 and 3-layer thick are identified by color contrast in an optical microscope and/or Raman spectroscopy. The Si substrates are *p*-doped to act as back gates, and the thickness of silicon and SiO_2 are 500 μm and 300 nm, respectively. The trenches are defined by photolithography followed by plasma etching in a reactive ion etcher

(RIE) system. The depths of trenches range from 100 to 250 nm, and width from 2 to 4 μm. Devices with electrodes are fabricated by direct deposition of Ti/Au metals through shadow masks that are carefully aligned to selected graphene sheets.

The graphene membranes are annealed in a standard chemical vapor deposition (CVD) furnace in argon gas at a flow rate 0.6 slm for 20 minutes. The annealing temperature varies from 400K to 750K. Some of the membranes are annealed inside an SEM chamber in vacuum, as will be discussed below.

Graphene membranes, ranging from single layers to ~ 16 nm in thickness, and ~0.5 to 20 μm in width, are suspended across pre-defined trenches on Si/SiO_2 substrates. We examine their morphology under a scanning electron microscope (SEM) or an atomic force microscope (AFM).

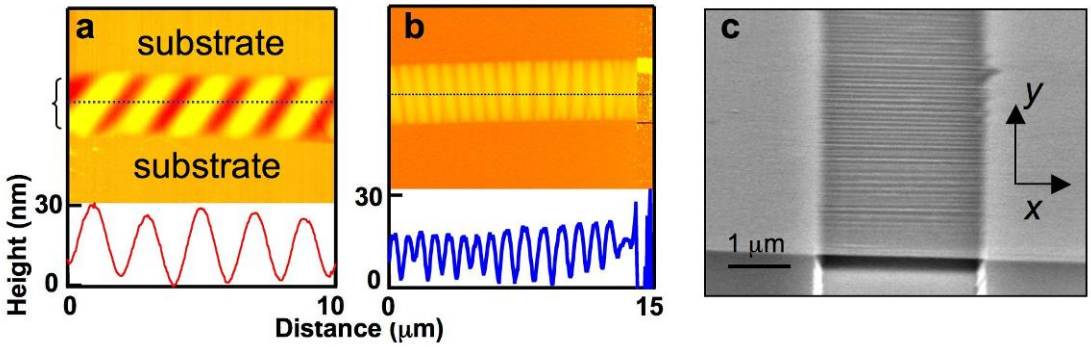

Fig. 7-1 (a) and (b) Data from two different graphene membranes suspended across trenches. The center horizontal stripe, indicated by the left bracket in (a), corresponds to the trench. Upper panels: AFM topographical images. Lower panels: line traces taken along the dotted lines. Note the different amplitudes and wavelengths of the devices. (c) SEM image of a bi-layer suspended membrane.

Strikingly, most of the graphene sheets are not flat, but spontaneously form

nearly periodic ripples (Fig. 7.1). Typically, the ripple crests are perpendicular to the edges of the trench (*y*-direction), although oblique ripples (i.e. with crests at an angle to the trench) are occasionally observed. The out-of-plane displacement ζ of the ripples is well-described by a sinusoidal function,

$$\zeta = A\sin(2\pi y/\lambda). \quad (4.1)$$

where A is the amplitude and λ the wavelength. We have imaged and measured more than 50 different membranes, with A ranging from 0.7 to 30 nm, and λ ranging from 370 nm to 5 μm.

We also observe that the ripples in graphene are not visible in SEM unless the device is imaged at a high tilting angle, typically 75-85 º. As shown in Fig. 7.2, the graphene membrane appears to be flat and ripple-free when imaged at 0 º (*i.e.* top view) or 45 º; however, when imaged at large angles (>75 º), the membrane displays prominent, periodic ripples. The majority of the images presented in the manuscript are taken at 80 º.

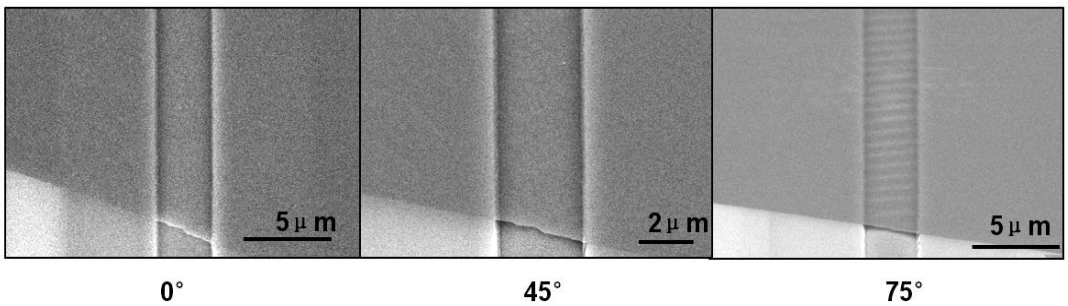

Fig. 7-2 SEM Images of a graphene sheet imaged at different tilting angles. Note that the ripples are observable only at a large tilting angle, >75 º.

Most of the as-prepared graphene membranes display strain-induced ripples. Occasionally, however, flat graphene or sagging sheets are also observed (Fig. 7.3).

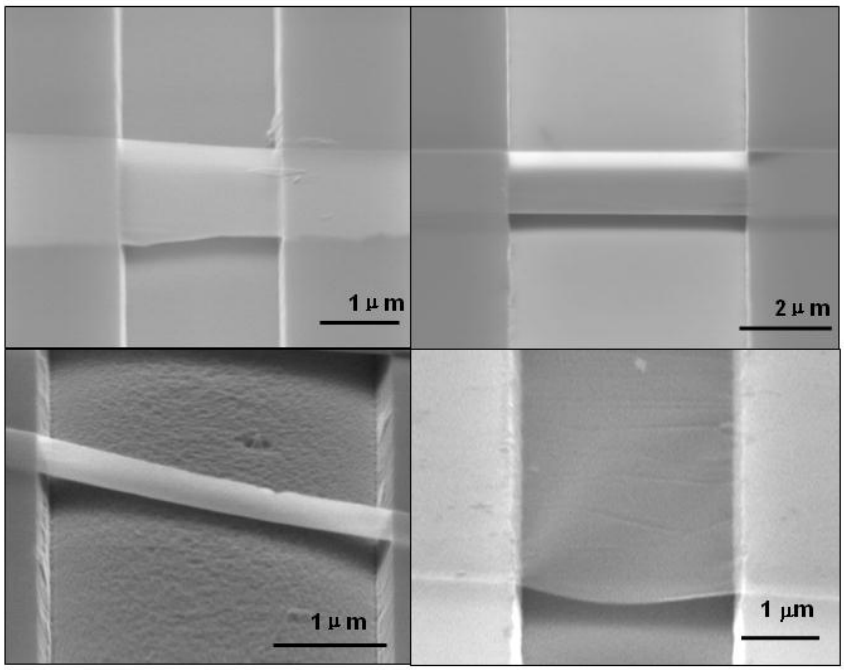

Fig. 7-3 SEM images of several different as-deposited few-layer graphene membranes.

To understand the origin of these ripples, we note that for an elastic thin film, ripples described by Eq. (4.1) may be induced by either transverse compression in the *y* direction, or by longitudinal strain and/or shear in the *x*-direction [159]. From classical elasticity theory [160], we expect the clamped boundary conditions imposed by the banks of the trenches suppress lateral movement and induce local biaxial stress. For a thin film of thickness *t* with clamped boundaries at $x=0$ and $x=L$, the presence of a longitudinal tensile strain γ leads to [159]:

$$\frac{\lambda^4}{(tL)^2} = \frac{4\pi^2}{3(1-\nu^2)\gamma} \tag{4.2a}$$

and

$$\frac{A^2}{\nu tL} = \left[\frac{16\gamma}{3\pi^2(1-\nu^2)}\right]^{1/2}. \tag{4.2b}$$

Here ν is the Poisson ratio, which is predicted to range from 0.1 to 0.3 for single layer graphene [161, 162]. Combining Eqs. (4.2a) and (4.2b), we eliminate γ and obtain an equation with only experimentally accessible parameters:

$$\frac{A\lambda}{L} = \sqrt{\frac{8\nu}{3(1-\nu^2)}}t \ . \tag{4.3}$$

If instead the applied stress is dominated by in-plane shear, the equation takes a different prefactor [163]:

$$\frac{A\lambda}{L} = \sqrt{\frac{8}{3(1+\nu)}}t \ . \tag{4.4}$$

Using values of *A*, *L*, λ and *t* as determined from AFM images, we plot $A\lambda/L$ vs. *t* for 51 devices that display periodic ripples, as shown by the data in Fig. 7.4. Eqs. (4.3) and (4.4) are plotted as the lower and upper lines, respectively, using ν=0.165 [164] for graphite in the basal plane, which is well within the theoretical range of values.

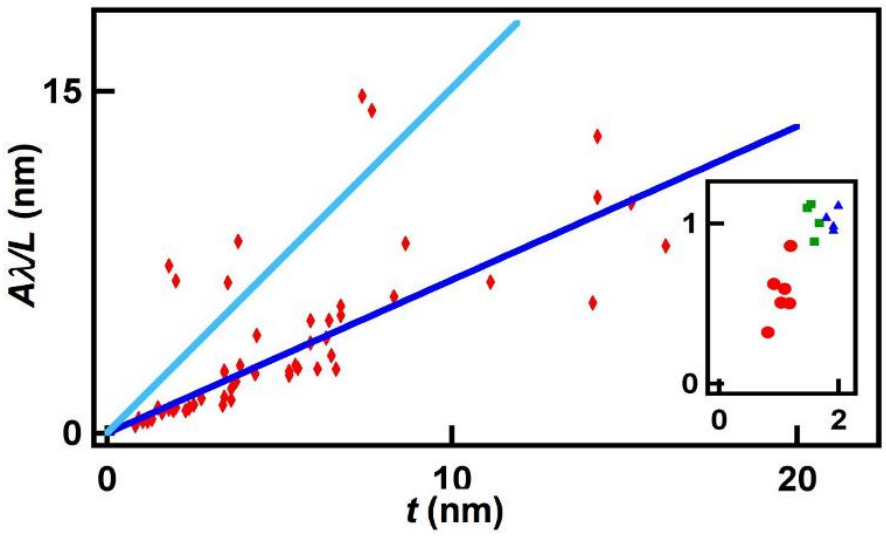

Fig. 7-4 $A\lambda/L$ vs t for 51 membrane devices. The lower and upper lines are calculated using ν=0.165 and Eqs. (3) and (4), respectively. Inset: $A\lambda/L$ vs t for single(red)-, bi(green)- and triple(blue)- layer devices. The number of layers is inferred from colour contrast in optical microscope, though only measured thickness is used.

We notice that most of the data points fall on the lower solid line, indicating that the ripples are induced by pre-existing longitudinal strains in graphene. However, the 6 data points that fall above the upper line have a similar slope to the latter, suggesting the presence of shear in these devices. Actually Eqs. (4.2) – (4.4) are derived based on classical thin-film elasticity theory, and may not be valid a *priori* for atomically thin membranes. The inset of Fig. 7.4 displays $A\lambda/L$ vs. t for samples that are 1, 2 and 3 layers thick. Remarkably, the data points falls on a straight line, suggesting that Eq. (4.3) holds even for single atomic layer membranes.

The strains in these atomic membranes, while difficult to determine using conventional techniques, can be readily obtained from Eq. (4.2a) or (4.2b). In Fig.

7.5, we use Eq. (4.2a) to compute γ for membranes with strain-induced ripples, and plot γ vs t. For thicker films, γ is relatively small, ~0.016% to 0.3%. In contrast, thinner films are more easily strained, and exhibit γ up to 1.5%.

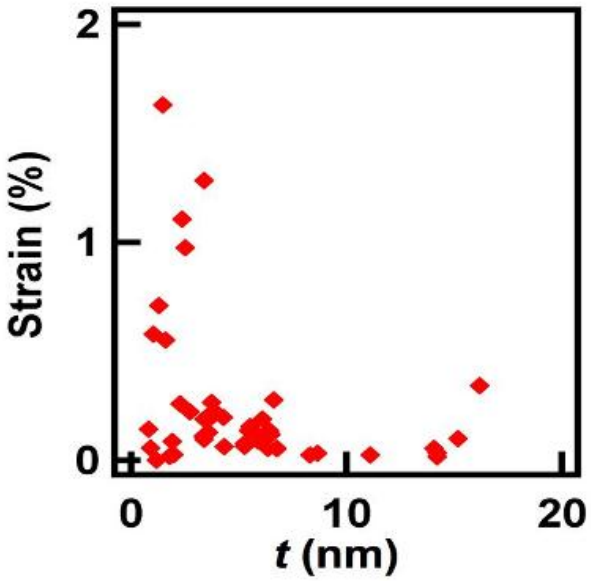

Fig. 7-5 Strain in suspended devices, calculated using Eq. (4.2a).

7.3 Thermal manipulation of graphene ripples

The above observation of periodic ripples in graphene membranes suggests that they can be further controlled to enable strain-based graphene electronics. Here we show that ripples can be controllably produced via simple thermal manipulation. The graphene membranes are annealed in a furnace in argon up to 700 K, and imaged again at room temperature. Surprisingly, almost all graphene membranes undergo dramatic morphology changes, displaying one or both of the following changes: (1) the ripple geometry is significantly altered, with apparently larger amplitudes and longer wavelengths (see also Fig. 3a); (2) the graphene membrane buckles, typically sagging toward the substrate, or occasionally buckling upwards. In fact, the buckling can be quite dramatic: the central portions of several membranes settled on the bottom of the trenches *without breaking*.

To understand these observations, we perform *in situ* SEM imaging of our devices at different temperatures *T*, using a custom-built SEM stage with a built-in heater and a thermocouple. Standard graphene samples on silicon substrates (4 mm x 4 mm x 0.5 mm) were mounted to a heated aluminum base plate using a thin layer of high-temperature cement (thermal conductivity 1.6 W/m.K). Temperature was measured using a fine-gage K-type thermocouple (diameter 2 mil ≈50 μm) cemented directly to the top of the silicon chip. To minimize errors in the temperature measurement, the thermocouple bead was embedded approximately 1 mm into the cement and located as close as practical to the top of the silicon (Fig. 7.6).

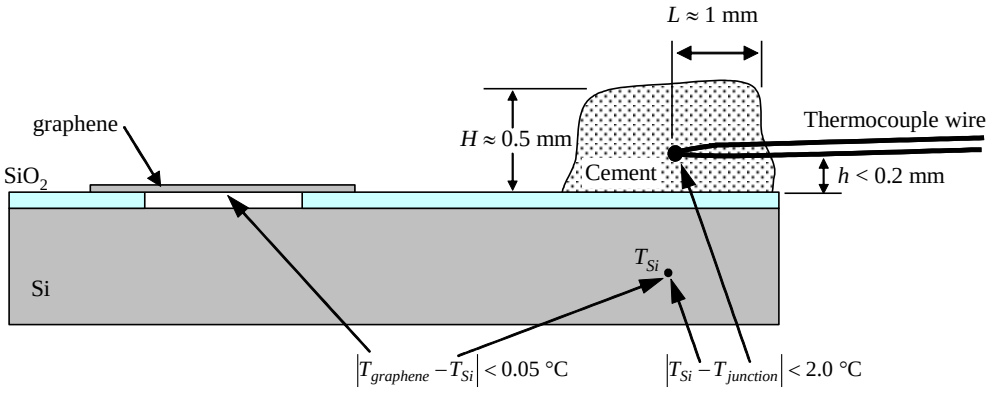

Fig. 7-6 Schematic of the heater stage for *in situ* SEM imaging.

This configuration exploits heat conduction through the cement to bring the temperature of the thermocouple junction as close as possible to the temperature of the silicon substrate. We assume conservative values for the thermal conductivity of the thermocouple wires (50 W/m-K), and the worst-case emissivity (ε=1) of all materials. Using standard heat transfer theory, we calculate that the temperature of the thermocouple junction is within 2K of the silicon temperature even at 725K. We have also conservatively estimated the temperature difference between the silicon and the center of the graphene flake to be 0.05K or less, which considers temperature gradients within the silicon, heat transfer through the oxide layer, contact resistance between graphene and oxide, heat conduction through the graphene, and black-body radiation to the surroundings. Taken together, the overall uncertainty in our temperature measurement is estimated as 4K at 725K, with the largest contribution simply being the uncertainty in the thermocouple calibration.

Fig. 7.7 (a) and (b) show image sequences for two different membranes. When *T* is raised to 450-600K, the membranes are flat, and any pre-existing ripples almost completely disappear. However, upon cooling down to 300K, ripples invariably appear, usually with much larger amplitudes than any pre-annealing ones. The device in Fig. 7.7(b) also exhibits longitudinal buckling and sags into the trench.

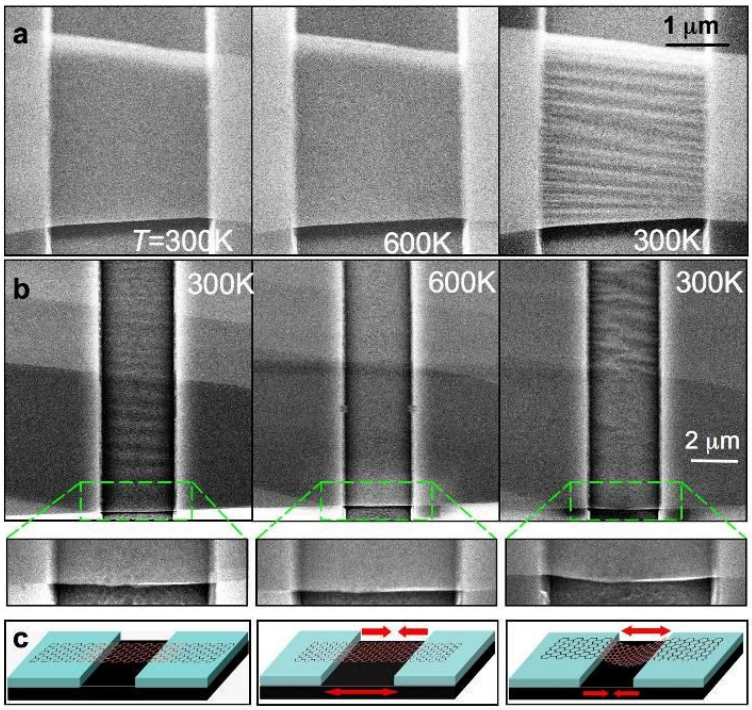

Fig. 7-7 Dependence of ripple morphology on temperature. (a-b) *In situ* SEM images of two devices taken before, during and after annealing. Bottom panels of (b) are higher magnification images of the edge of the graphene membrane, which sags into the trench after annealing. (c) Schematic of buckling of a graphene membrane due to thermal contraction. From left to right, the panels depict the membrane in its original state, during heating and during cooling, respectively. The arrows indicate the contraction/expansion of the substrate and graphene.

The above observations suggest that, after thermal annealing, a graphene sheet experiences biaxial compression [165]; the different behaviours (rippling *vs.*

buckling) arise from the different boundary conditions in *x* and *y* directions. This is only possible if graphene's TEC is much smaller than that of silicon, so that it effectively contracts relative to the trench during heating, and expands during cooling. In fact, a *negative* TEC is expected as a consequence of graphene's two-dimensionality, in which the energies of out-of-plane (bending) phonon modes is lower for smaller lattice parameters (in contrast to increasing phonon energy in bulk materials) [166]. Furthermore, during thermal cycling, the graphene membranes experience a competition between three forces: (1). F_{pin}, the substrate-pinning force that prevents the graphene membrane from sliding; (2) F_b, the bending/buckling critical compression force, which is generally << F_{pin}; and (3). $F_{stretch}$, the elastic restoring force under tension. A schematic of the process is shown in Fig. 2c. When *T* increases, the substrate and the trench width expand biaxially, while graphene *contracts*; this differential in TEC places the membrane in biaxial tension. Once $F_{stretch} > F_{pin}$, the taut membrane slides over the substrate into the trench, hence "erasing" any pre-existing ripples. Conversely, the cooling process applies *compressive* stress; since $F_b << F_{pin}$, the ends of the graphene remain pinned to the banks of the trench, resulting in transverse (*y*) ripples and/or longitudinal (*x*) buckling.

Such interplay between the thermal expansion of the substrate and the membrane suggest a simple way to control both the amplitude (or, if desired, the wavelength) and orientation of the ripples. Since the membranes buckle readily

under compression, the transverse compressive strain is $\Delta \sim \sqrt{1+\frac{\zeta^2}{\lambda^2}}-1$. Hence A and λ of the post-annealed wrinkles are related by

$$A \sim \lambda\sqrt{\Delta} \tag{4.5}$$

for $A<<\lambda$. Since Δ arises from the difference in TEC between the substrate and graphene, we expect Δ to scale with Θ_{max}, the maximum annealing temperature rise above ambient. This can be clearly seen in Fig. 7.8(a), in which the ripples' amplitudes become considerably more prominent after successive annealing to 425K and 475K, respectively.

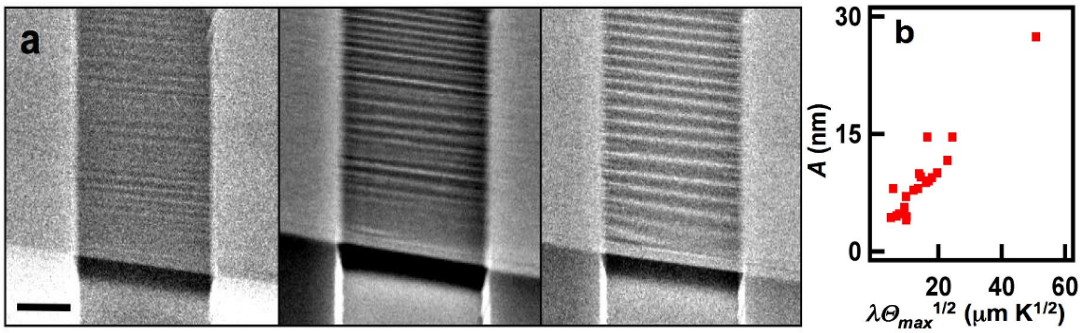

Fig. 7-8 Thermo-mechanical manipulation of amplitude and orientation of ripples. (a) SEM images of a membrane before annealing (left), after annealing to 425K (middle) and to 475K (right). Notice the increase in wavelength and amplitude of the ripples with annealing temperature. (b) *A vs.* $\lambda\Theta_{max}^{1/2}$ for post-annealed devices.

Fig. 7.8(b) plots A vs $\lambda\sqrt{\Theta_{max}}$ for 6 different devices, each thermally cycled to several different temperatures. Indeed, the data points fall approximately on a straight line. Thus, for a given set of boundary conditions, the wavelength and amplitude of the ripples can be controlled by Θ_{max}.

After annealing, all graphene membranes display more prominent ripples in the y-direction, and/or buckling in the *x*-direction (Fig. 7.9). Apart from membranes that buckle or sag towards the substrate (Fig. 7.7(b)), upward buckling is also observed (Fig. 7.9(d)). For graphene membranes that have been thermally cycled to high temperatures (>~600 K), some completely collapsed, settling onto the bottom of the trenches without breaking (Fig. 7.9 (a)-(c)).

Fig. 7.10 shows the morphological changes of graphene membranes through several thermal cycles via *in situ* SEM imaging in vacuum. Invariably, the graphene sheets become smoother (rippled) upon heating (cooling) with each cycle.

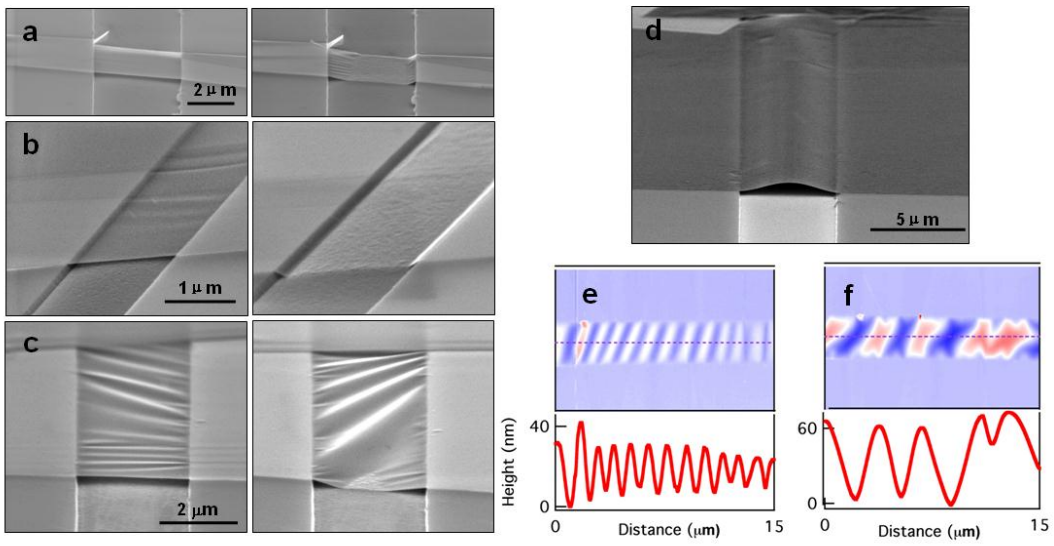

Fig. 7-9 (a), (b) and (c): SEM images of three graphene membranes before (left) and after annealing (right). (d) SEM image of a few-layer graphene membrane that buckles upwards after annealing. (e) an AFM image of a graphene membrane device before annealing (Upper panel: AFM topography image. Lower panel: Line trace along the dotted line in the upper panel.). (f) same as (a), after annealing to 550 K.

In addition to mechanical strains, thermal fluctuations may also induce ripples. However, numerical simulations [47, 167, 168] show that thermally induced ripples are random, dynamic, with amplitudes of ~ 1 Å at 300K. In contrast, the ripples in our devices are periodic, static, with amplitudes 1-3 orders of magnitude large than those predicted, thus are unlikely to arise from thermal fluctuations.

Another ripple-inducing mechanism is molecular adsorption, which has been shown theoretically to yield ripples in as-prepared, suspended graphene [168, 169]. However, for devices thermally cycled under vacuum, any desorbed molecular species are unlikely to adsorb on the graphene surface again. Thus, if molecular adsorption is the main rippling mechanism, the graphene sheet is not expected to exhibit further morphological changes after the first thermal cycle. This is incompatible with experimental data: Fig. 7.10 establishes the repeatability of the morphological changes through several thermal cycles. We therefore exclude molecular adsorption/desorption as the ripple formation mechanism in our experiments.

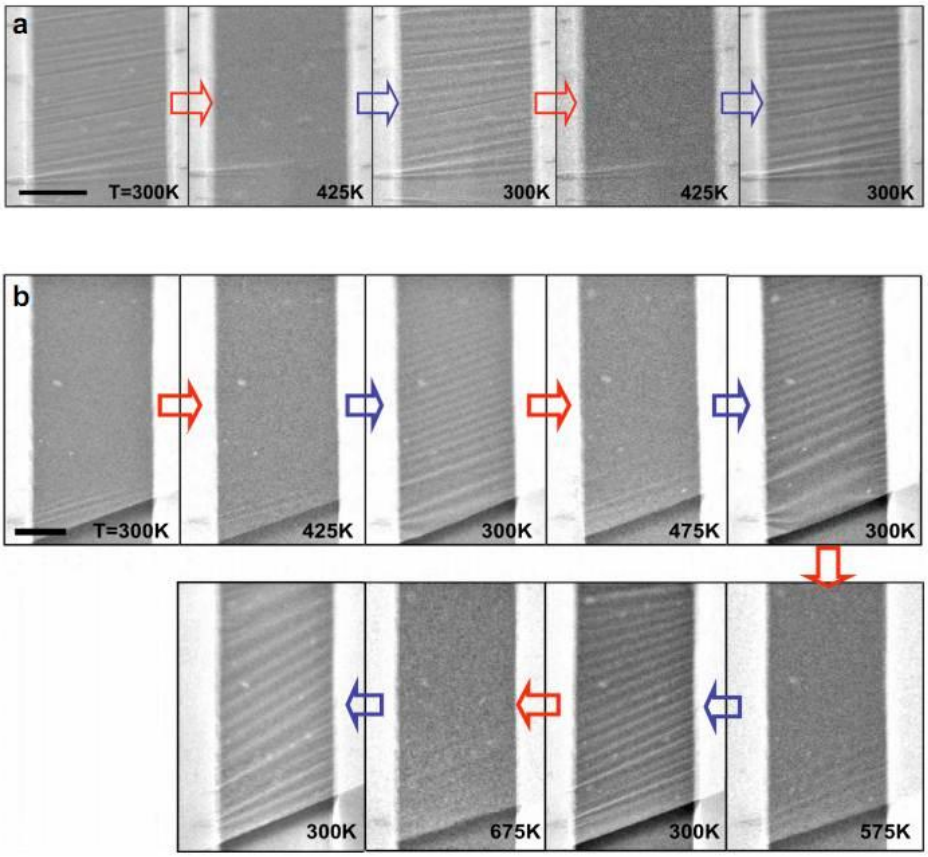

Fig. 7-10 *In situ* SEM imaging of graphene sheets through thermal cycles. Scale bars: 1 μm. (a) A bilayer graphene sheet with pre-existing ripples are thermally cycled between 300K and 675 K. (b) A single layer graphene sheet is relatively flat immediately after deposition. It is then thermal cycled to successively higher temperatures up to 575K.

To control the orientation of the ripples, we note that the ripple patterns are determined by the substrate-imposed boundary conditions (*e.g.* buckling *vs.* wrinkling in *x* and *y*-directions, respectively). This is similar to that in metallic thin films on elastomeric substrates that were patterned with relief structures [170]. In both experiments, ripples patterns, in which crests are aligned perpendicular to the step-like structures on the substrate, arise from the redistribution of compressive stresses due to the TEC differential between the substrate and the thin film. Hence,

as the first step towards controlled creation of 2D ripples, we pattern openings of different shapes on the substrates. Graphene membranes are suspended over these openings; annealing in temperature up to 700K yields striking patterns of 2D ripples, with the crests perpendicular to the edges of the opening (Fig. 7.11).

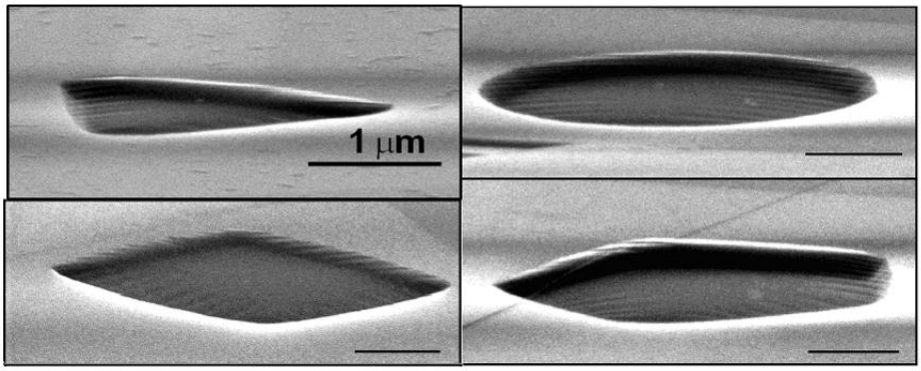

Fig. 7-11 Formation of periodic 2D ripples in graphene membranes suspended over openings of various shapes. Scale bars in all images are 1 μm.

These 1D or 2D ripple patterns may be desirable for novel devices such as in-plane electronic superlattices [171, 172]. In the long term, just as the creation of complex patterns was demonstrated in the metal/elastomer systems [170], simple thermal manipulation, coupled with pre-patterned relief structures on substrates, can be used to engineer graphene's local morphology, and alter its electronic properties. Such processes are also compatible with large-scale device applications.

7.4 Negative thermal expansion of suspended graphene

Our experimental system also enables us to explore the interplay between

graphene's mechanical, thermal and electrical properties. For instance, the thermo-mechanical manipulation of the ripples proves to be exceedingly effective, since graphene's *negative* TEC α accentuates the TEC-difference between the substrate and graphene. On the other hand, despite theoretical calculations and a debate over its temperature dependence [156, 172], $\alpha(T)$ has never been experimentally measured.

Our experiment readily enables measurement of the TEC $\alpha(T)$. To this end, we anneal a single-layer graphene sheet in a furnace up to 700K to create a sagging membrane. This device is then inserted into the SEM chamber, and heated up to ~450 K, at which the membrane is apparently taut across the trench. The heater is then turned off to allow the membrane to cool to 300K in 2 hours. We take a series of images to capture the sagging process. At a given temperature T, we compute the ratio $l(T)=L_g(T)/L_t(T)$, where L_g is the length of graphene membrane as measured along the arc, and L_t is the length of the trench measured along the chord (Fig. 7.12a inset). Both quantities are measured independently for every image to minimize errors induced by, *e.g.*, slight variations in the imaging conditions. Since the membrane's vertical displacement $\zeta \propto L_t\sqrt{l-1}$, even a miniscule deviation of l from unity produces notable changes in ζ that are readily detected in the SEM images.

In Fig. 7.12 we plot $l(T)$ for a single layer graphene sheet. The slope of the graph is the effective TEC of the graphene-trench system, and can be approximated by $\alpha_{eff} = \frac{dl}{dT} \approx \alpha - \alpha_t$, where α_t is the TEC of the trench, ~120% of that of Si, and a

detailed discussion is given below:

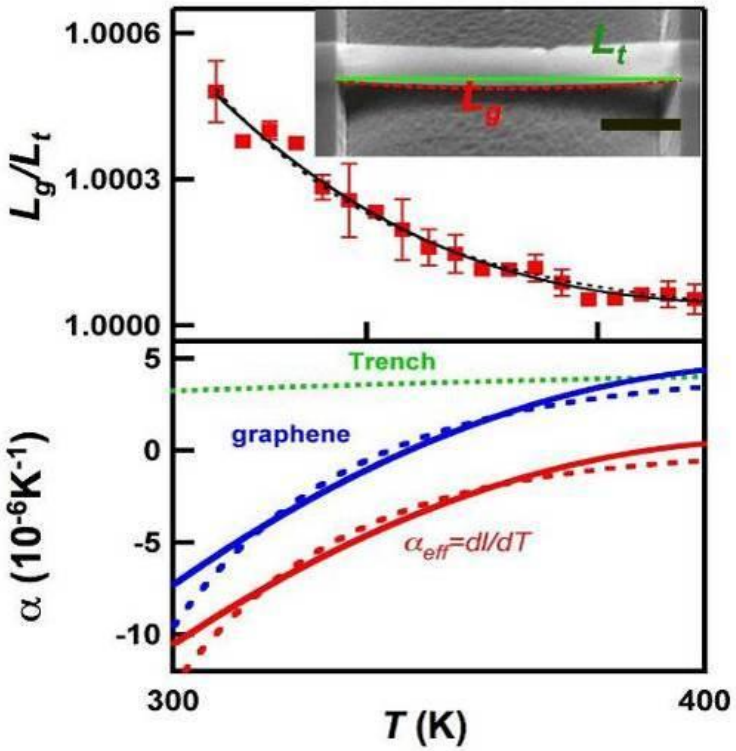

Fig. 7-12 TEC measurement of suspended graphene membranes. Upper Panel: *l(T)* for a single layer graphene membrane. We use two mathematical functions to approximate and interpolate the data: the solid line is a 4th-order polynomial fit to the data points, and the dotted line (almost indistinguishable) is an exponential function fit. The inset displays an SEM image of a sagging few-layer graphene sheet; scale bar: 1 μm. Lower Panel: Slope α_{eff} (red) and TEC (blue) of a single-layer graphene membrane. The solid and dotted lines correspond to results obtained using the polynomial and exponential functions, respectively. The trench's TEC is taken to be 120% of Si, and plotted as the green dotted line.

Graphene's TEC *(T)* is calculated from the slope of the curve *l(T)* $=L_g(T)/L_{trench}(T)$. The slope is given by:

$$b(T)=\frac{dl(T)}{dT}=\frac{1}{\Delta T}\left[\frac{L_g(T+\Delta T)}{L_t(T+\Delta T)}-\frac{L_g(T)}{L_t(T)}\right]$$
$$=\frac{1}{\Delta T}\left[\frac{L_g(T)\cdot(1+\alpha\Delta T)}{L_t(T)\cdot(1+\alpha_{sub}\Delta T)}-\frac{L_g(T)}{L_t(T)}\right]\approx\frac{L_g(T)}{L_t(T)}\left(\alpha-\alpha_{sub}\right),$$

if we take first order expansions, assuming $\alpha\Delta T<<1$. Here α and α_{sub} are the thermal expansion coefficients of graphene and substrate, respectively. Since the prefactor $L_g(T)/L_t(T)$ is within 0.1% of unity, $b \approx \alpha-\alpha_{sub}$ or

$$\alpha \approx b+\alpha_{sub}. \tag{4.6}$$

To determine α, we substitute $\alpha_{sub}\approx 1.25\alpha_{\mathrm{Si}}$ into Eq. (4.6), since thermal expansion of the trench is mainly determined by the underlying Si substrate (rather than the thin SiO_2 layer) – to the first order, the thermal expansion of the trench is mainly determined by the underlying Si substrate, which is 1700 times thicker and twice as stiff as the SiO_2 layer. A more careful consideration indicates that the presence of the thin SiO_2 layer with a smaller TEC may give rise to two different effects that may modify the trenches' TEC.

(a). Upon a temperature increase ΔT, The difference in TEC between the substrate and the thin oxide gives rise to an interfacial thermal stress; as a result, the substrate is strained and acquires a finite curvature. This phenomenon is qualitatively similar to, although much smaller in magnitude, that observed during the thermal expansion of a bi-metallic strip. The strain and radius of curvature R can be estimated using the well-known Stoney formula [173] for a thin-film-on-substrate system, given by

$$\varepsilon = -\frac{\sigma_f d_f (1-\nu_s)}{E_s d_s} \quad \text{and} \qquad R = \frac{E_s d_s^{\,2}}{6\sigma_f d_f (1-\nu_s)}$$

where $\sigma_f = \frac{(\alpha_s - \alpha_f)\Delta T\, E_f}{(1-\nu_f)}$ is the thermal stress in the oxide. Here α is the TEC, d is the thickness, ΔT is the temperature increase, ν is the Poisson's ratio, E is the elastic constant, and the subscripts f and s indicate thin film and substrate, respectively. Using d_s=500 μm, d_f=300 nm, and standard values α_{Si}~3x10^{-6} K^{-1}, α_{SiO2}~5x10^{-7} K^{-1}, E_{Si}≈160 GPa, E_{SiO2}≈70 GPa, ν_{Si}≈0.22 and ν_{SiO2}≈0.16, we estimate σ_f≈62.5 MPa, R~450m, and ε≈-2x10^{-7}. Thus, *within an accuracy of 1 part per million*, the expansion of Si is unaffected by the oxide layer.

(b). A second, and more prominent, factor is the free edge effect – while the bottom of the SiO_2 is bonded to and expands as much as silicon, the top layer is free and expands at a smaller rate; thus, the walls of a trench are no longer vertical but slant outwards. In fact, if the expansion of the top of the thin film is independent of that of the bottom, and if the thin film is perfectly incompressible, the trench length as measured from the top will be increased by $(2\alpha_{sub}-\alpha_f)\Delta T$. To quantify this effect, we use COMSOL, a finite element analysis software, to simulate our experimental situation. Our results show that the thermal expansion of the trench is roughly 125% that of bare silicon, which is reasonable considering the small thickness and Poisson's ratio of SiO_2.

To obtain α_{eff}, the data points are interpolated by an analytical function, which is then differentiated. Two different fitting functions are used to illustrate the error

range of this procedure. Using values of $\alpha_{Si}(T)$ from ref. , we can determine $\alpha(T)$ for graphene (lower panel of Fig. 7.12, blue lines). We find that at 300K, $\alpha \sim -7\text{x}10^{-6}$ K^{-1}, which indeed greatly exceeds than the in-plane TEC of graphite, $\sim -1\text{x}10^{-6}$ K^{-1}; its magnitude decreases with increasing *T*. On the other hand, the measured α is roughly twice that from theoretical calculation, and approaches zero more quickly than expected [156]. Though more experimental and theoretical works are warranted to resolve such discrepancies, our first quantitative measurement of graphene's TEC provides important insight into graphene's unique thermal properties.

This result has important implications towards controlling thermally induced stress in graphene electronics, as the difference in TECs between the substrate and thin film is the most common mechanism that give rise to stress and even cracks in devices. It is also important for understanding the transport and mechanical properties of suspended graphene devices. For instance, because of its anomalously large and negative TEC, a flat, suspended graphene sheet almost invariably become rippled after annealing, or after cooling by 100-200 K. This may account for the disappearance of quantum Hall features in suspended graphene devices after annealing, and the unusual *G(T)* behaviour with large sample-to-sample variations reported in ref. [146].

Chapter 8. Gating effect of suspended graphene devices

Although transport measurements have been performed in suspended graphene (SG) devices for years [24, 25, 92, 129], direct observation of morphology for SG at external electrical field or low temperature still remains undetected. In this chapter we will first discuss the buckling of suspended graphene sheets when applying a V_g to the back gate. Such a gating effect could also modify the morphology of ripples in suspended graphene.

At low temperature, due to graphene's negative thermal expansion, suspended graphene is rippled and buckled with features that resembles "butterfly" forming at two free edges, therefore suspended graphene contacts the bottom of trench more easily when V_g is applied at low temperature. The above observation has important applications for strain and charge density engineering in SG, and these results may also indicate the necessity to effectively manipulate both charge density and strain in SG devices.

8.1 Introduction

In previous chapters we have already demonstrated that suspended graphene (SG) membrane is an ideal platform that enables the investigation of its properties free of interaction with substrates. For instance, SG exhibits extraordinary mechanical properties [28, 30], large thermal conductivity [26, 174], ultra-high mobility [24, 25] that enables the observation of fractional quantum Hall effect [94, 95], and it is also an ideal material for an electromechanical oscillator or resonator [28]. In fact, all of these important properties could be related to and affected by the morphology of SG, in which strains or ripples [52, 53] could induce an effective magnetic field and strongly affect the transport properties of SG [148-153].

A simple and direct method to strain and buckle graphene is to apply a back gate to SG sheet since a gate-created electrostatic force could induce a deflection of graphene [175]. Thermal manipulation can also effectively affect SG's morphology as discussed in the last chapter. In the following we first report a successful manipulation of graphene's morphology via electrostatic and thermal control.

8.2 Device fabrication

SG sheets are prepared by mechanical exfoliation of Kish graphite onto Si/SiO_2 (300nm) wafers with pre-patterned trenches (250nm in depth and ~3 μm in width) as shown in Fig. 8.1(a). The trenches are defined by photolithography followed by plasma etching in a reactive ion etcher (RIE) system. The number of graphene layers

is identified by color contrast under an optical microscope and then confirmed by Raman spectroscopy. We directly deposit Ti/Au metal electrodes through shadow masks that are carefully aligned to selected graphene sheets. By grounding one of the electrodes and applying a gate voltage V_g, we can maintain an electrostatic potential and hence an attractive force between SG and Si substrate. The structure of such a device is different from hydrogen fluoride etched SG devices [24, 25], since two ends of the SG sheet are supported by SiO_2 banks instead of attaching to the bottom of partially suspended electrodes, therefore excluding the influence of bending of suspended electrodes when applying back gate V_g.

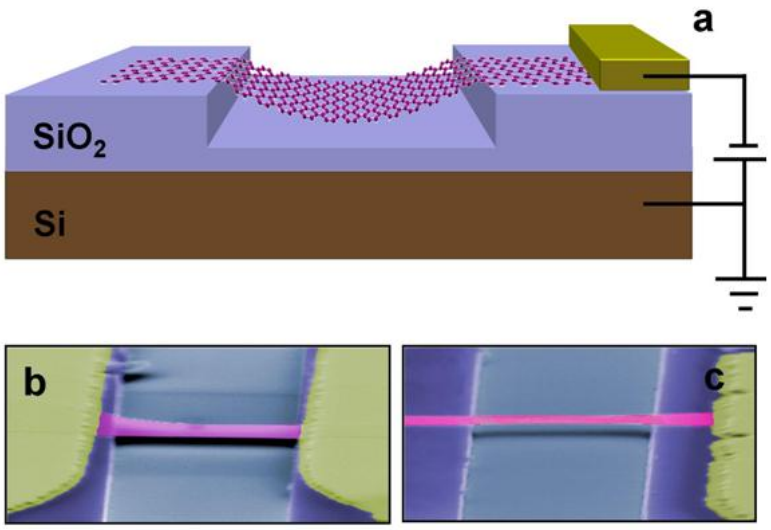

Fig. 8-1 (a) Schematic diagram of applying a gate voltage V_g to a suspended graphene device. (b) and (c) SEM images of doubly clamped and non-clamped SG devices, respectively.

After considering the sliding effect between the graphene and substrate [30, 52], we fabricated two types of SG devices: 1) SG sheet is clamped by two parallel metal

contacts which are deposited at the edges of trench, as shown in Fig. 8.1(b). 2) SG sheet is non-clamped and only the ends of the graphene sheet are connected by metal contacts which are greater than 10μm away from the edge of the trench, as shown in Fig. 8.1(c). For both types of devices, narrow and rectangular-shaped SG sheets with widths less than 1μm are selected for device fabrication.

8.3 Gating effect of suspended graphene devices

Applying V_g to SG sheet could induce a deflection of graphene [175] due to the created electrostatic force. To experimentally explore this effect we perform *in situ* scanning electron microscope (SEM) imaging for profiles of devices described above on a tilted stage, while continuously varying V_g. In Fig. 8.2 a series of SEM images taken at 85^o tilted angle show the morphology change of a single layer SG sheet (non-clamped) in response to applied V_g.

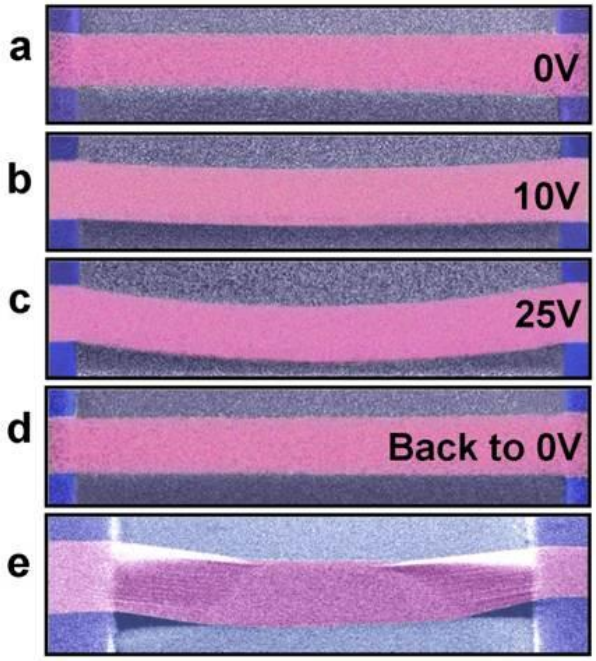

Fig. 8-2 SEM images of a SG device at different electrical fields created by back gate voltage.

As V_g increases, the SG sheet gradually buckles downward to the bottom of trench. As long as the buckling is elastic, the strain could be released to allow the SG to return to the taut state by removing the V_g. Neither sagging nor deformation of SG is observed after sweeping V_g back to zero even after multiple cycles of V_g sweeping, indicating such a buckling is largely reversible. The out-of-plane deformation h can also be readily estimated in such an SEM image and more analysis will be discussed in details later. Here h is calculated using measured arc length l_1 assuming the deformation is nearly parabolic.

$$h = l_0\sqrt{\frac{3}{8}(\frac{l_1}{l_0}-1)}\,, \tag{8.1}$$

where l_0 is the width the trench.

However, when V_g is sufficiently large and once the SG sheet is pulled down far enough to contact the bottom of trench, the SG sheet becomes irreversibly collapsed due to the Van der Waals force even after V_g is removed, as shown in Fig. 8.2(e). We also note that the sufficiently strong Van der Waals force in the collapsed region could induce strain in regions that remain suspended, therefore creating ripples [52].

Since such a deflection of SG arises from the attraction of opposite electrostatic charges between the SG and back gate, the attractive force could be described by:

$$F = \frac{\varepsilon_0\varepsilon^2 V_g{}^2 S}{2(\varepsilon d_0 + \varepsilon_0 d_1)^2} \tag{8.2}$$

where S is the area of SG, ε_0 is the permittivity of vacuum, ε is the permittivity of

SiO_2, e is the charge of an electron, d_0 =250nm is the depth of trench and d_1 =50nm is the thickness of the residual SiO_2 on the bottom of trench. A theoretical calculation has been investigated [175] in a model similar to our SG devices which considers that a uniform load of electrostatic force is applied to the SG sheet. The resultant out-of-plane deformation $h(V_g)$ (as indicated in the inset of Fig. 8.3a) for single layer graphene is hence plotted in Fig. 8.3(a) (dotted line) by setting geometries of the model equivalent to our devices. However, such assumption of uniform load no longer holds when the buckling of SG is comparable to the separation between the SG and Si substrate. Therefore, we consider a modified model that includes the buckling-induced, non-uniform charge distribution in SG. This modified model is simulated by COMSOL Multiphysics in this work and the corresponding result is plotted in Fig. 8.3(a) as solid line for single layer graphene.

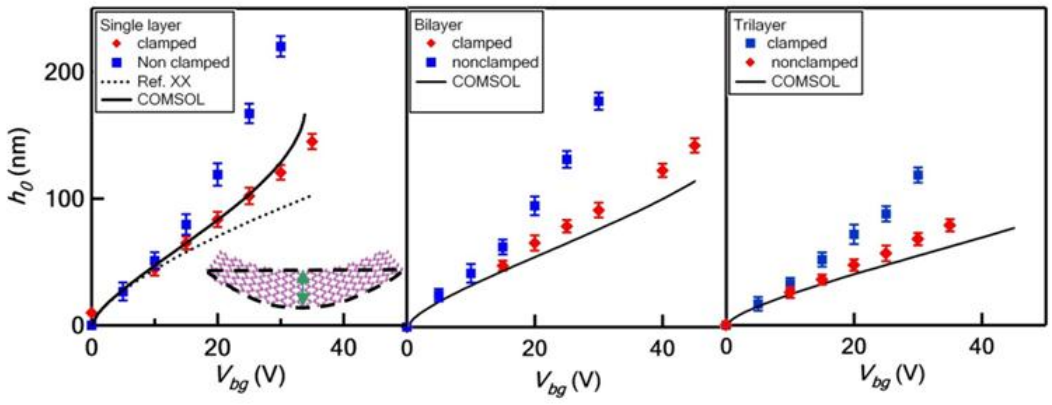

Fig. 8-3 (a)-(c): Out-of-plane deformation $h(V_g)$ for single layer, bilayer and trilayer SG, respectively.

To compare the above models with experimental results we also plot $h(V_g)$ of

single layer graphene for both clamped and non-clamped devices, and for each V_g, h is extracted and averaged from several *in-situ* SEM images. The results of *in-situ* measurement shown in Fig 3a indicate that the clamped SG device agrees well with the COMSOL simulation for single layer. However, for bilayer and trilayer SG (Fig 4.15 b and c), the results deviate slightly from the COMSOL simulation, which could be attributed to the incomplete clamping of SG (SG could possibly slide between the metal and substrate interface) or other systematic errors such as simply assuming that Young's modulus of bilayer (trilayer) graphene is double (triple) that of single layer graphene. Nonetheless, we notice that for all SG with different numbers of layers, the deflection of non-clamped devices is obviously larger than that of clamped devices.

The above observations could be schematically explained in Fig. 8.4: when $F_{strain} > F_{pin}$ (where F_{strain} is the force induced by strain in SG from electrostatic attraction and F_{pin} is the substrate-pinning force that prevents the graphene sheet from sliding), the substrate-supported part of graphene slides into the trench and hence increases the value of h. While after gate voltage is removed, F_{strain} can possibly pull this part back to substrate, therefore no obvious slacking is observed after V_g is cycled to zero. Future works of similar experiments might enable us to study the layer dependence and substrate dependence of friction between graphene and substrate.

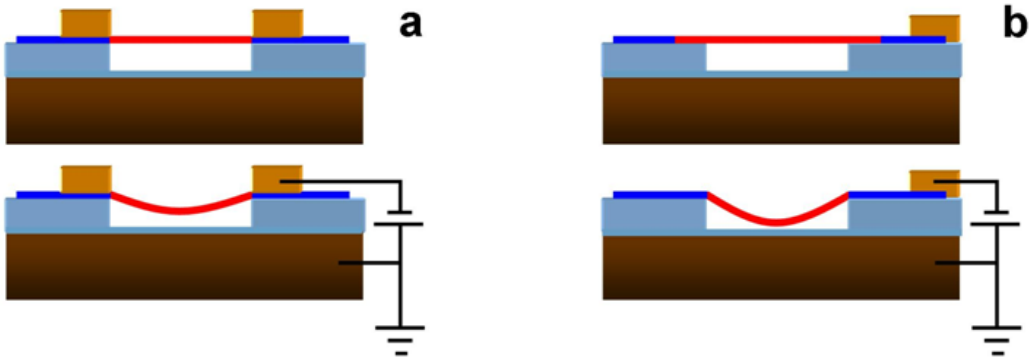

Fig. 8-4 Schematic illustration of graphene buckling in (a) clamped SG devices and possible sliding in (b) non-clamped SG devices

The non-uniformity of charge density and strain distribution in buckled SG can also be simulated by COMSOL and results are shown in Fig. 8.5. It is apparent that both charge density and strain increase with increasing V_g, and their non-uniformities become significant at large buckling. Simulation results also suggest that at large buc()kling, the charge density reaches its maximum at the center of the buckled SG sheet, while the strain is maximum at the two edges of the buckled SG.

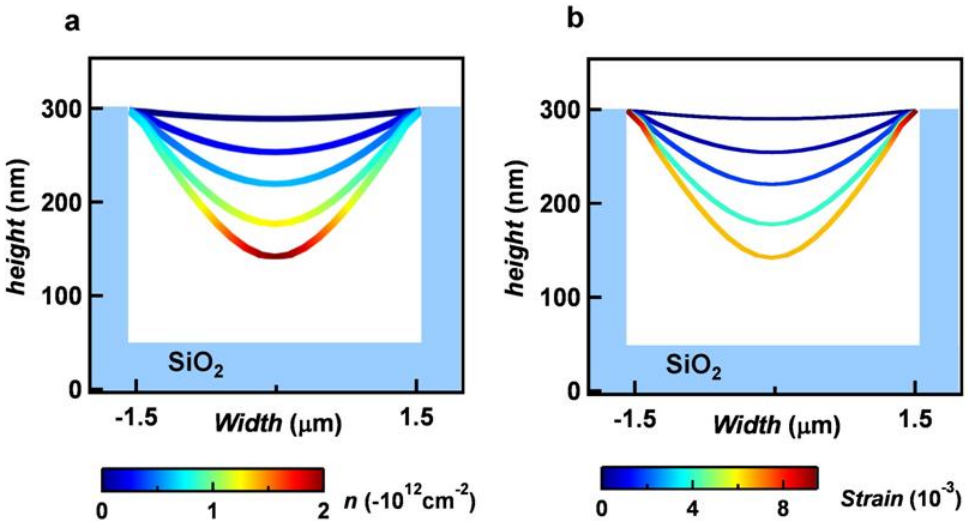

Fig. 8-5 Non-uniformity of (a) charge density and (b) strain distribution in buckled SG (from top to bottom: V_{bg}=1, 10, 20, 30, 33.8V)

These results may now indicate that, instead of assuming uniform charge density and zero strain in transport measurements (as one typically does), one may need also to consider the non-uniform charge density and strain distribution under applied V_g in order to account for the data.

8.4 Combination of rippling, cooling and gating effects

Another important morphological feature in SG is its rippling effect. It has already been demonstrated that both tensile and compressive strains can create periodic ripples in SG [52], which are predicted to strongly influence the electronic properties of graphene [148-153]. Therefore, we now study the gating effect on SG with strain-induced ripples.

In Fig. 8.6 (a) - (c), we show that when V_g is applied to a SG sheet with oblique ripples, not only is the whole SG sheet buckled, but also the wavelength of ripples becomes altered. Such a phenomenon is expected from the classical elasticity theory with a result [52, 159]: $\lambda^4 \sim \gamma^{-1}$, where λ is the wavelength of ripples and the γ is the longitudinal tensile strain. Therefore the gating effect can increase γ which consequently decreases λ. In this case we estimate that the strain is $\sim 6 \times 10^{-4}$ at V_g = 30V.

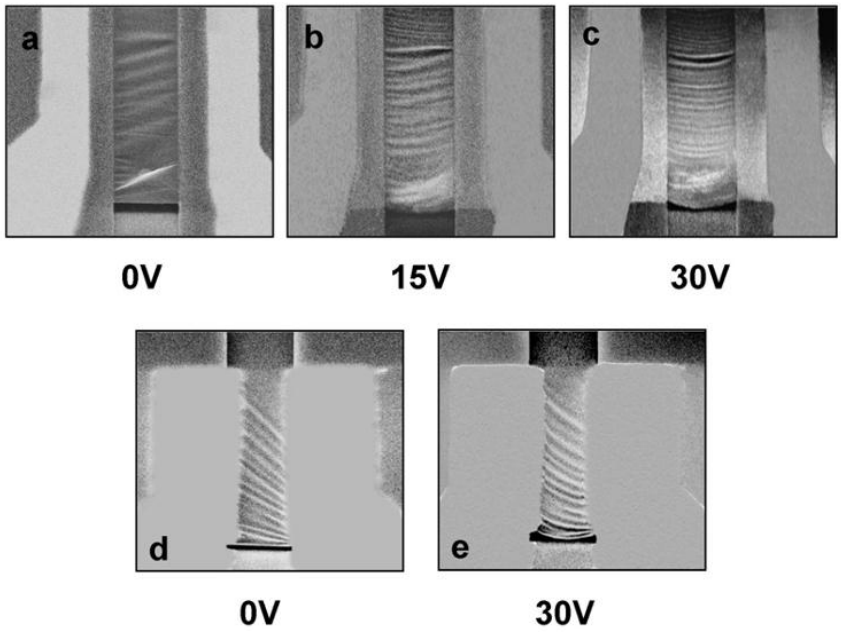

Fig. 8-6 SEM images of (a)-(c): partially clamped SG sheet with oblique ripples at different V_g. (d)-(e): fully clamped SG sheet with oblique ripples at different V_g.

Meanwhile, the gating effect also changes the orientation of the ripples from oblique to perpendicular to the edges of trench, which could be explained by sliding of the substrate-supported region of graphene. However, when metal contacts extend

onto the suspended portion of graphene, as shown in Fig. 8.6 d-e, the gating effect no longer manipulates the morphology of ripples; therefore the ripples in SG could be "frozen" by certain boundary conditions.

Finally we note that although low temperature transport measurements have been performed in SG devices for years [24, 25, 92, 129], direct observation of morphology for SG at low temperature has not been reported. Therefore now we focus on the cooling effect on SG membranes. Using an SEM cold stage, we perform *in situ* SEM imaging for relatively wide (aspect ratio ~1) SG sheets at room temperature and at 100K.

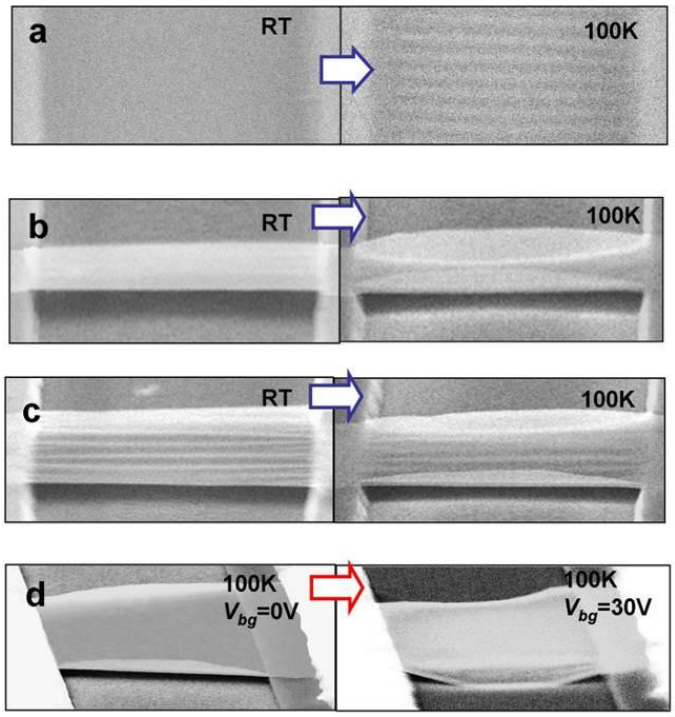

Fig. 8-7 (a)-(c): In-situ SEM images of SG devices at room temperature (left panels) and 100K (right panels). (d): At 100K, SEM images of SG at different V_g.

Fig. 8.7(a) shows that ripples appear at 100K in SG sheet which is taut at room

temperature (RT). This process could be understood in terms of graphene's negative thermal expansion coefficient (TEC), which induces a compressive stress due to the clamped edges of SG and results in the formation of ripples. The expansion due to graphene's negative TEC can also induce the upward buckling of SG's two free sides, forming a "butterfly" feature at two sides of SG, as shown in Fig 4.19(b) and (c). This observation readily enables us to measure the lower bound of the TEC by measuring the length along the arc of the "butterfly" feature. We estimate that the average TEC between 100K and room temperature is up to 2×10^{-5} (no unit for thermal expansion coefficient) for single layer graphene and 4×10^{-5} for multilayer graphene, which are much larger than the theoretical expectation [156-158]. The mechanism of such an anomalous result is still unclear and more experiments are necessary for confirmation. At last, we combine both gating and cooling effect on SG, as shown in Fig. 8.7(d). The expanded "butterfly" feature could be easily pulled to the bottom of the trench when applying a V_g, though SG may still be suspended under similar V_g at room temperature. Therefore SG is easier to collapse at low temperature.

To conclude, we observe a buckling of SG when applying a V_g to the back gate, and such a gating effect could also modify the morphology of ripples in SG. At low temperature, due to its negative TEC, SG is observed to be rippled at the center and "flares" up at the free edges; therefore SG is more prone to collapse by applying V_g at low temperatures. The above observation has important implications for strain

engineering in SG and understanding transport data of suspended graphene devices at low temperatures.

Chapter 9. Conclusion

To conclude, this thesis explored the electrical and mechanical properties of a new 2-D atomic thick crystal – graphene. Chapter 1 included an overview of the basic concepts of electrical transport and mechanical properties of nano-scale material, together with a brief introduction of graphene relevant to the experimental results presented in this thesis. In Chapter 2 we describe fabrication techniques of graphene devices, in which the innovative shadow mask fabrication method is the key to this thesis since most exciting results are produced by ultra-clean graphene devices fabricated by this lithography-free method.

The electrical measurement section begins in Chapter 3. When graphene is coupled to superconducting electrodes such as aluminum, we observed both multiple Andreev reflections and bi-polar supercurrent in such graphene Josephson junctions. We also observed depression of critical current I_c and the strong dependence of I_cR_n on charge density, which can be explained by premature switching in underdamped Josephson junctions described by RCSJ model. This demonstrates that thermal fluctuation plays an important role in electronic transport of graphene Josephson junctions. However, an intended goal of the project, trying to observe specular Andreev reflection, was not achieved. This is because specular Andreev reflection mainly takes place when the Fermi level is within the energy gap of the superconductor, thus a very sharp Dirac point is required. We expect that specular Andreev reflection can be observed in the near future if we can couple

superconducting electrodes to suspended graphene with high mobility.

Then in Chapter 4 we focus on quantum Hall effect in suspended BLG and TLG. Applying shadow mask technique we successfully fabricated devices with ultra-high mobilities. For bilayer devices, we observe conductance minima at all integer filling factors ν between 0 and -8, as well as a small plateau at ν=1/3. For trilayer devices, we observe features at ν=-1, -2, -3 and -4, and at ν~0.5 that persist to 4.5K at B=8T. These features persist for all accessible values of n and B, and suggest the onset of symmetry breaking and/or FQH states in these devices. Besides we also observed that some well-developed quantum Hall (QH) plateaus in r-TLG split into 3 branches at higher fields. Such splitting is a signature of Lifshitz transition, a topological change in the Fermi surface, which is found only in BLG and r-TLG till now.

At high magnetic field, graphene devices with high qualities (including SLG, BLG and TLG) always show insulating state at the Dirac point, however in some BLG/TLG devices we observe a zero field insulating state which has never been observed or predict by single particle calculation. Therefore we went on to study the low temperature transport behavior of minimum conductivity of both BLG and TLG at zero fields. In chapter 5 we report on a systematic study of the minimum conductivity σ_{min} in a large number of single-gated and double-gated BLG samples. We find a surprisingly constant σ_{min} value ~ 2-3 e^2/h for the majority of devices, independent of device mobility and the presence or absence of substrates. However, the best devices manifest an insulating state with an energy gap ~ 2-3 meV. We

observe a phase transition between the single-particle metallic state and the interaction-induced insulating state in ultra-clean BLG, which can be tuned by temperature, disorder, charge density n and perpendicular electric field $E_{\perp}$.

In chapter 6 we extended this work on to trilayer graphene, we demonstrate the dramatically different transport properties in TLG with different stacking orders, and the unexpected spontaneous gap opening in charge neutral r-TLG. At the Dirac point, B-TLG remains conductive while r-TLG becomes insulating with an intrinsic interaction-driven gap ~6 meV. Our results underscore the rich interaction-induced phenomena in trilayer graphene with different stacking orders, and its potential towards future gapped graphene applications.

An experimental study of the mechanical properties of suspended graphene membrane began in Chapter 7. We demonstrate that we are able to control ripple orientation, wavelength and amplitude by controlling boundary conditions and exploiting graphene's negative thermal expansion coefficient, which we measure to be much larger than that of graphite. By elucidating the ripple formation process, which can be understood in terms of classical thin-film elasticity theory, our results should lead to a better understanding of suspended graphene devices, controlled engineering of thermal stress in large scale graphene electronics, and enabling a systematic investigation of the effect of ripples on the electronic properties of graphene. At last in Chapter 8 we observe a buckling of SG when applying a V_g to the back gate, and such a gating effect could also modify the morphology of ripples in SG. At low

temperature, due to its negative TEC, SG is observed to be rippled and buckled at two free edges.

Our results have contributed to the graphene field for fundamental understanding of both electrical and mechanical properties of graphene. However, there are still many new and interesting unsolved problems to address, such as experimental observation of specular Andreev reflection in graphene, mechanism of insulating states in BLG and r-TLG, how ripples affect graphene's transport properties, and layer dependence of graphene's CTE. I believe this thesis just touched the surface of what is possible within this new and exciting material, and hopefully a lot more can be explored by more scientists and engineers in this unique and wonderful material.

References

[1] K.S. Novoselov, A.K. Geim, S.V. Morozov, D. Jiang, M.I. Katsnelson, I.V. Grigorieva, S.V. Dubonos, A.A. Firsov, Two-dimensional gas of massless Dirac fermions in graphene, Nature, 438 (2005) 197-200.

[2] Y.B. Zhang, Y.W. Tan, H.L. Stormer, P. Kim, Experimental observation of the quantum Hall effect and Berry's phase in graphene, Nature, 438 (2005) 201-204.

[3] W.T. Sommer, Liquid Helium as a Barrier to Electrons, Physical Review Letters, 12 (1964) 271-273.

[4] K.S. Novoselov, Z. Jiang, Y. Zhang, S.V. Morozov, H.L. Stormer, U. Zeitler, J.C. Maan, G.S. Boebinger, P. Kim, A.K. Geim, Room-temperature quantum hall effect in graphene, Science, 315 (2007) 1379-1379.

[5] K.S. Novoselov, A.K. Geim, S.V. Morozov, D. Jiang, Y. Zhang, S.V. Dubonos, I.V. Grigorieva, A.A. Firsov, Electric field effect in atomically thin carbon films, Science, 306 (2004) 666-669.

[6] S. Iijima, T. Ichihashi, SINGLE-SHELL CARBON NANOTUBES OF 1-NM DIAMETER, Nature, 363 (1993) 603-605.

[7] A. Bezryadin, C.N. Lau, M. Tinkham, Quantum suppression of superconductivity in ultrathin nanowires, Nature, 404 (2000) 971-974.

[8] J.L. Costa-Kramer, N. Garcia, P. Garcia-Mochales, P.A. Serena, M.I. Marques, A. Correia, Conductance quantization in nanowires formed between micro and

macroscope metallic electrodes, Phys. Rev. B, 55 (1997) 5416.

[9] M. Tinkham, Limits on superconductivity in nanoparticles and nanowires, Journal Of Superconductivity, 13 (2000) 801-804.

[10] M. Huang, S. Mao, H. Feick, H. Yan, Y. Wu, H. Kind, E. Weber, R. Russo, S. P. Yang, Room-temperature ultraviolet nanowire nanolasers, Science, 292 (2001) 1897.

[11] M.S. Gudiksen, L.J. Lauhon, J. Wang, D.C. Smith, C.M. Lieber, Growth of nanowire superlattice structures for nanoscale photonics and electronics, Nature, 415 (2002) 617-620.

[12] C.W.J. Beenakker, H. van Houten, Resonant Josephson Current through a Quantum Dot, in: H. Koch, H. Lubbig (Eds.) Single Electron Tunneling and Mesoscopic Devices, Springer, Berlin, 1992, pp. 175-179.

[13] C.P. Collier, R.J. Saykally, J.J. Shiang, S.E. Henrichs, J.R. Heath, Reversible tuning of silver quantum dot monolayers through the metal-insulator transition, Science, 277 (1997) 1978.

[14] L.P. Kouwenhoven, C.M. Marcus, P.L. McEuen, S. Tarucha, R.M. Westervelt, S. Wingreen, Electron Transport in Quantum Dots, in: L.L. Sohn, L.P. Kouwenhoven, G. Schon (Eds.) Mesoscopic Electron Transport, Springer, Kluwer, 1997.

[15] R. Schuster, E. Buks, M. Heiblum, D. Mahalu, V. Umansky, H. Shtrikman, Phase measurement in a quantum dot via a double-slit interference experiment,

Nature, 385 (1997) 417-420.

[16] K. Kang, Kondo resonance, Coulomb blockade, and Andreev transport through a quantum dot, Physical Review B (Condensed Matter and Materials Physics), 58 (1998) 9641-9643.

[17] T.I. Ivanov, Low-temperature transport through a quantum dot coupled to two superconducting leads, Physical Review B (Condensed Matter and Materials Physics), 59 (1999) 169-172.

[18] K.v. Klitzing, G. Dorda, M. Pepper, New Method for High-Accuracy Determination of the Fine-Structure Constant Based on Quantized Hall Resistance, Physical Review Letters, 45 (1980) 494-497.

[19] J.K. Jain, S.A. Kivelson, QUANTUM HALL-EFFECT IN QUASI ONE-DIMENSIONAL SYSTEMS - RESISTANCE FLUCTUATIONS AND BREAKDOWN, Physical Review Letters, 60 (1988) 1542-1545.

[20] B.J. van Wees, E.M.M. Willems, C.J.P. Harmans, C.W.J. Beenakker, H. van Houten, J.G. Williamson, C.T. Foxton, J.J. Harris, Anomalous Integer Quantum Hall Effect in the Ballistic Regime with Quantum Point Contacts, Phys. Rev. Lett., 62 (1989) 1181.

[21] S. Datta, Electronic transport in mesoscopic systems, Cambridge Studies in Semiconductor Physics and Microelectronic Engineering, 1997.

[22] K.S. Novoselov, D. Jiang, F. Schedin, T.J. Booth, V.V. Khotkevich, S.V. Morozov, A.K. Geim, Two-dimensional atomic crystals, Proc. Natl. Acad. Sci.

U. S. A., 102 (2005) 10451-10453.

[23] A.K. Geim, K.S. Novoselov, The rise of graphene, Nat. Mater., 6 (2007) 183-191.

[24] K.I. Bolotin, K.J. Sikes, Z. Jiang, M. Klima, G. Fudenberg, J. Hone, P. Kim, H.L. Stormer, Ultrahigh electron mobility in suspended graphene, Sol. State Commun., 146 (2008) 351-355.

[25] X. Du, I. Skachko, A. Barker, E.Y. Andrei, Approaching ballistic transport in suspended graphene, Nat. Nanotechnol., 3 (2008) 491-495.

[26] A.A. Balandin, S. Ghosh, W. Bao, I. Calizo, D. Teweldebrhan, F. Miao, C.N. Lau, Superior Thermal Conductivity of Single-Layer Graphene, Nano Lett., 8 (2008) 902.

[27] I.W. Frank, D.M. Tanenbaum, A.M. Van der Zande, P.L. McEuen, Mechanical properties of suspended graphene sheets, Journal Of Vacuum Science & Technology B, 25 (2007) 2558-2561.

[28] J.S. Bunch, A.M. van der Zande, S.S. Verbridge, I.W. Frank, D.M. Tanenbaum, J.M. Parpia, H.G. Craighead, P.L. McEuen, Electromechanical resonators from graphene sheets, Science, 315 (2007) 490-493.

[29] J.S. Bunch, S.S. Verbridge, J.S. Alden, A.M. van der Zande, J.M. Parpia, H.G. Craighead, P.L. McEuen, Impermeable atomic membranes from graphene sheets, Nano Letters, 8 (2008) 2458-2462.

[30] C. Lee, X.D. Wei, J.W. Kysar, J. Hone, Measurement of the elastic properties

and intrinsic strength of monolayer graphene, Science, 321 (2008) 385-388.

[31] A.C. Ferrari, J.C. Meyer, V. Scardaci, C. Casiraghi, M. Lazzeri, F. Mauri, S. Piscanec, D. Jiang, K.S. Novoselov, S. Roth, A.K. Geim, Raman spectrum of graphene and graphene layers, Phys. Rev. Lett., 97 (2006) 187401.

[32] C. Casiraghi, S. Pisana, K.S. Novoselov, A.K. Geim, A.C. Ferrari, Raman fingerprint of charged impurities in graphene, Applied Physics Letters, 91 (2007) 233108.

[33] F. Wang, Y.B. Zhang, C.S. Tian, C. Girit, A. Zettl, M. Crommie, Y.R. Shen, Gate-variable optical transitions in graphene, Science, 320 (2008) 206-209.

[34] J. Yan, Y.B. Zhang, P. Kim, A. Pinczuk, Electric field effect tuning of electron-phonon coupling in graphene, Physical Review Letters, 98 (2007).

[35] B.D.A. Daniel R. Cooper, Nageswara Ghattamaneni, Benjamin Harack, Michael Hilke, Alexandre Horth, Norberto Majlis, Mathieu Massicotte, Leron Vandsburger, Eric Whiteway, Victor Yu, Experimental review of graphene, in, arXiv:1110.6557v1, 2011.

[36] M.I. Katsnelson, K.S. Novoselov, A.K. Geim, Chiral tunnelling and the Klein paradox in graphene, Nat. Phys., 2 (2006) 620-625.

[37] A.V. Shytov, M.S. Rudner, L.S. Levitov, Klein Backscattering and Fabry-Perot Interference in Graphene Heterojunctions, Phys. Rev. Lett., 101 (2008) 156804.

[38] N. Stander, B. Huard, D. Goldhaber-Gordon, Evidence for Klein Tunneling in Graphene p-n Junctions", Phys. Rev. Lett., 102 (2009) 026807.

[39] S. Das Sarma, S. Adam, E.H. Hwang, E. Rossi, Electronic transport in two dimensional graphene, Rev. Mod. Phys., 83 (2011) 407.

[40] A.H. Castro Neto, F. Guinea, N.M.R. Peres, K.S. Novoselov, A.K. Geim, The electronic properties of graphene, Rev. Mod. Phys., 81 (2009) 109-162.

[41] F. Guinea, A.H. Castro Neto, N.M.R. Peres, Electronic states and Landau levels in graphene stacks, Phys. Rev. B, 73 (2006) 245426.

[42] M. Aoki, H. Amawashi, Dependence of band structures on stacking and field in layered graphene, Sol. State Commun., 142 (2007) 123-127.

[43] M.F. Craciun, S. Russo, M. Yamamoto, J.B. Oostinga, A.F. Morpurgo, S. Thrucha, Trilayer graphene is a semimetal with a gate-tunable band overlap, Nature Nanotechnol., 4 (2009) 383-388.

[44] F. Zhang, B. Sahu, H.K. Min, A.H. MacDonald, Band structure of ABC-stacked graphene trilayers, Phys. Rev. B, 82 (2010) 035409.

[45] D. Garcia-Sanchez, A.M. van der Zande, A.S. Paulo, B. Lassagne, P.L. McEuen, A. Bachtold, Imaging mechanical vibrations in suspended graphene sheets, Nano Letters, 8 (2008) 1399-1403.

[46] F. de Juan, A. Cortijo, M.A.H. Vozmediano, Charge inhomogeneities due to smooth ripples in graphene sheets, Physical Review B, 76 (2007) 165409.

[47] A. Fasolino, J.H. Los, M.I. Katsnelson, Intrinsic ripples in graphene, Nature Materials, 6 (2007) 858-861.

[48] F.d. Juan, A. Cortijo, M.A.H. Vozmediano, Charge inhomogeneities due to

smooth ripples in graphene sheets, Physical Review B, 76 (2007) 165409.

[49] F. Guinea, B. Horovitz, P. Le Doussal, Gauge field induced by ripples in graphene, Phys. Rev. B, 77 (2008) 205421.

[50] A.L.V. de Parga, F. Calleja, B. Borca, M.C.G. Passeggi, J.J. Hinarejos, F. Guinea, R. Miranda, Periodically rippled graphene: Growth and spatially resolved electronic structure, Phys. Rev. Lett., 100 (2008) 056807.

[51] A.L.V. de Parga, F. Calleja, B. Borca, C.G.P. M, Jr., J.J. Hinarejos, F. Guinea, R. Miranda, Periodically Rippled Graphene: Growth and Spatially Resolved Electronic structure, Phys. Rev. Lett., 100 (2008) 056807.

[52] W.Z. Bao, F. Miao, Z. Chen, H. Zhang, W.Y. Jang, C. Dames, C.N. Lau, Controlled ripple texturing of suspended graphene and ultrathin graphite membranes, Nat. Nanotechnol., 4 (2009) 562-566.

[53] C.-C. Chen, W. Bao, J. Theiss, C. Dames, C.N. Lau, S.B. Cronin, Raman Spectroscopy of Ripple Formation in Suspended Graphene, Nano Letters, 9 (2009) 4172-4176.

[54] A.K. Geim, P. Kim, Carbon wonderland, Scientific American, 298 (2008) 90-97.

[55] P. Blake, E.W. Hill, A.H.C. Neto, K.S. Novoselov, D. Jiang, R. Yang, T.J. Booth, A.K. Geim, Making graphene visible, Applied Physics Letters, 91 (2007).

[56] K.S. Novoselov, E. McCann, S.V. Morozov, V.I. Fal'ko, M.I. Katsnelson, U. Zeitler, D. Jiang, F. Schedin, A.K. Geim, Unconventional quantum Hall effect

and Berry's phase of 2 pi in bilayer graphene, Nat. Phys., 2 (2006) 177-180.

[57] S. Adam, E.H. Hwang, V.M. Galitski, S. Das Sarma, A self-consistent theory for graphene transport, Proceedings Of The National Academy Of Sciences Of The United States Of America, 104 (2007) 18392-18397.

[58] J.H. Chen, C. Jang, S. Adam, M.S. Fuhrer, E.D. Williams, M. Ishigami, Charged-impurity scattering in graphene, Nature Physics, 4 (2008) 377-381.

[59] J. Moser, A. Barreiro, A. Bachtold, Current-induced cleaning of graphene, Applied Physics Letters, 91 (2007) 163513.

[60] C.O. Girit, A. Zettl, Soldering to a single atomic layer, Applied Physics Letters, 91 (2007) 193512.

[61] N. Staley, H. Wang, C. Puls, J. Forster, T.N. Jackson, K. McCarthy, B. Clouser, Y. Liu, Lithography-free fabrication of graphene devices, Applied Physics Letters, 90 (2007) 143518.

[62] W.Z. Bao, G. Liu, Z. Zhao, H. Zhang, D. Yan, A. Deshpande, B. LeRoy, C.N. Lau, Lithography-free fabrication of high quality substrate-supported and freestanding graphene devices, Nano Res., 3 (2010) 98-102.

[63] M.M. Deshmukh, D.C. Ralph, M. Thomas, J. Silcox, Nanofabrication using a stencil mask, Applied Physics Letters, 75 (1999) 1631-1633.

[64] Y.X. Zhou, A.T. Johnson, Simple fabrication of molecular circuits by shadow mask evaporation, Nano Letters, 3 (2003) 1371-1374.

[65] M. Lishchynska, V. Bourenkov, M.A.F. van den Boogaart, L. Doeswijk, J.

Brugger, J.C. Greer, Predicting mask distortion, clogging and pattern transfer for stencil lithography, Microelectronic Engineering, 84 (2007) 42-53.

[66] S. Egger, A. Ilie, Y.T. Fu, J. Chongsathien, D.J. Kang, M.E. Welland, Dynamic shadow mask technique: A universal tool for nanoscience, Nano Letters, 5 (2005) 15-20.

[67] G. Liu, Electrical Transport in Carbon Nanotubes and Graphene, in, University of California, Riverside, 2010.

[68] F. Miao, Electronic Transport in Novel Nanoscale Systems: Graphene and Metal Oxide Switches, in, University of California, Riverside, 2009.

[69] K. Capelle, E.K.U. Gross, Relativistic framework for microscopic theories of superconductivity. I. The Dirac equation for superconductors, Physical Review B (Condensed Matter and Materials Physics), 59 (1999) 7140.

[70] B. Uchoa, A.H.C. Neto, Superconducting States of Pure and Doped Graphene, Phys. Rev. Lett., 98 (2007).

[71] J.C. Cuevas, A.L. Yeyati, Subharmonic gap structure in short ballistic graphene junctions, Physical Review B (Condensed Matter and Materials Physics), 74 (2006) 180501.

[72] J. Gonzalez, E. Perfetto, Cooper-pair propagation and superconducting correlations in graphene, Physical Review B, 76 (2007).

[73] C.W.J. Beenakker, Specular andreev Reflection in graphene, Phys. Rev. Lett., 97 (2006) 067007.

[74] M. Titov, A. Ossipov, C.W.J. Beenakker, Excitation gap of a graphene channel with superconducting boundaries, Phys. Rev. B, 75 (2007) 045417.

[75] K. Sengupta, R. Roy, M. Maiti, Spin Hall effect in triplet chiral superconductors and graphene, Physical Review B, 74 (2006).

[76] H.B. Heersche, P. Jarillo-Herrero, J.B. Oostinga, L.M.K. Vandersypen, A.F. Morpurgo, Bipolar supercurrent in graphene, Nature, 446 (2007) 56-59.

[77] X. Du, I. Skachko, E.Y. Andrei, Josephson current and multiple Andreev reflections in graphene SNS junctions, Physical Review B, 77 (2008) 184507.

[78] F. Miao, S. Wijeratne, Y. Zhang, U. Coskun, W. Bao, C.N. Lau, Phase Coherent Transport in Graphene Quantum Billiards, Science, 317 (2007) 1530-1533.

[79] A.F. Andreev, The Thermal Conductivity of the Intermediate State in Superconductors, Sov. Phys. JETP, 19 (1964) 1228.

[80] G.E. Blonder, M. Tinkham, T.M. Klapwijk, Transition from Metallic to Tunneling Regimes in Superconducting Micro-Constrictions - Excess Current, Charge Imbalance, and Super-Current Conversion, Physical Review B, 25 (1982) 4515-4532.

[81] C.W.J. Beenakker, Three "universa" mesoscopic Josephson Effects, in: H. Fukuyama, T. Ando (Eds.) Transport Phenomena in Mesoscopic Systems, Springer, Berlin, 1992.

[82] M. Titov, C.W.J. Beenakker, Josephson effect in ballistic graphene, Phys. Rev. B, 74 (2006) 041401.

[83] C.W.J. Beenakker, Colloquium: Andreev reflection and Klein tunneling in graphene, Rev. Mod. Phys., 80 (2008) 1337.

[84] M. Tinkham, Introduction to Superconductivity, Second Edition ed., McGraw-Hill Book Co., 1996.

[85] G. Liu, Y. Zhang, C.N. Lau, Gate tunable dissipation and superconductor-insulator transition in carbon nanotube Josephson Junctions, Phys. Rev. Lett., 102 (2009) 016803.

[86] R. Lutchyn, V. Galitski, G. Refael, S. DasSama, Dissipation-driven quantum phase transistion in superconductor-graphene systems, Physical Review Letters, 101 (2008) 106402.

[87] R.L. Willett, H.L. Stormer, D.C. Tsui, L.N. Pfeiffer, K.W. West, K.W. Baldwin, Termination of the series of fractional quantum hall states at small filling factors, Physical Review B, 38 (1988) 7881-7884.

[88] Y. Zhang, Z. Jiang, J.P. Small, M.S. Purewal, Y.W. Tan, M. Fazlollahi, J.D. Chudow, J.A. Jaszczak, H.L. Stormer, P. Kim, Landau-level splitting in graphene in high magnetic fields, Physical Review Letters, 96 (2006) 136806.

[89] D.A. Abanin, K.S. Novoselov, U. Zeitler, P.A. Lee, A.K. Geim, L.S. Levitov, Dissipative quantum Hall effect in graphene near the Dirac point, Phys. Rev. lett., 98 (2007) 1968006.

[90] Z. Jiang, Y. Zhang, H.L. Stormer, P. Kim, Quantum Hall states near the charge-neutral Dirac point in graphene, Phys Rev Lett, 99 (2007) 106802.

[91] Y. Zhao, P. Cadden-Zimansky, Z. Jiang, P. Kim, Symmetry Breaking in the Zero-Energy Landau Level in Bilayer Graphene, Phys. Rev. Lett., 104 (2010) 066801.

[92] B.E. Feldman, J. Martin, A. Yacoby, Broken-symmetry states and divergent resistance in suspended bilayer graphene, Nat. Phys., 5 (2009) 889-893.

[93] W.Z. Bao, Z. Zhao, H. Zhang, G. Liu, P. Kratz, L. Jing, J. Velasco, D. Smirnov, C.N. Lau, Magnetoconductance oscillations and evidence for fractional quantum Hall states in suspended bilayer and trilayer graphene, Phys. Rev. Lett., 105 (2010) 246601.

[94] X. Du, I. Skachko, F. Duerr, A. Luican, E.Y. Andrei, Fractional quantum Hall effect and insulating phase of Dirac electrons in graphene, Nature, 462 (2009) 192-195.

[95] K.I. Bolotin, F. Ghahari, M.D. Shulman, H.L. Stormer, P. Kim, Observation of the fractional quantum Hall effect in graphene, Nature, 462 (2009) 196-199.

[96] C.R. Dean, A.F. Young, P. Cadden-Zimansky, L. Wang, H. Ren, K. Watanabe, T. Taniguchi, P. Kim, J. Hone, K.L. Shepard, Multicomponent fractional quantum Hall effect in graphene, preprint, (2010) arXiv:1010.1179.

[97] D.A. Abanin, L.S. Levitov, Conformal invariance and shape-dependent conductance of graphene samples, Phys. Rev. B, 78 (2008) 035416.

[98] E. Prada, P. San-Jose, G. León, M.M. Fogler, F. Guinea, Singular elastic strains and magnetoconductance of suspended graphene, Phys. Rev. B, 81 (2010)

161402.

[99] V.M. Pereira, A.H. Castro Neto, All-graphene integrated circuits via strain engineering, Phys. Rev. Lett., 103 (2008) 046801.

[100] D.A. Abanin, I. Skachko, X. Du, E.Y. Andrei, L.S. Levitov, Fractional Quantum Hall Effect in Suspended Graphene: Transport Coefficients and Electron Interaction Strength, preprint, (2009) arXiv:0912.1134v0911.

[101] N. Shibata, K. Nomura, Fractional Quantum Hall Effects in Graphene and Its Bilayer, Journal of the Physical Society of Japan, 78 (2009) 104708.

[102] V.M. Apalkov, T. Chakraborty, Controllable Driven Phase Transitions in Fractional Quantum Hall States in Bilayer Graphene, Physical Review Letters, 105 (2010) 036801.

[103] T.C. Vadim Apalkov, Reentrant fractional quantum Hall states in bilayer graphene: Controllable, driven phase transitions, arXiv:1003.0378v1, (2010).

[104] V.C. Kyrylo Snizhko, Steven H. Simon, Importance of interband transitions for the fractional quantum Hall effect in bilayer graphene, arXiv:1112.1659v1, (2011).

[105] J.W. McClure, Diamagnetism of Graphite, Phys. Rev., 104 (1956) 666-671.

[106] E. McCann, V.I. Fal'ko, Landau-level degeneracy and quantum hall effect in a graphite bilayer, Phys. Rev. Lett., 96 (2006) 086805.

[107] M. Koshino, E. McCann, Gate-induced interlayer asymmetry in ABA-stacked trilayer graphene, Phys. Rev. B, 79 (2009) 125443.

[108] E. McCann, M. Koshino, Spin-orbit coupling and broken spin degeneracy in multilayer graphene, Phys. Rev. B, 81 (2010) 241409.

[109] B.I. Halperin, P.A. Lee, N. Read, THEORY OF THE HALF-FILLED LANDAU-LEVEL, Physical Review B, 47 (1993) 7312-7343.

[110] J.P. Eisenstein, G.S. Boebinger, L.N. Pfeiffer, K.W. West, S. He, NEW FRACTIONAL QUANTUM HALL STATE IN DOUBLE-LAYER 2-DIMENSIONAL ELECTRON-SYSTEMS, Physical Review Letters, 68 (1992) 1383-1386.

[111] M. Koshino, E. McCann, Trigonal warping and Berry's phase N pi in ABC-stacked multilayer graphene, Phys. Rev. B, 80 (2009) 165409.

[112] Y. Lemonik, I.L. Aleiner, C. Toke, V.I. Fal'ko, Spontaneous symmetry breaking and Lifshitz transition in bilayer graphene, Phys. Rev. B, 82 (2010) 201408.

[113] E. McCann, Asymmetry gap in the electronic band structure of bilayer graphene, Phys. Rev. B, 74 (2006) 161403.

[114] H.K. Min, B. Sahu, S.K. Banerjee, A.H. MacDonald, Ab initio theory of gate induced gaps in graphene bilayers, Phys. Rev. B, 75 (2007) 155115.

[115] R. Nandkishore, L. Levitov, Electron interactions in bilayer graphene: Marginal Fermi liquid and zero-bias anomaly, Physical Review B, 82 (2010).

[116] F. Zhang, J. Jung, G.A. Fiete, Q.A. Niu, A.H. MacDonald, Spontaneous quantum Hall states in chirally stacked few-layer graphene systems, Phys. Rev. Lett., 106 (2011) 156801.

[117] O. Vafek, K. Yang, Many-body instability of Coulomb interacting bilayer graphene: Renormalization group approach, Phys. Rev. B, 81 (2010) 041401.

[118] E.V. Castro, N.M.R. Peres, T. Stauber, N.A.P. Silva, Low-density ferromagnetism in biased bilayer graphene, Phys. Rev. Lett., 100 (2008) 186803.

[119] I. Martin, Y.M. Blanter, A.F. Morpurgo, Topological confinement in bilayer graphene, Phys. Rev. Lett., 100 (2008) 036804.

[120] R.T. Weitz, M.T. Allen, B.E. Feldman, J. Martin, A. Yacoby, Broken-symmetry states in doubly gated suspended bilayer graphene, Science, 330 (2010) 812-816.

[121] J. Martin, B.E. Feldman, R.T. Weitz, M.T. Allen, A. Yacoby, Local Compressibility Measurements of Correlated States in Suspended Bilayer Graphene, Phys. Rev. Lett., 105 (2010) 256806.

[122] F. Freitag, j. Trbovic, M. Weiss, C. Schonenberger, Spontaneously gapped ground state in suspended bilayer graphene, preprint, (2011) axXiv:1104.3816vs.

[123] J. Velasco, L. Jing, W. Bao, Y. Lee, P. Kratz, V. Aji, M. Bockrath, C.N. Lau, C. Varma, R. Stillwell, D. Smirnov, F. Zhang, J. Jung, A.H. MacDonald, Transport spectroscopy of symmetry-broken insulating states in bilayer graphene, preprint, (2011) arXiv:1103.6088.

[124] A.S. Mayorov, D.C. Elias, M. Mucha-Kruczynski, R.V. Gorbachev, T.

Tudorovskiy, A. Zhukov, S.V. Morozov, M.I. Katsnelson, V.I. Fal'ko, A.K. Geim, K.S. Novoselov, Interaction-driven spectrum reconstruction in bilayer graphene, Science, 333 (2011) 860.

[125] M. Koshino, T. Ando, Transport in bilayer graphene: Calculations within a self-consistent Born approximation, Phys. Rev. B, 73 (2006) 245403.

[126] J. Cserti, A. Palyi, C. Peterfalvi, Caustics due to a negative refractive index in circular graphene p-n junctions, Phys. Rev. Lett., 99 (2007) 246801.

[127] M. Trushin, J. Kailasvuori, J. Schliemann, A.H. MacDonald, Finite conductivity minimum in bilayer graphene without charge inhomogeneities, Phys. Rev. B, 82 (2010) 155308.

[128] Y.W. Tan, Y. Zhang, K. Bolotin, Y. Zhao, S. Adam, E.H. Hwang, S.D. Sarma, H.L. Stormer, P. Kim, Measurement of scattering rate and minimum conductivity in graphene, Phys. Rev. Lett., 99 (2007) 246803.

[129] K.I. Bolotin, K.J. Sikes, J. Hone, H.L. Stormer, P. Kim, Temperature-dependent transport in suspended graphene, Phys. Rev. Lett., 101 (2008) 096802.

[130] W.J. Zhu, V. Perebeinos, M. Freitag, P. Avouris, Carrier scattering, mobilities, and electrostatic potential in monolayer, bilayer, and trilayer graphene, Phys. Rev. B, 80 (2009).

[131] W. Bao, L. Jing, Y. Lee, J.V. Jr., P. Kratz, D. Tran, B. Standley, M. Aykol, S.B. Cronin, D. Smirnov, M. Koshino, E. McCann, M. Bockrath, C.N. Lau,

Stacking-Dependent Band Gap and Quantum Transport in Trilayer Graphene, Nat. Phys., (2011) to appear; preprint available at arxiv:1103.6088.

[132] H.K. Min, R. Bistritzer, J.J. Su, A.H. MacDonald, Room-temperature superfluidity in graphene bilayers, Phys. Rev. B, 78 (2008) 121401.

[133] F. Zhang, A.H. MacDonald, Distinguishing Spontaneous Quantum Hall States in Graphene Bilayers, preprint, (2011) arXiv:1107.4727v1101.

[134] Y.P. Liu, S. Goolaup, C. Murapaka, W.S. Lew, S.K. Wong, Effect of Magnetic Field on the Electronic Transport in Trilayer Graphene, ACS Nano, 4 (2010) 7087-7092.

[135] K.F. Mak, J. Shan, T.F. Heinz, Electronic structure of few-layer graphene: experimental demonstration of strong dependence on stacking sequence, Phys. Rev. Lett., 104 (2010) 176404.

[136] J.L. Manes, F. Guinea, M.A.H. Vozmediano, Existence and topological stability of Fermi points in multilayered graphene, Phys. Rev. B, 75 (2007) 155424.

[137] B. Partoens, F.M. Peeters, From graphene to graphite: Electronic structure around the K point, Phys. Rev. B, 74 (2006) 075404.

[138] S. Latil, L. Henrard, Charge carriers in few-layer graphene films, Phys. Rev. Lett., 97 (2006) 036803.

[139] M. Koshino, Interlayer screening effect in graphene multilayers with ABA and ABC stacking, Phys. Rev. B, 81 (2010) 125304.

[140] S. Das Sarma, S. Adam, E.H. Hwang, E. Rossi, Electronic transport in two dimensional graphene, Rev. Mod. Phys., (2010) to appear. arXiv:1003.4731v1002.

[141] C.H. Lui, Z. Li, Z. Chen, P.V. Klimov, L.E. Brus, T.F. Heinz, Imaging stacking order in few-layer graphene, Nano Lett., 11 (2011) 164-169.

[142] J. Martin, N. Akerman, G. Ulbricht, T. Lohmann, J.H. Smet, K.v. Klitzing, A. Yacoby, Observation of electron-hole puddles in graphene using a scanning single electron transistor, Nat. Phys., 4 (2008) 144-148.

[143] R. Nandkishore, L. Levitov, Flavor symmetry and competing orders in bilayer graphene, preprint, (2010) arXiv:1002.1966v1001.

[144] F. Zhang, H. Min, M. Polini, A.H. MacDonald, Spontaneous inversion symmetry breaking in graphene bilayers, Phys. Rev. B, 81 (2010) 041402 (R).

[145] X. Du, I. Skachko, A. Barker, E.Y. Andrei, Approaching ballistic transport in suspended graphene, Nature Nanotechnology, 3 (2008) 491-495.

[146] K.I. Bolotin, K.J. Sikes, J. Hone, H.L. Stormer, P. Kim, Temperature-dependent transport in suspended graphene, Physical Review Letters, 101 (2008) 096802.

[147] J.C. Meyer, A.K. Geim, M.I. Katsnelson, K.S. Novoselov, T.J. Booth, S. Roth, The Structure of Suspended Graphene Sheets, Nature, 446 (2007) 60-63.

[148] F. Guinea, B. Horovitz, P. Le Doussal, Gauge field induced by ripples in graphene, Physical Review B, 77 (2008) 205421.

[149] F. Guinea, M.I. Katsnelson, M.A.H. Vozmediano, Midgap states and charge inhomogeneities in corrugated graphene, Physical Review B, 77 (2008) 075422.

[150] A.L.V. de Parga, F. Calleja, B. Borca, M.C.G. Passeggi, J.J. Hinarejos, F. Guinea, R. Miranda, Periodically rippled graphene: Growth and spatially resolved electronic structure, Physical Review Letters, 100 (2008) 056807.

[151] E.-A. Kim, A.H. Castro Neto, Graphene as an Electronic Membrane, Europhysics Letters, 84 (2008) 57007.

[152] M.I. Katsnelson, A.K. Geim, Electron scattering on microscopic corrugations in graphene, Philosophical Transactions Of The Royal Society A-Mathematical Physical And Engineering Sciences, 366 (2008) 195-204.

[153] S.V. Morozov, K.S. Novoselov, M.I. Katsnelson, F. Schedin, D.C. Elias, J.A. Jaszczak, A.K. Geim, Giant intrinsic carrier mobilities in graphene and its bilayer, Physical Review Letters, 100 (2008) 016602.

[154] V.M. Pereira, A.H. Castro Neto, All-graphene integrated circuits via strain engineering, arXiv:0810.4539v1, (2008).

[155] D.C. Elias, R.R. Nair, T.M.G. Mohiuddin, S.V. Morozov, P. Blake, M.P. Halsall, A.C. Ferrari, D.W. Boukhvalov, M.I. Katsnelson, A.K. Geim, K.S. Novoselov, Control of graphene's properties by reversible hydrogenation arXiv:0810.4706v1, (2008).

[156] N. Mounet, N. Marzari, First-principles determination of the structural,

vibrational and thermodynamic properties of diamond, graphite, and derivatives, Physical Review B, 71 (2005) 205214.

[157] Y.K. Kwon, S. Berber, D. Tomanek, Thermal contraction of carbon fullerenes and nanotubes, Physical Review Letters, 92 (2004) 015901.

[158] P.K. Schelling, R. Keblinski, Thermal expansion of carbon structures, Physical Review B, 68 (2003) 035425.

[159] E. Cerda, L. Mahadevan, Geometry and physics of wrinkling, Physical Review Letters, 90 (2003) 074302.

[160] E.M. Lifshitz, L.D. Landau, Theory of Elasticity, 3rd ed., Butterworth-Heinemann.

[161] K.V. Zakharchenko, M.I. Katsnelson, A. Fasolino, Finite Temperature Lattice Properties of Graphene beyond the Quasiharmonic Approximation, Physical Review Letters, 102 (2009) 046808.

[162] F. Scarpa, S. Adhikari, A.S. Phani, Effective elastic mechanical properties of single layer graphene sheets, Nanotechnology, 20 (2009) 065709.

[163] Y.W. Wong, S. Pellegrino, Wrinkled membranes. Part II: analytical models. Journal of Mechanics of Materials and Structures, Journal of Mechanics of Materials and Structures, 1 (2006) 25-29.

[164] O.L. Blakslee, D.G. Proctor, E.J. Seldin, G.B. Spence, T. Weng, Elastic constants of compression-annealed pyrolytic graphite, Journal of Applied Physics, 41 (1970) 3373-3382.

[165] P. Peyla, Buckling of a compressed elastic membrane: a simple model, European Physical Journal B, 48 (2005) 379-383.

[166] M.E. Simon, C.M. Varma, Dynamics of Some Constrained Lattices, Phys. Rev. Lett., 86 (2001) 1781-1784.

[167] N. Abedpour, M. Neek-Amal, R. Asgari, F. Shahbazi, N. Nafari, M.R.R. Tabar, Roughness of undoped graphene and its short-range induced gauge field, Physical Review B, 76 (2007) 195407.

[168] R.C. Thompson-Flagg, M.J.B. Moura, M. Marder, Rippling of graphene, Europhysics Letters, 85 (2009) 46002.

[169] D.C. Elias, R.R. Nair, T.M.G. Mohiuddin, S.V. Morozov, P. Blake, M.P. Halsall, A.C. Ferrari, D.W. Boukhvalov, M.I. Katsnelson, A.K. Geim, K.S. Novoselov, Control of graphene's properties by reversible hydrogenation Science, 323 (2009) 610-613.

[170] N. Bowden, S. Brittain, A. Evans, J.W. Hutchinson, G.M. Whitesides, Spontaneous formation of ordered structures in thin films of metals supported on an elastomeric polymer, Nature, 393 (1998) 146-149.

[171] A. Isacsson, L.M. Jonsson, J.M. Kinaret, M. Jonson, Electronic superlattices in corrugated graphene, Physical Review B, 77 (2008) 035423.

[172] C.H. Park, Y.W. Son, L. Yang, M.L. Cohen, S.G. Louie, Electron beam supercollimation in graphene superlattices, Nano Letters, 8 (2008) 2920-2924.

[173] L.B. Freund, S. Suresh, Thin Film Materials, Cambridge University Press,

2003.

[174] S. Ghosh, W.Z. Bao, D.L. Nika, S. Subrina, E.P. Pokatilov, C.N. Lau, A.A. Balandin, Dimensional crossover of thermal transport in few-layer graphene, Nat. Mater., 9 (2010) 555-558.

[175] M.M. Fogler, F. Guinea, M.I. Katsnelson, Pseudomagnetic Fields and Ballistic Transport in a Suspended Graphene Sheet, Phys. Rev. Lett., 101 (2008) 226804.